Inverse opal hydrogel scaffolds as lymphoid microenvironments for the study of immune cell migration and immunotherapy

by

Agnieszka Stachowiak

S.B. in Chemical Engineering
Massachusetts Institute of Technology, 2001

SUBMITTED TO THE DEPARTMENT OF MATERIALS SCIENCE AND ENGINEERING IN PARTIAL FULFILLMENT OF THE REQUIREMENTS FOR THE DEGREE OF

DOCTOR OF PHILOSOPHY IN MATERIALS SCIENCE AND ENGINEERING
AT THE
MASSACHUSETTS INSTITUTE OF TECHNOLOGY

JUNE 2007

Signature of Author: _____

Department of Materials Science and Engineering
May 17, 2007

Certified by: _____

Darrell J. Irvine
Eugene Bell Associate Professor of Tissue Engineering
Thesis Advisor

Accepted by: _____

Samuel M. Allen
POSCO Professor of Physical Metallurgy
Chair, Departmental Committee on Graduate Students

Inverse opal hydrogel scaffolds as lymphoid microenvironments for the study of immune cell migration and immunotherapy

by

Agnieszka Stachowiak

Submitted to the Department of Materials Science and Engineering on May 17, 2007 in Partial Fulfillment of the Requirements for the degree of Doctor of Philosophy in Materials Science and Engineering

ABSTRACT

Immunotherapies harness the inherent potential of the body to destroy foreign or infected cells, by stimulating new or enhancing existing immune responses. One way to boost insufficient native immunity might be to engineer lymphoid tissue at disease sites (e.g., tumors). Such neotissues could be formed by attracting or transferring immune cells into a defined microenvironment supportive of their activation. In addition to having therapeutic potential, such artificial lymphoid scaffolds could be used as *in vitro* models to investigate how immune cells respond to changing properties of their environment (e.g., architecture or biochemistry). We developed and tested macroporous poly(ethylene glycol) (PEG) hydrogel scaffolds as a platform for lymphoid tissue models and immunotherapy. By applying the method of colloidal crystal templating to materials and length scales appropriate for soft tissues, PEG hydrogels with arrays of ordered, interconnected pores were prepared. These combined the attractive properties of hydrogels, including biochemical versatility and tissue-mimetic mechanical properties, with the benefits of a macroporous structure, including improved nutrient transport and a defined space for cell interactions. Moreover, the ordered pore arrangement provided high interconnectivity at unprecedented (low) porosities. We primarily tested the migratory responses of T cells to these novel hydrogel scaffolds, due to the importance of rapid T cell motility in promoting efficient immune responses. Varying the choice of adhesion ligand coating the scaffolds prompted significant T cell trafficking only for the case of intercellular-adhesion-molecule I (ICAM-1), and ultimately, a composite scaffold structure was required to attain *in vivo*-like cell migration. In this modified structure, the porous PEG hydrogel provided mechanical stability and the ability to deliver proteins of interest, while an infused collagen matrix supported intra-scaffold migration of loaded T cells and dendritic cells. We tested the effect of scaffold architecture in the composites, and found that increasing the PEG pore size enhanced T cell motility. We also demonstrated the delivery of the chemokine CCL21 – a cytokine likely to be useful for immunotherapy – to cells within composite scaffolds. This hybrid scaffold approach combines the strengths of the synthetic and biopolymer hydrogels used in a complementary fashion, and may be generally useful for tissue engineering.

Thesis Supervisor: Darrell J. Irvine

Biographical Note

Publications

Stachowiak, A.N. and Irvine, D.J. Inverse opal hydrogel-collagen composite scaffolds as a supportive microenvironment for immune cell migration, submitted.

Stachowiak, A.N., Wang, Y., Huang, Y., and Irvine, D.J. Homeostatic lymphoid chemokines synergize with adhesion ligands to trigger T and B lymphocyte chemokinesis, *J Immunol, 177:2340-2348* (2006)

Stachowiak, A.N., Bershteyn, A., Tzatzalos, E., and Irvine, D.J. Bioactive hydrogels with an ordered cellular structure combine interconnected macroporosity and robust mechanical properties, *Adv Mat, 17:399-403* (2005)

Irvine, D.J., Stachowiak, A.N., and Jain, S. Engineering materials for control of immune functions, *Mat. Sci. Forum*, 426-432, 3213-3218 (2003)

Conference Presentations

Oct. 2006 – Biomedical Enginering Society – Dynamic interactions of immune cells in porous hydrogel scaffolds for lymph node tissue engineering (talk)

May 2006 – American Association of Immunologists – Homeostatic lymphoid chemokines synergize with adhesion ligands to trigger lymphocyte chemokinesis (talk and poster)

Mar. 2005 – Keystone Symposium – Lymphocyte migration in a 3D *in vitro* model of the lymph node T zone (poster)

Dec. 2004 – Materials Research Society – Natural and artificial bioactive hydrogels with interconnected macroporosity and robust mechanical properties (poster)

Apr. 2004 – Experimental Biology – Toward an *in vitro* model of the lymph node T zone (poster)

May 2003- Society for Biomaterials – Towards and artificial lymph node: imaging lymphocyte interactions on polymeric scaffolds (talk)

Dec. 2003 – Materials Research Society – Lymphoid scaffolds prepared by colloidal crystal templating (talk)

Acknowledgements

First and foremost I would like to thank my advisor Darrell Irvine. Darrell's boundless optimism and insight have been an excellent match for my own skepticism and quick criticism. Nothing revitalized my enthusiasm for my project at tough times quite like our brainstorming sessions. I am grateful to have worked with Darrell not only as a scientist but as an educator, and I have fond memories of my time as a teaching assistant for his thermodynamics course.

I would also like to thank my fellow students – particularly my brilliant first colleagues, Junsang Doh and Siddhartha Jain, for their insight and camaraderie during the formative years of our lab's existence. Yana Wang, Yuki Hori, Ashley Salomon and Yen-Chen Huang each participated in useful experiments and discussions related to scaffold systems and chemokines. Maria Foley brought useful real-world experience to the lab from her days in the biotechnology industry, as well as a much welcomed impetus to organize our quickly-growing lab. I have learned from and enjoyed working with Heejae Kim, Yuhua Hu, Bonnie Huang, Brandon Kwong, Vinay Mahajan, and Andrew Miller. My summer UROP student Elina Tzatzalos worked closely and diligently with me during the first period of concerted work on my project. Anna Bershteyn provided invaluable creativity and contributed directly to the optimization of the colloidal crystal templating process as my UROP student, and more recently has been a pleasure to work with as a graduate colleague.

There are a number of people I would like to thank for technical assistance over the years. I especially want to thank Glenn Paradis at the MIT Flow Cytometry facility and Don Galler of the Gibson Scanning Electron Microscope facility for their excellent and friendly instruction. I appreciate the early training in confocal microscopy that I received from Nicki Watson at the Keck Imaging Facility. Brendan Harley was generous with his time and resources in teaching me mechanical properties assays and discussing biopolymer cross-linking methods. Peter Morley and others at the MIT Machine Shop were helpful and solid craftsmen. Dr. Richard Colvin shared his expertise regarding chemotaxis assays. Sheree Beane was a wonderful addition to our lab in the past few years, and made all our lives easier in her role as lab manager.

Apart from my advisor, several faculty members have enriched my graduate experience. Professor Nir Hacohen was patient and helpful in discussing several biological areas of relevance to my project, including trends in cancer therapies. Professor Lorna Gibson's discussion of her work in cellular solids provided a useful framework for my first peer-reviewed publication. Professor Peter So gave expert advice on imaging technologies. Professor Anne Mayes prompted me to carefully consider the scope of my work at an important juncture in the life of this project. The lecturers in my graduate courses were almost uniformly excellent, and I appreciate their contribution to my intellectual development as well.

My family, friends, and partners over the past six years have played an important role in providing balance and support in a hectic life. I am grateful to the MIT Chamber Music Society and all the musicians I played with for the beautiful respite from everyday stresses that we created. Housemates and other friends have been a joy to live and spend time with. My mother, father, and brother have been an inspiration and encouragement to me – the dedication and expansive approach to education in my upbringing has greatly influenced who I am today. Finally, my dearest Wally has shared the best and worst of the past three years with me, and I look forward to many more years of laughter, growing up and out together, and tortles.

This work was funded by an National Defense Science and Engineering fellowship, the Whitaker Foundation (RG-02-0837) and DARPA (award W81XWH-04-C-0139).

TABLE OF CONTENTS

1 Background and Significance

The present work is motivated both by fundamental cell biology questions and by therapeutic applications in the field of immunology. These motivating problems may be addressed by *in vitro* lymphoid tissue models and by *in vivo* therapeutic tissue engineering, respectively. For this work, we developed a novel macroporous polymer scaffold, modified it with adhesion and signaling proteins, and studied the *in vitro* behavior of immune cells within the resulting construct. We were particularly concerned with creating a lymphoid microenvironment supportive of T cell migration, due to the importance of rapid T cell motility in promoting efficient immune responses. This chapter will introduce key facets of the immune response, followed by a discussion of prior relevant work in immunotherapy and tissue engineering. Finally, our specific objectives and contribution to the field will be outlined.

1.1 Cells and signals in the immune response

1.1.1 Organization of lymph node microenvironment

The primary function of lymph nodes is to provide a supportive environment in which adaptive immune responses to pathogens (bacteria, viruses, etc.) are initiated, and to this effect lymph nodes are present at regular intervals throughout the human body (1). Each lymph node is a complex organ with several distinctive features, including a compartmentalized structure. T and B lymphocytes – white blood cells that play a key role in the immune response – are segregated into distinct zones: B cells are primarily present in follicles that have relatively little extracellular matrix (ECM), while T cells typically reside in the lymph node paracortex or T zone, a cell-rich area with a loosely woven but substantial ECM (see Figure 1-1). Other secondary lymphoid organs (such as the spleen) have similar structures and purpose, while primary lymphoid organs are where immune cells develop.

The T zone extracellular matrix is known as the reticular network, due to its distinctive microfibrous structure. Thick collagen fibers (0.5-5 μm in diameter) lie ~5-35 μm apart in all directions, creating pores in which lymphocytes are packed to high density (2-4). The collagen-core fibers are covered by a basement membrane-like layer including fibronectin, laminins, and perlecan (5), and are largely ensheathed by a layer of fibroblastic reticular cells (FRCs) – a stromal component of secondary lymphoid organs – and by dendritic cells (3, 6, 7). We became interested in mimicking this architecture and biochemical composition in synthetic scaffolds, as described more completely in sections 1.2-1.4. Within the T zone, T cells may become activated upon encountering their cognate antigen presented by a dendritic cell; this process is described in the following section.

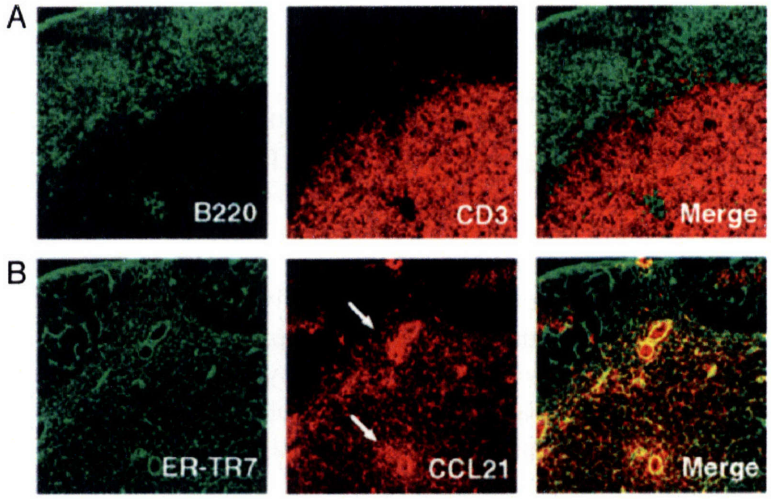

Figure 1-1 **Lymph node architecture and cellular composition.** Immunostaining of lymph node sections was performed by Katakai et al. (3). (A) T cells expressing CD3 (shown in red) and B cells expressing B220 (shown in green) segregate to distinct areas of the lymph node. (B) ER-TR7 antigen (expressed and secreted by lymphoid fibroblasts) forms a denser network in the T cell-rich paracortex than in the B cell-rich follicles. The chemokine CCL21 (to be discussed in section 1.1.3) is present in the T cell areas almost exclusively.

1.1.2 T cell priming and migration in secondary lymphoid organs

The immune system is composed of innate and adaptive components, both of which act to eliminate foreign pathogens. Innate immunity is a fast response of limited specificity, while adaptive immunity is slower but highly specific, and has the additional characteristic of memory. In a typical adaptive immune response, dendritic cells (DCs) ingest or otherwise acquire pathogenic elements in the peripheral tissues of the body, and then undergo a maturation process while they travel to the secondary lymphoid organs (such as spleen, lymph nodes, and Peyer's patches). There they display pathogen-derived antigens at their surfaces for inspection by T lymphocytes and other cells (see Figure 1-2). Each T cell has receptors specific for a single antigenic epitope, receptors whose population diversity is kept high by somatic recombination of multiple germ-line elements during cell development (1, 8). Because of this random generation and great diversity, few (typically on the order of 1 in 10^5 (9, 10) or fewer) T cells have receptors cognate to any given antigen, and these cells must rapidly find a DC presenting said antigen in order to initiate a primary immune response in a timely and effective manner. Naïve T cells – cells that have not previously encountered antigen – constitutively circulate between the blood and lymph nodes in turn, entering the lymphoid tissue via high endothelial venules (HEV) (11). If they are not stimulated, most naïve T cells will eventually die, because they compete for a limited pool of survival-maintaining cytokines (1, 12). DCs are the only antigen-presenting cells capable of activating naïve T cells, due perhaps to such factors as their very high level of co-stimulatory molecules (13).

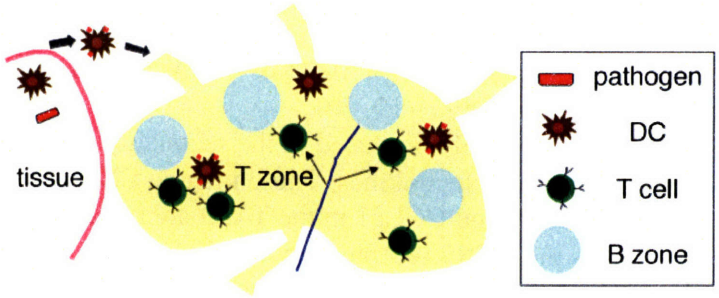

Figure 1-2 **Schematic of events in the primary immune response.** Dendritic cells encounter pathogens in peripheral tissues such as skin, ingest and break them up into small surface-presented antigens, and then travel to the lymph nodes. Naïve T cells emerge from venules (blue line) into the T zone of the lymph node, where they encounter DCs that may activate them.

Upon activation by antigen-bearing DCs, many naïve T cells become effector cells, i.e., cells that effect the elimination of the invading pathogen. $CD8^+$ cytolitic/cytotoxic T cells do this by lysing pathogen-infected cells (14). $CD4^+$ helper T cells perform helper (stimulation) functions for cells such as antibody-secreting B cells and $CD8^+$ T cells, by secreting cytokines as well by direct cell-cell contact (15). Eventually the effector cells die, but a small fraction of activated naïve cells also become long-lived memory cells. Immune responses to previously encountered pathogens are more rapid and more effective, due to the continued presence of these memory cells (16). In our work, we focused on studying naïve as well as activated $CD4^+$ T cells, due to their central role in interacting with multiple immune cell types.

In the past few years, imaging of lymph nodes in live anesthetized mice (intravital microscopy) has given a new window into the behavior of immune cells during both resting and immune-activated conditions. Both $CD4^+$ and $CD8^+$ T cells rapidly migrate throughout the lymph nodes at ~ 10 μm/min on average, and contact DCs for ~ 3 min. per encounter in the absence of antigenic stimulation (10, 17). DCs themselves move at only 2-3 μm/min on average and are largely present as a stationary network, though their extensive dendrites increase their effective cell size (6, 17). Together, these factors mean that each DC can encounter 500-5000 naïve T cells per hour (10, 17).

The above studies have shown that T cell migration specifically is one key element in the success of primary immune responses. Several aspects of the lymph node microenvironment, including architecture (see section 1.1.1), cellular organization, and soluble signaling molecules (see section 1.1.3), are also likely to promote efficient and effective immune responses, some of them via influencing cell migration. We were thus interested in recreating some of these important factors in an artificial lymphoid microenvironment, and measuring the resulting T cell migration responses. Variation of environmental parameters coupled with migration assessments served both as a study of how microenvironmental cues influence T cell migration, and helped to determine the utility of a given synthetic scaffold for immune-based therapies.

1.1.3 Role of chemokines in lymphoid organ development and function

Cytokines are soluble (or surface-presented) polypeptides involved in cell communication: one cell type secretes (or presents) a cytokine in order to influence the behavior of target cells (of the same or another lineage) that express a receptor for that cytokine. Binding of a cytokine ligand to

its target receptor may result in cell proliferation, differentiation, or act as a survival cue, to give a few common functions of cytokines (18). Cytokines are particularly abundant in the lymphoid system – there exists a large sub-class called interleukins – and chemokines are an important class of cytokines that affect cell migration (19, 20).

Several chemokines are constitutively produced in the secondary lymphoid organs, and are thus known as homeostatic lymphoid chemokines. These include CXCL13 in the B cell areas of lymph nodes, and CXCL12, CCL19 and CCL21 in the T cell areas (see Figure 1-3). T cells (and to some extent B cells) express the CCR7 receptor, which binds both CCL19 and CCL21, while only B cells express the CXCL13-binding receptor CXCR5. CCL21 and CCL19 are strong inducers of T cell chemotaxis, that is, T cells will follow a gradient of increasing chemokine concentration (21), and CXCL13 has similar effects on B cells (22). Upon activation, B cells upregulate CCR7 and subsequently travel to the border between the T cell and B cell zones in the lymph node to receive T cell help (23). Similarly, DCs that have been stimulated to mature (e.g., by an encounter with pathogen) upregulate CCR7 and become responsive to CCL19/21. This causes the DCs to travel from peripheral tissues to lymph nodes where they can activate T cells.

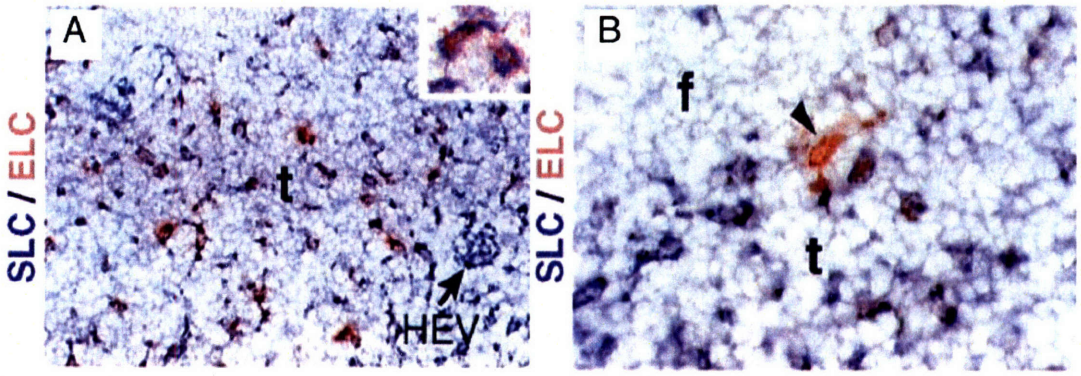

Figure 1-3 **Homeostatic chemokine expression in lymph nodes.** Luther et al. performed *in situ* hybridization experiments on lymph node sections to test for localization of different chemokines (24). (A) The T cell zone – marked 't' – includes many cells staining for CCL21 (also called SLC) and/or CCL19 (ELC). (B) In the B cell-rich follicles – marked 'f' – there is little to no staining for CCL21 and CCL19.

These three chemokines – CCL21, CCL19, and CXCL13 – thus appear to be involved in homing of lymphocytes and dendritic cells to their respective compartments in the lymphoid organs, and this is true under not only activated but also under homeostatic and developmental conditions (23, 25). The latter is evidenced by studies with knockout mice lacking the genes for CCR7, CCL19, or CCL21: such mice have disrupted lymphoid architecture and cellular composition (24, 26). Murine CXCR5 and CXCL13 knockouts have more severe defects, including the lack of some types of lymph nodes (27).

In addition to their role in cell homing in the adult, lymphoid chemokines also play a role in lymphoid organogenesis, downstream of lymphotoxin (LT). Mice lacking the genes for the LTα or LTβ chains, or the LTβ receptor, develop few or even none of their secondary lymphoid organs (28-31), which may be compared to the less severe effects of T zone chemokine deletion. In the developing Peyer's patches (lymphoid tissue nodules that line the small intestine),

interactions between LT-β receptors on stromal cells and LT-presenting 'inducer' cells cause the secretion of chemokines such as CCL21 by stromal cells, which in turn influences lymphocyte development (32); similar processes are believed to occur in lymph nodes (33). Transgenic expression of members of both the lymphotoxin and lymphoid chemokine families has been attempted in several cell types, and causes varying degrees of neotissue development (34-36). For example, induced expression of CCL21 in pancreatic islet cells is enough to stimulate formation of 'tertiary' lymphoid tissues with organized cell compartments in the pancreas within six weeks after birth (36-38).

Although cytokines and cells involved in homing and development have been relatively well-defined, much less is known about what signals affect homeostatic migration of cells, particularly naïve T lymphocytes, once they reach the lymph nodes during normal circulation (39). An *in vitro* model of lymphoid tissue could be used to test the effect of different soluble factors in a 3D tissue-like environment, in which the type and concentration of chemokine may be defined and varied at will, as can physical factors such as cell density and pore size.

While an *in vitro* model of lymph nodes could be used to dissect microenvironmental cues governing lymph node function, it might also be useful as an *in vivo* platform for immunotherapy, particularly in concert with soluble signals such as chemokines. Chemokines have at least two qualities – promotion of lymphoid cell chemoattraction and of lymphoid neotissue development – which may be useful in immunotherapies, as described below.

1.2 New strategies in cancer immunotherapies

Understanding and manipulating the immune response to tumors could assist in development of new cancer therapies. Many tumors display weakly immunogenic antigens that stimulate an incomplete adaptive immune response, causing an influx of tumor-infiltrating lymphocytes (TILs). The presence of TILs correlates with increased survival in many cancers, including ovarian (40), as well as breast, bladder, and prostate (41). In the second most lethal cancer – colorectal (42) – the number (and type) of invading immune cells has been shown to correlate positively with duration of patient survival, and to predict survival better than the current histopathological standard (43). Thus, the adaptive immune response to transformed cells does appear to have some ability to eradicate tumors.

However, cancers also can employ a variety of strategies that cause immune suppression or immune ignorance. These methods include recruitment of immunosuppressive T regulatory cells, tumor secretion of immunosuppressive factors such as TGFβ, tumor cell downregulation of 'recognizable' elements such as MHC, and the tumor stroma as a physical barrier (44). To take a specific instance, tumor cells can modulate the surrounding cytokine environment to halt the maturation of antigen-presenting cells such as DCs, which upon encountering T cells will then render them tolerant to tumor antigens rather than active against them (45). Somewhat paradoxically, several aspects of the innate immune response can worsen cancer (46): chronic inflammation due to innate immune cell infiltrates and inflammatory cytokines can promote immunosuppression, and cancer can both cause and be exacerbated by such persistant inflammation (47). Combating or evading immunosuppression while boosting the specific, adaptive immune response against tumor antigens is thus a desired goal in immunotherapy (44, 48).

One method of enhancing immune function may be to stimulate the *de novo* formation of organized lymphoid tissue, since the architecture and cell compartmentalization in secondary lymphoid organs is believed to make immune responses highly efficient (2, 3, 49). As described in section 1.1.3, a number of cytokines play a role in progressive stages of immune organogenesis or neogenesis, including those in the lymphotoxin and chemokine families. Although lymphoid neogenesis in previously healthy adults is associated with certain pathologies, particularly of the autoimmune and chronic inflammation variety (50, 51), studies of cytokine targeting or cell transfection in tumors have indicated a therapeutic role for the formation of lymphoid-like tissue proximate to a cancerous mass.

In one study, targeting of LTα to murine pulmonary and subcutaneous tumors effectively eliminated them, and resulted in large T cell and other immune cell infiltrates at the tumor site (52). Alternatively, tumor cells can themselves be harnessed to create a lymphoid-like environment by genetic modification. For example, tumor stromal cells that were transfected with LIGHT (homologous to Lymphotoxins, exhibits Inducible expression, and competes with HSV Glycoprotein D for HVEM, a receptor expressed by T lymphocytes), a cytokine ligand for LTβ receptor, stimulated invading stromal cells to express CCL21 as well as lymphoid tissue-associated adhesion molecules, resulting in T cell infiltrates that fought the tumor (53). Finally, chemokines themselves have been directly injected at tumor sites. CCL21 injection in a lung mouse model caused notable tumor regression/eradication, an increase in immune cell infiltrates in the tumor, and a decrease in immunosuppressive cytokines typically associated with tumors (54). CCL21 transfection of tumor cells has also been attempted, and the authors showed that in that case one operating anti-tumor mechanism was inhibition of angiogenesis (55).

We believe that CCL21 in particular may be an ideal candidate for immunotherapy, for the above-mentioned reasons – ability to combat immunosuppression, angiostatic activity in mice – as well as others. This chemokine attracts both naïve T cells and mature dendritic cells (DCs), and causes a greater ratio of naïve:memory T cells than does LTα when ectopically expressed in pancreas (35, 36). This is beneficial because only naïve cells can respond to a new antigen, while the attracted memory cells may have already been primed against an irrelevant (i.e., not a tumor) antigen. CCL21 also attracts $CD4^+$ and $CD8^+$ cells nearly equally (21, 56), which is desirable since $CD8^+$ cells need helper functions provided by $CD4^+$ T cells for the strongest response possible (57).

Due to the short half-life of injected proteins such as CCL21 *in vivo*, they have to be injected frequently (e.g., every other day) to have a lasting effect. This is both expensive and undesirable for patient compliance. Further, systemic injections of cytokines may cause unintended side effects, while frequent injection directly at a tumor site can only be performed in cases where the tumor is near enough to the skin surface. Injection at deeper tumor sites (e.g., during resection) can realistically only be performed rarely, due to the invasiveness of the procedure. As an alternative, delivery to a tumor site of cells that transgenically express a needed protein would seem to alleviate some of these problems, by providing an inexhaustible supply of chemokine. However, this strategy comes with all the risks of gene therapy (such as stimulating new tumors to form) (58), as well as the labor and expense of creating a transfected cell line.

Due to the drawbacks and complications described above, we became interested in the development of strategies to synthetically induce the *de novo* formation of tertiary lymphoid tissue at ectopic sites via implantable scaffolds that release chemokine in a controlled fashion (see Figure 1-4). These could be used both as a potential therapeutic strategy for the treatment of solid tumors, and as a tool to understand cues controlling ectopic lymphoid tissue formation or

other basic questions in immune biology. Such a strategy has certain advantages, in that a scaffold could simultaneously provide release of biological factors (such as CCL21) and provide a defined space and suitable architecture for cell interactions, which may be more effective than merely injecting both cells and soluble factors. This approach could be combined with adoptive transfer therapies by pre-loading the scaffold with tumor-specific cells expanded *ex vivo*, or be used simply to attract cells already within the body. One disadvantage of this system, however, is that the chemokine may still be cleared too rapidly, as there is a limit to how much can be loaded on the scaffold surfaces. Further, the invasiveness of the implantation procedure would limit it to cases where operation at the tumor site is already required. Nevertheless, lymphoid scaffolds may be useful in precisely such cases. In the following section, we describe our selection/design rationale for producing lymphoid scaffolds.

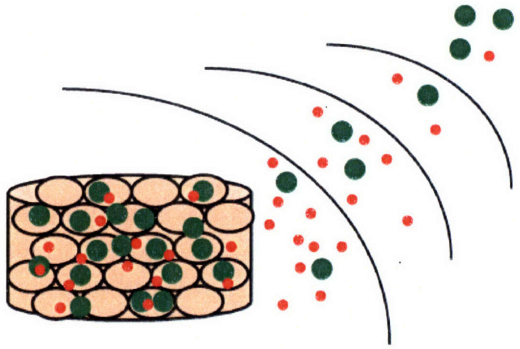

Figure 1-4 **Schematic of immunotherapy approach.** A porous scaffold (beige, with pores outlined in black) that releases CCL21 (small red circles) could be implanted at a tumor site, forming a chemokine gradient that attracts T cells and dendritic cells (large green circles). For simplicity, the radially symmetric gradient is shown at only one side of the scaffold.

1.3 Materials selection for tissue engineering and tissue models

1.3.1 General considerations for biomaterials

The use of natural and artificial materials in biology and medicine has a long-standing history. The three major classes of materials – polymers, ceramics, and metals – have all been used successfully as biomaterials, and materials selection depends on the exact purpose at hand (59). In the quintessential tissue engineering paradigm, a scaffold, usually porous, is loaded with cells and/or soluble factors, implanted at a wound or disease site, and slowly degrades as it is replaced with new cells and tissue (60-63). Hard tissues such as bone require scaffolds with mechanical properties typical of metals and ceramics (and some hard polymers), while soft tissues such as skin or cartilage may be more suitably replaced or guided by polymeric scaffolds.

In additional to mechanical properties, the exact chemical and especially biochemical properties that are desired for a scaffold vary from application to application. One often wants to support the viability and activity of one cell type – using appropriate adhesion ligands, soluble growth factors, etc. – while excluding bacteria, the formation of blood clots that are dangerous to the patient, and toxic and immunogenic elements. Collectively, the interaction of a material with the body without causing harm is known as biocompatibility, while selective targeting of cells and promotion of behaviors such as differentiation or adhesion is known as bioactivity.

1.3.2 Polymeric hydrogels for tissue engineering

Both mechanical and chemical properties are readily altered in many polymer systems, by the introduction of cross-linking reagents (or mechanically strong co-polymers) and labile moieties, respectively. Polymeric hydrogels, which swell in water but remain insoluble, are particularly attractive for tissue engineering: their high water content facilitates diffusion of aqueous nutrients and oxygen throughout these structures, and mimics the permeability and mechanical properties of natural soft tissues (64, 65). Hydrogels are typically formed under mild conditions that do not require the use of organic solvents, meaning that there is no danger of residual toxins from solvent sources causing damage to cells later. Both synthetic and natural hydrogels often form quickly from liquids at room or physiological temperatures. For some applications, hydrogels are favored for their ability to be mixed directly with cells and injected into arbitrarily shaped wounds for *in situ* gelation (66-68).

Natural gel biopolymers used as biomaterials include alginate (an ion-complexed polysacharride), other polysacharrides such as chitosan and hyaluronic acid, the peptide fibrin that is involved in blood clotting, and the ECM gels collagen and gelatin (denatured collagen). Each of these materials has certain advantages: the mechanical strength, gelation time, and degradability of alginate can all be regulated by mixing of multiple alginate elements (69), fibrin can be extracted from autologous sources (i.e., human serum) (65), and gelatin can be treated to expose positive or negative surface charges for attachment of negatively or positively charged proteins, respectively (70). However, most natural biopolymers suffer from poor mechanical strength, possible immunogenicity due to derivation from xenologous sources, and a high degree of variation between lots and even within a single gel (65). This variation makes the ultimate behavior – such as degradation rate – difficult to predict (71).

Synthetic hydrogels have the advantage of both reproducibility and tuneability. Many such hydrogels are made by photopolymerization chemistry, which offers the additional advantages of spatial and temporal control of gelation, high conversion rates, and energy efficient production (72). The main drawback of synthetics is that the biocompatibility of these materials and their degradation products may be difficult to predict and must be carefully tested. The most common photopolymerizable polymers studied for use in tissue engineering applications so far have been poly(vinyl alcohol), poly(2-hydroxyethyl methacrylate), and poly(ethylene glycol), known as PVA, poly(HEMA), and PEG, respectively (72-74).

PEG is a commonly used biomaterial, and has proven its biocompatability in some applications well enough to meet FDA approval standards (65). One reason it is so attractive is that PEG in a broad range of molecular weights and architectures exhibits a natural resistance to protein adsorption and cell adhesion, likely due to steric interactions and its many non-covalent (e.g., hydrogen) bonds with water (75). Otherwise inert PEG can be made bioactive by chemical modification and conjugation of proteins or protein analogues. Dr. Jeffrey Hubbell's lab pioneered the introduction of bioactivity into PEG gels made by radical chain polymerization of PEG diacrylates. The bioactivity is introduced by co-polymerizing adhesive or enzyme-sensitive peptides on PEG-monoacrylate (PEGA) tethers or as PEGA-peptide-PEGA blocks (76). The introduction of specific bioactivity is desirable for targeting certain cell types. For example, the PEG-tethered peptide RGD has been used to promote spreading and organization of osteoblasts (67), and even to stimulate vascularization and connective tissue formation *in vivo* (77), while PEG gels presenting the peptide VAPG are selective for smooth muscle cells while preventing fibroblast and endothelial cell adhesion (78).

For these reasons, we focused on cross-linked PEG hydrogels in our studies. We initially studied cell responses to peptide-modified gels similar to those described above, and later developed a method for attaching whole adhesion proteins to PEG. In this method (further explained in Ch. 4), biotinylated proteins were attached to biotin-containing scaffolds by using streptavidin as a bridging molecule.

1.3.3 Fabrication strategies for porous scaffolds

Porosity at various length scales has been introduced in natural as well as artificial polymers, in both hydrophilic hydrogels and more hydrophobic polymers. Pores are used to enhance diffusion of nutrients, gases, and other biologically relevant compounds, as well as to allow cell loading or ingrowth within a structure. Interconnectivity between pores is key for taking full advantage of increased diffusion and space for cell development and interactions.

The polyesters poly(lactic acid) and poly(glycolic) acid, PLA and PGA, are perhaps the most ubiquitous biomaterials used clinically to date (59). These hydrophobic polymers are typically obtained in powdered form, dissolved in organic solvents, and made porous by methods such as salt leaching, phase separation, gas foaming, and solid freeform fabrication. Co-polymers of PLA and PGA are readily degradable on different time scales (based on the PLA:PGA ratio) with metabolizable acidic byproducts. However, these polymers have the disadvantage of lacking readily modifiable groups for attaching biological moieties.

For a soft tissue application, hydrogels are more suitable and attractive than PLA-co-PGA, for the reasons described in the previous section. However, since much of the work on pore formation has been done with hydrophobic polymers, pore-forming methods will first be discussed in this context. Solid freeform fabrication was originally designed with such polymers in mind. In a typical process, arbitrary 3D structures are created from loose powdered polymer using a layer-by-layer approach. Each 2D layer is 'drawn' by the use of a binding solvent to solidify the polymer particles (79). In recent years, some methods for analogous (layer-by-layer or arbitrary freeform shape) fabrication of hydrogels have been developed, using light rather than solvent. However, feature size and architecture is limited (resolution ~ 100 μm, (80)). In a gas foaming approach, carbon dioxide is dissolved in P(L)GA at high pressure, and pores spontaneously form after inducing a pressure drop (81). Alone, this procedure causes a closed pore structure, which for many applications is inadequate. However, gas foaming can be used in combination with particulate leaching, which tends to improve interconnectivity (82). In particulate leaching techniques, porogens such as salt or sugar crystals are used as a template on which to cast polymer-solvent solutions (or are mixed directly with polymer particles) prior to polymerization or fusion of the polymer, then removed by addition of water or another appropriate solvent (83, 84). Depending on the weight fraction of salt and other factors, pores may or may not be interconnected. Ways to increase connectivity in such techniques were recently developed: Murphy et al. fused salt crystals together using a humidified atmosphere prior to casting polymer on the template (85), and Ma et al. exposed paraffin sphere templates to high temperatures to melt the spheres together prior to casting of PLA-co-PGA (and then sphere removal by dissolution in organic solvents) (86).

We took our inspiration from salt leaching techniques because of their simplicity and cost-effectiveness, but wanted to develop a method more suitable for hydrogels. The literature for creating porous hydrogels is less vast than that for hydrophobic polymers, perhaps due to the already good diffusion properties of water-swollen polymers, the fact that some cells may be

encapsulated and grown directly in hydrogels without causing them harm, and also because of the relatively weak mechanical properties of even bulk hydrogels. However, in some cases the lack of macroporosity in typical hydrogel networks may be an impediment to cellular invasion and neovascularization *in vivo*, even when the gel is designed with cross-links that may be cleaved by migrating cells. Porous hydrogels have been made by three primary methods: temperature-induced phase separation (87), templating by solid materials (e.g., fibers) (88, 89), and the use of foaming agents such as carbonates and organic solvents (90). For drug release and other applications, macroporous hydrogel foams have been made using porogens/foaming agents to create highly absorbent structures (91, 92). These foams typically have pores in the 100's of μm, and a high porosity and swelling ratio. However, we were interested in mimicking the 10's of μm scale of the reticular network (see section 1.1.1) with a less swellable and more mechanically strong construct. Further, we were interested in specifying the interconnected architecture exactly, so that all pores would be connected to their neighbors.

In order to achieve such a pore structure, we applied the process of colloidal crystal templating to length scales and materials suitable for tissue engineering. This templating method has previously been used to create ordered arrays of pores at the submicron scale in dieletric materials for photonics applications such as waveguides (93). Two materials are required for this method: particles of an appropriate size that can be arranged into a crystalline array, and the scaffold material that is to comprise the final porous structure. The particles must be removable from the scaffold by solvent etching, calcination, or other techniques. The scaffold material, meanwhile, must be able to coat the template, but then to become stable and hold its shape (e.g., to undergo a liquid to solid transition after addition to the template). The details of colloidal crystal templating are further described in Chapter 2.

1.3.4 Cytokine delivery within scaffolds

A key part of a given biological microenvironment is the presence of soluble factors, such as growth factors and chemokines. In fact, about 12% of genes with known function in the human genome are used for cell signaling and intercellular communication (94). As described earlier (see section 1.2), we hypothesized that delivery of the chemokine CCL21 from a scaffold could promote ectopic lymphoid tissue formation if implanted at a tumor site. Having chosen a material and pore-forming method for such a scaffold, we considered strategies to incorporate cytokines. As with pore formation, the introduction of cytokines into a scaffold system has been accomplished using a wide variety of methods (reviewed in (95-98)).

Three main categories of growth factor incorporation in porous polymer scaffolds may be described: direct mixing of growth factor with polymer, surface attachment of growth factor to polymer, and release of growth factor from a separate delivery device (e.g., microspheres) loaded in the porous matrix. Dr. David Mooney's group alone has explored several strategies for the incorporation of the angiogenesis-promoting factor VEGF in hydrophobic polymers, such as direct mixing with PLGA polymer (99), addition to a mixture of PLGA and alginate to improve protein incorporation efficiency and stability (100), and release from PLGA microspheres within PLGA scaffolds to improve temporal control over release (101). In any delivery system, the method of incorporation may affect how well the bioactivity of the protein is maintained, as well how predictably its release rates can be controlled.

In our case, direct mixing of the cytokine with the polymer was unlikely to work. Although most proteins can survive the short UV exposure required for photopolymerization, in our

fabrication strategy the gel solidification is followed by template leaching in pure acetic acid (described in Ch. 2). This high concentration of acid may denature proteins, or some protein may escape the scaffold and dissolve in the large amount of solvent. Both surface attachment and microsphere release of growth factor, however, should be feasible in our scaffolds. To reduce the components in the system, we began by pursuing surface attachment of chemokine to the cross-linked PEG gels.

PEG gels in non-porous form have been previously studied as growth factor release vehicles by a few groups. For instance, Mann and West reported that PEG-tethered TGF-β (transforming growth factor β) increased matrix production by encapsulated cells better than unmodified TGF-β that was merely physically trapped in PEG hydrogels (102). Gobin and West found similarly good functionality of PEG-tethered EGF (epidermal growth factor) released from degradable hydrogel matrices (103). However, this method might not be expected to work for all cytokines, since chemical modification may destabilize the protein structure or mask the relevant epitope for interaction. One promising strategy for retaining long-term release and functionality using untouched proteins is the inclusion of heparin, which has specific interactions with many molecules of interest. Researchers have implemented a number of strategies to incorporate heparin in gels and in scaffolds, demonstrating that both covalent and non-covalent interactions can prove useful (104-107). Using a PEG-based system, Pratt et al. directly encapsulated BMP-2 (bone morphogenetic protein 2) in hydrogels (77), or instead bound heparin and BMP-2 to the PEG matrix via inclusion of a co-polymerized heparin-binding peptide (108), and found that the presence of heparin improved cytokine activity.

The molecules we are interested in delivering to a specified site, namely chemokines, are known to anchor reversibly to ECM and cell surfaces by binding to heparan sulfate, and have been shown *in vitro* to bind to its analogue heparin (109, 110). CCL21 has especially strong binding to the anionic polymer heparin, due to the chemokine's strong net positive charge at neutral pH (111-114). However, we would expect this ionic complex to dissociate and thus for the scaffold to slowly release CCL21 over time, as the dissociation constant K_D for CCL21-heparin is estimated to be ~ 5 nM (112). It is also possible that surface-bound chemokine may have an effect on cell migration even if it is not released, as has been shown for some chemokines presented by endothelial cells (or cell-mimetic synthetic surfaces) to T cells (25, 115). We thus attached heparin to the surfaces of PEG macroporous hydrogels and used this biopolymer to sequester CCL21 for delivery to cells.

1.3.5 Summary of lymphoid scaffold design

As discussed above, scaffolds for tissue modeling or tissue engineering platforms must fulfill several criteria: biocompatibility, mechanical integrity, as well as high interconnectivity of pores for cell migration and nutrient diffusion. Besides these generalized criteria, scaffolds must also meet the demands of the application at hand. We hypothesized that several key features of the lymph node microenvironment would need to be recapitulated in order for successful use as a therapeutic or modeling construct, as defined by cell viability, migratory capacity, and efficient interactions. Namely, we proposed to model the unique macroporous architecture, cellular composition, and ECM or integrin ligands presented in the lymph node, and to study the effects of systematic variation of these parameters.

For this effort, we decided to develop and implement a novel templating method for fabricating macroporous hydrogels. We chose PEG as the primary material component due to its

protein-resistant properties, ability to be quickly undergo gelation via photopolymerization, and ease of chemical modification. This final property makes for ready incorporation of specific bioactivity by co-polymerization as well as post-polymerization modifications. In order to create highly interconnected pores in a hydrogel, we planned to modify the typical particulate leaching paradigm by creating ordered arrays of pores rather than relying on random arrangements of the templating material. We planned to achieve this by creating colloidal crystal templates from polymer microspheres with diameters on the 10's of μm scale. Over the course of this project, several iterations of scaffolds were made: peptide-modified, protein-modified, composite scaffolds filled with collagen gel, and finally scaffolds for chemokine delivery. By creating macroporous gels that could be modified with adhesion and signaling proteins, we sought to mimic the architecture and biochemical composition of the lymph node.

1.4 Lymphoid scaffolds: motivation and significance

Two types of applications for lymphoid scaffolds may be envisioned: those that use an *in vitro* tissue model to study fundamental questions in immune biology, and those that intend to ultimately make scaffolds effective in clinical therapies.

We initially focused on the first goal. In particular, we were interested in the role of the lymphoid microenvironment in shaping T cell migration and the kinetics of priming by DCs. Several years ago, these signals were not well-defined, and a systematic study in an *in vitro* model seemed a promising approach. Specifically, factors affecting migration within lymph nodes were far less well understood than those that drive homing to lymph nodes. Very recently, intravital microscopy of murine lymph nodes, in concert with the ever-growing development of transgenic mouse models, has shed light on several of the questions we intended to study. For example, we originally proposed to investigate what migration strategies T cells use to sample dendritic cells for antigen, by creating environments where we defined the relative numbers of polyclonal T cells, antigen-specific T cells, antigen-bearing DCs, and DCs lacking antigen. Such ratios could long be defined *in vivo* by adoptive transfer strategies, but only recently could they also be imaged in live animals. In 2003, Miller et al. showed that basal T cell migration appears random, and that the search for antigen occurs by a stochastic process (116). Some have hypothesized that cell organization, particularly placement of incoming antigen-bearing DCs near HEVs (which is also where T cells enter lymph nodes) helps to make random sampling efficient enough to promote immune responses (117). In contrast to the random migration hypothesis, more recently Dr. Ronald Germain's group has shown that small localized chemokine gradients can influence cell migration to an extent, because $CD8^+$ T cells are attracted to antigen-presenting DCs more than would be expected by chance if $CD4^+$ T cells are also present (118). At this stage, the remaining questions in T cell migration are subtle and involve the simultaneous tracking of many cell populations, which can only reasonably be done by 2-photon microscopy, whether *in vivo* or *in vitro*.

Although we perceived a diminished need for an *in vitro* model, one could imagine such a construct nevertheless being useful for studies of human immune cells, which clearly cannot be studied by intravital methods. However, the second issue faced during the course of this project was design complexity, and subsequent lack of reproducibility. Despite the complexity of the multi-step fabrication process, the model was still quite simplified compared to a real lymph node, and further modifications were likely to result in further compromised reproducibility.

Despite these setbacks, it became clear that our scaffold system could be well-suited to use in tissue engineering for immunotherapy (see section 1.2). Immune-based therapeutics are a promising area of research, and constructs that boost immunity during cancer are particularly of interest. As an alternative to cytokine injection and targeting methods, we pursued a scaffold-based method for creating an environment supportive of robust T cell migration. Suematsu et al. were the first to describe and carry-out a scaffold-based lymphoid tissue-engineering strategy in 2004; however, at present their system appears to require delivery of genetically engineered stromal cells in order to have lymphoid induction properties (119, 120). Our scaffold system represents an attempt at developing a lymphoid tissue engineering system free of all but autologous cells.

In the immunotherapy framework, some requirements on the scaffold would be relaxed while other new ones would arise. Specifically, the need for exact mimicry of the lymph node T zone would be reduced. Rather, we would create an intermediate-stage scaffold meant to induce further modifications in its surrounding environment, resulting finally in a lymph node-like structure. We maintained our goal of studying T cell migration in varying microenvironments, but now allowed the means toward the end result of robust migration to be less mimetic. Thus, rather than attempting to find the protein-cell combinations and densities that could allow migration in an open porous architecture similar to the reticular network, we ultimately used the well-known migration substrate collagen to make a composite scaffold. In this structure, collagen was infused in the porous PEG-based hydrogel and then heated to form a fibrillar gel. Such tightly woven collagen nanofibers are uncharacteristic of the T zone area of the lymph node, thus reducing the mimetic properties we originally envisioned, but can support T cell migration and priming. Meanwhile, the porous scaffold provided superior mechanical properties compared to collagen alone, as well as the potential for cytokine delivery.

Besides the composite structure, the main novel aspect we introduced for tissue engineering (as opposed to *in vitro* model) scaffolds was the incorporation of motility factors onto the scaffold surface. As described in section 1.2, scaffolds for immunotherapy could be used with adoptively transferred cells, whose motility and function should be maintained by an appropriate microenvironment, and attracting host cells to the scaffold could be desired as well. Delivery of CCL21 would be ideal in this type of application, because CCL21 can stimulate both chemotaxis (for attracting new cells) and also, as we discovered, potent chemokinesis (for sustained migration of cells initially placed within the construct), along with playing a role in formation of neotissues (see sections 1.1.3, 1.2, and Chapter 3). One new requirement that we did not yet address in more than a preliminary way is that of degradability; that is, most of the work was done with non-degradable scaffolds intended for an *in vitro* model, and for comparison purposes this was continued throughout the entire thesis. However, minor modifications to the scaffold chemistry could be made in the future by co-polymerization of enzyme-sensitive linkage; these peptide fragments would allow the polymer network to be degraded by natural proteases (76).

At this time, we showed that our scaffolds are a supportive environment for T cell migration, and performed some initial studies demonstrating dendritic cell and stromal cell spreading and viability in these constructs. In the future, cell invasion studies and more complete determination of chemokine delivery parameters should be performed, followed by *in vivo* studies of functionality.

1.5 Overall Objectives and Specific Aims

The purpose of this thesis was to design and fabricate a novel scaffold appropriate for lymph node tissue engineering, and to perform some initial studies of lymphoid cell behavior in this model lymph node T zone construct. The revised specific aims were as follows:

1) Develop porous polymeric scaffold for model T zone.
    a. Select appropriate materials and design and implement a fabrication process.
    b. Characterize the morphology and mechanical properties of the resulting scaffold.
2) Study factors that are known to influence T cell motility.
    a. Determine effect of homeostatic chemokines on lymphocytes interacting with 2D substrates, with or without adhesion proteins.
    b. Study whether chemokines have an ultimate effect on T cell activation.
3) Integrate lymphoid cells into scaffold.
    a. Develop cell loading procedures for T cells, DCs, and fibroblasts.
    b. Examine response of cells to scaffold and improve design accordingly.
4) Carry out a systematic study of scaffold parameters on T cell motility.
    a. Determine effect of coating scaffold with two important protein ligands.
    b. Study effect of pore size in final chosen (composite) scaffold construct.
5) Develop initial system for releasing chemokine from the scaffold.

The above experiments would be a first step in investigating what types of scaffolds are appropriate for lymphoid tissue engineering, and in determining what factors may best be exploited in a 3D environment to influence T cell motility.

2 Development of inverse opal scaffolds for model lymph node 'T zone'

2.1 Introduction

For the reasons outlined in section 1.3.2, hydrogels are a class of materials well-suited for engineering soft tissues with a high water content, including lymphoid tissues. Briefly, hydrogels mimic the elasticity and permeability of such tissues, and also are easily conjugated with functional moieties. In particular, protein-resistant PEGs that are modified with peptides or other bioactive signals provide a flexible platform for developing tissue engineering strategies. Such gels have been used to encapsulate cells and growth factors for cartilage and other tissue engineering applications (66, 67, 77, 78, 121, 122), as well as for models of cell migration (103, 122).

An encapsulation strategy may not be appropriate for all cells and tissues, however. These bioactive PEG gels have primarily been made using radical photopolymerization, and toxicity to cells varies both with photoinitiator used (and its concentration) and the cell type (123, 124). In our experience with lymphocytes, they are sensitive to even mildly cytotoxic compounds (e.g., some fluorescent dyes) and viability of gel-encapsulated lymphocytes might be difficult to maintain. Further, unlike many soft tissues that have a dense ECM, the reticular networks of secondary lymphoid organs comprise a loosely woven fibrous network; we were initially interested in mimicking this macroporous architecture (see section 1.1.1). Finally, despite the relatively good diffusivity within water-swollen hydrogels, diffusion of nutrients and oxygen could be further improved by the introduction of porosity.

Altogether, bioactive hydrogels having a cellular structure of interconnecting macropores would be attractive scaffolds for drug delivery and tissue engineering, by combining tissue-like elasticity with enhanced pathways for mass transport and cell migration (64, 125-127). However, to obtain high degrees of pore interconnectivity using available stochastic porogen methods (developed primarily for hydrophobic thermoplastic polymers), void fractions exceeding 95% must be introduced (85, 99, 128, 129). This high porosity causes severe deterioration of the polymer's mechanical properties, such that only a limited selection of stiff materials can be utilized and still maintain tissue-like moduli after processing (126, 130). In this chapter we describe the development of a method to prepare soft hydrogels with interconnected porosity at moderate (~ 65%) void fractions, thus maintaining compressive stiffnesses comparable to native tissues. This was achieved by fabricating gels with ordered, interconnected macrovoids (20-60 μm diameter) via colloidal crystal templating.

Colloidal crystal templating has been extensively applied in the field of photonics to fabricate materials with periodic variations in refractive index, as well as in membranes, chromatography media, and solid-phase catalysis substrates (131-134). The colloidal template is comprised of a crystalline arrangement of monodisperse microspheres (typically silica or polystyrene), which can be used as an extractable template for the fabrication of inorganics, metals, or polymers having close-packed voids of ~0.05-5 μm diameter (commonly referred to as inverse opal structures). Such structures have features which, if adapted to appropriate length scales, would be of great interest as scaffolds for tissue engineering: a monodisperse open cellular structure;

potentially perfect, ordered connectivity between voids; and improved mechanical properties compared to more porous (and typically less interconnected) structures generated by stochastic porogen methods.

Two ubiquitous biomaterials, cross-linked poly(ethylene glycol) and gelatin, were templated. As described above and in section 1.3.2, bioactive PEG gels have been extensively used in tissue engineering and drug delivery applications, but to our knowledge always in solid gel form thus far. Gelatin has the same attractive properties of hydrogels that synthetic PEGs have, and unlike PEG, it has inherent bioactivity and biodegradability. It also has inferior mechanical properties and other drawbacks (as described in section 1.3.2), but nevertheless is useful as a biomaterial, particularly for drug delivery (70). The generality of the colloidal templating approach should make it applicable to materials of interest for a broad range of bioengineering applications.

Preliminary experiments that we conducted to examine cell behavior in these novel scaffolds utilized PEG gels modified with RGD peptide. However, since this most commonly investigated adhesion sequence was of no use for most subsets of lymphoid cells, we later developed methods to attach whole proteins to the scaffolds. The studies of cell responses to these scaffolds are described in Chapter 4.

2.2 Materials and Methods

2.2.1 Preparation of colloidal crystal templates

A suspension of monodisperse poly(methyl methacrylate) (PMMA) microspheres (Fluka) was concentrated to ~65% solids in 70% aqueous ethanol. The microsphere suspension (30-50 μL total in 2-3 additions) was deposited in 4.8 mm diameter poly(dimethyl siloxane) wells adhered to glass slides, and agitated until dry (2-4 h) at 400-450 rpm on a 3/8 inch orbit shaker (IKA) at 20 °C. Partially ordered templates were then resuspended a second time directly in the wells, and shaken/dried to form well-ordered crystals. A range of microsphere concentrations and shaker speeds was acceptable for forming crystals; the above text describes the method we used most recently that gave the most consistent results.

2.2.2 Preparation of sintered templates

PMMA templates were prepared per section 2.2.1, then placed in a pre-heated oven (200 °C) for 0, 8, 16, or 24 h. To avoid melting under force of gravity in any one direction for too long, scaffolds were turned five times at near-equal time intervals, such that they melted first with the coverslip face down, and once resting on each of the four edges of the coverslip.

2.2.3 Preparation of PEG scaffolds

Chemicals were from Sigma-Aldrich and used as received unless otherwise noted. A hydrogel precursor solution was prepared containing 20 % (w/v) PEG dimethacrylate (PEGDMA, 1000 Da, Polysciences), 0.15 M triethylamine, and 0.8 % hexyl phenyl ketone photoinitiator in 3:1 (v/v) pH 7.4 HEPES buffer (4-(2-hydroxyethyl)piperazine-1-ethansulfonic acid-buffered saline) and ethanol. The precursor (10-12 μL) was gently pipetted onto a colloidal template, perfused by centrifugation (2 min, 1500 rpm), and exposed to UV light (365 nm, 12 mW/cm^2) for 90 seconds to polymerize the liquid into a gel. The polymerized construct was transferred to acetic acid to dissolve the microspheres over 48 hrs, to phosphate-buffered saline pH 7.4 (PBS) for 24 h, then

briefly sterilized in 70% aqueous ethanol and finally equilibrated in sterile PBS. The final synthesis conditions we chose were described above; however, some experiments were performed with 875 Da PEG, varying concentrations of ethanol, and/or 2,2-dimethyl-2-phenyl-acetophenone as the radical initiator.

2.2.4 Preparation of functional PEG scaffolds

Fluorescent scaffolds were prepared by including 0.003 wt % methacryloxethyl thiocarbonyl rhodamine (Polysciences) in the gel precursor solution. To prepare peptide-containing bioactive scaffolds, hydrogel precursor solution containing 1:160 mol:mol RGD-PEGA:PEGDMA was polymerized around colloidal crystal templates as before. Peptide-modified PEG acrylates (RGD-PEGA) were prepared by reacting 0.5 molar excess acryloyl-PEG-N-hydroxy-succinimide (PEGA-NHS, 3400 Da, Nektar Therapeutics) with the adhesion peptide (135) GWGRGDSP or a control peptide GWGRDGSP (MIT Biopolymers Laboratory) in 0.1 M sodium bicarbonate buffer (pH 8.3) for 2 h at 20 °C, then dialyzing overnight to remove excess PEGA-NHS (3500 Da cutoff dialysis cassettes, Pierce) (122). Finally, the RGD-PEGA was filtered, lyophilized, resuspended at ~40 mg/mL, and stored at –20 °C.

2.2.5 Preparation of scaffolds for SEM

PEG scaffolds were serially dehydrated (10, 25, 50, 75, and 90% ethanol at 10 min each; 100% overnight), razor-cut, and observed using a LEO VP-438 at 5kV. Gelatin scaffolds were frozen in liquid nitrogen, fractured, and lyophilized for 24 h prior to observation with a LEO VP-438, which was used in variable pressure mode (20 Pa) at 20 kV.

2.2.6 Confocal microscopy

Fluorescent scaffolds were observed using a Zeiss LSM 510 with either a 40X Apochromat water-corrected objective, or a 40X Acroplan water-immersion objective.

2.2.7 Mechanical properties testing:

Compressive moduli of hydrated PEG and gelatin scaffolds were measured at a constant strain rate (5 μm/s) using a precision motor stage (Micromechanics, UK) and a 25 g load cell (Transducer Techniques, CA). Data is reported as mean ± standard error for three scaffolds per condition.

2.2.8 Preparation of gelatin scaffolds

PMMA templates were heated to 70 °C and pre-wet with 70% ethanol, after which gelatin solution at 70 °C (Sigma Type A, ~ 300 Bloom, 200 mg/mL, prepared in 25% aqueous ethanol) was immediately added and perfused by centrifugation (5 min, 2000 rpm, 30 °C). After cooling to room temperature for 30 minutes, gels were flash frozen in liquid nitrogen and lyophilized overnight. Dehydrated gels were then treated with EDC and NHS (0.20 mM *N*-Ethyl-*N*'-(3-dimethylaminopropyl)carbodiimide and 0.07 mM N-hydroxysuccinimide for 3 hrs at 20 °C) to form covalent cross-links that remain stable during template dissolution (136). After the PMMA template was dissolved in acetic acid, the construct was rinsed and equilibrated in PBS pH 7.4.

2.2.9 Observation of scaffolds made using sintered templates

Fluorescent scaffolds were prepared as usual from the sintered templates, then observed on a Zeiss LSM 510 confocal microscope using a water-immersion objective (0.8 numerical aperture). Five 210x210x~70 μm 3D fields were observed per scaffold, with successive z-plane images collected at ~1 μm increments. Each field was observed in Volocity software (Improvision, Inc.), and throat pore diameters were quantified by observation of the *y-z* plane at the *x* location that gave the smallest pore diameter for any given pore. Two independent experiments were performed with similar results, examining 70-100 pores per scaffold.

2.3 Results

2.3.1 Scaffold development: materials and fabrication

As a basis to develop a porous artificial lymphoid tissue construct, we used a synthesis pioneered by West and Hubbell for solid gels (76), in which PEG diacrylates are co-polymerized with peptide-PEG monoacrylates in order to present tethered adhesion sequences (see Figure 2-1).

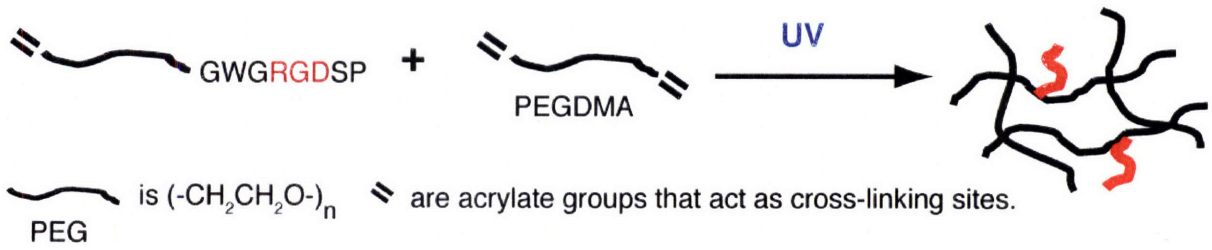

Figure 2-1 **Schematic of hydrogel polymerization chemistry.** PEG-monoacrylates conjugated to adhesion peptides such as RGD were copolymerized with PEG-dimethacrylate (PEGDMA) to form a cross-linked PEG gel network with surface adhesion peptide presentation.

Several changes were made to the original protocol developed by West. First, a lower molecular weight PEG than 4000-6000 Da was used, in order to strengthen mechanical properties, which would be relatively weakened by the proposed porous structure. We tested both 1000 Da and 875 Da PEGDMA. Second, the PEG precursor solution was prepared in a mixture of saline buffer solution and ethanol rather than in pure buffer. The use of ethanol improved wetting of the colloidal template by the pre-polymer solution, due to the alcohol's reduced surface energy compared to water. Better wetting would in turn be expected to reduce defects caused by incomplete penetration of the polymer into the template.

We found that ethanol also dramatically enhanced the transparency of the final product, when we performed initial testing of different formulations with thick bulk gels (rather than thin porous scaffolds). Transparency was a desirable quality due to the reliance of the ultimate project on many imaging studies (e.g., of cell migration within scaffolds). The reason for the observed improvement in transparency might be due to the breaking up or alternative organization of PEG

micelles; such micelles are known to occur in aqueous solutions of acrylate PEGs and promote their polymerization (137).

Finally, the photoinitiator 1-hydroxy-cyclohexyl-phenyl-ketone (HPK) was used rather than 2,2-dimethyl-2-phenyl-acetophenone (DMPA). Although HPK does not work as rapidly as DMPA, its solubility in aqueous ethanol rather than the organic N-vinyl pyrrolidone is attractive for creating a homogeneous solution and ultimately transparent product. Table 2-1 shows the transparency of different PEG formulations.

Table 2-1 **Transparency of different gel formulations.**

PEG MW	Initiator	Ethanol (%)	Resulting Gel
875	DMPA	25-50	opaque
875	HPK	25-50	opaque
1000	DMPA	25-50	opaque
1000	HPK	25-50	transparent

Although the presence of ethanol enhanced gel transparency, it also increased the polymerization time needed to form a gel, and decreased the mechanical properties (as ascertained by qualitative observation of gels). Stiff gels were formed when using 0-25% ethanol, soft gels were formed using 50% ethanol, and gelation did not occur when using 75-100% ethanol. Thus, we used 25% ethanol in our final precursor solution formulation.

Having settled on the conditions for polymerization of our system, we next focused our attention to developing a fabrication method for creating interconnected pores in the gel. To adapt colloidal crystal templating to the fabrication of tissue engineering scaffolds appropriate for the migration and growth of living cells within the structure, we prepared 1-2 mm-thick templates from monodisperse polymer microspheres with 20-60 μm diameters (see Figure 2-2). Colloidal crystal templates can be prepared from submicron-diameter particle suspensions simply by controlled evaporation, with random thermal motion enabling the spheres to evolve to close-packed structures as they are concentrated (132, 133). For the large microspheres used in our templates, however, Brownian forces were insufficient to promote ordering: controlled evaporation alone did not lead to close packing of large microspheres, resulting in imperfect templated gel structures (138). To overcome this problem and achieve highly-ordered colloidal templates, we incubated microspheres suspended in aqueous ethanol solutions atop an orbital shaker, and allowed them to dry. We had also attempted thermal methods to allow spheres to reach their equilibrium state, but found that continuous mechanical agitation worked best. Smaller microsphere sizes tended to form crystals somewhat less easily than larger ones, requiring higher speeds and higher particle densities to do so reliably.

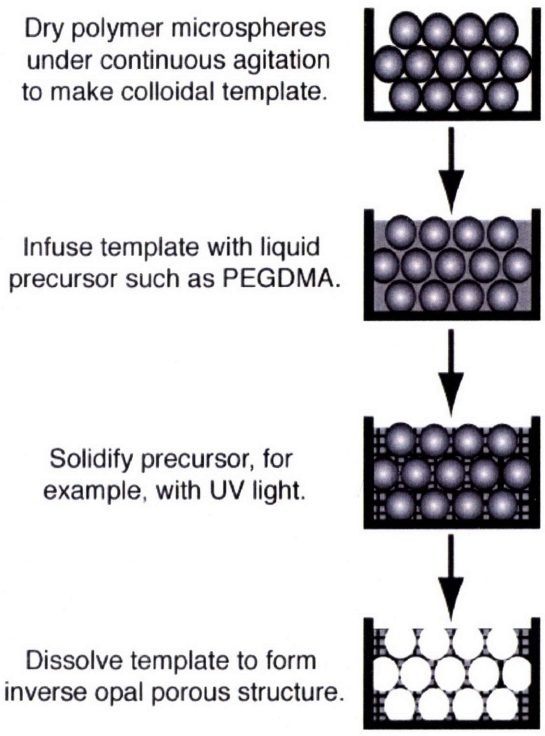

Figure 2-2 **Schematic of colloidal crystal templating process for hydrogels.**

Finally, we needed to select a solvent that would dissolve the PMMA microspheres without having an adverse effect on the surrounding PEG gel. We wanted to avoid the use of harsh organic solvents that might be difficult to fully remove from the gel, and thus might cause cytotoxicity problems for cells added to the scaffolds later on. Acetic acid was chosen because of its high solubility in water, and the fact that in very low amounts it is not harmful to cells. A sample scaffold made using the chemistry and procedures described above is shown in Figure 2-3 below.

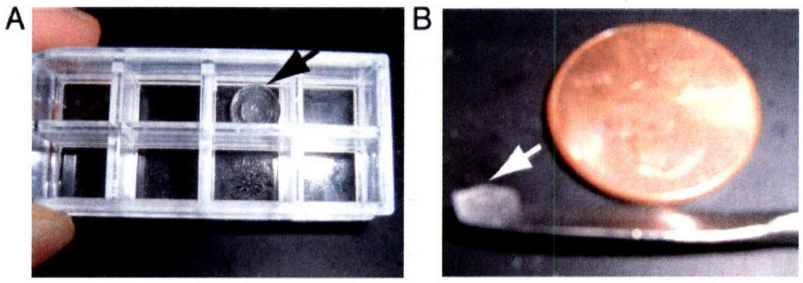

Figure 2-3 **Macroscopic appearance of lymphoid scaffolds.** Digital micrographs showing the top (A) and side (B) views of a typical scaffold. Scaffolds are indicated by arrows.

2.3.2 Scaffold characterization: morphology

The morphology of templated PEG hydrogels was examined by optical, fluorescence, and scanning electron microscopy. The few layers nearest to the surface of the scaffold could be examined in the hydrated state by optical microscopy. Brightfield micrographs demonstrate the long-range, hexagonally close-packed order of the main pores, whose diameter was exactly determined by the size of the templating spheres (Figure 2-4A). Ordered cellular structures could be made with pores at least as small as eight and at least as large as eighty microns.

In order to look slightly deeper into the scaffolds, and more importantly to probe the structure in three dimensions, confocal fluorescence microscopy was utilized on scaffolds doped with a rhodamine methacrylate. Regions of sphere-sphere contact in the original template created ordered arrays of inter-cell pores. These interconnecting throat pores were visible even in the *x-y* plane, as a break in fluorescence in between struts (Figure 2-4B). Scaffolds typically had ~78% of the pores expected for a perfect structure, as determined by counting visible breaks in multiple image fields; this is well above the threshold for a fully percolating structure (139, 140). Serial *x-y* confocal images were taken in fine-grained (c. 1 μm) steps to allow for 3D computational reconstruction, which gave a clearer view of throat pores on edge (Figure 2-4C, D). A quantitative measure of overall porosity was obtained by determining scaffold volumes from multiple confocal 3D intensity-thresholded fields covering a total volume of 0.005 mm^3. Scaffolds formed from 20 μm diameter sphere templates had 65 ± 3% porosity, somewhat lower than the theoretical value of 74% due to defects, though many ~25x20 μm areas had 70-73% porosity. The major defect observed in structures was imperfections in packing that caused lateral inter-cell pores to be missing.

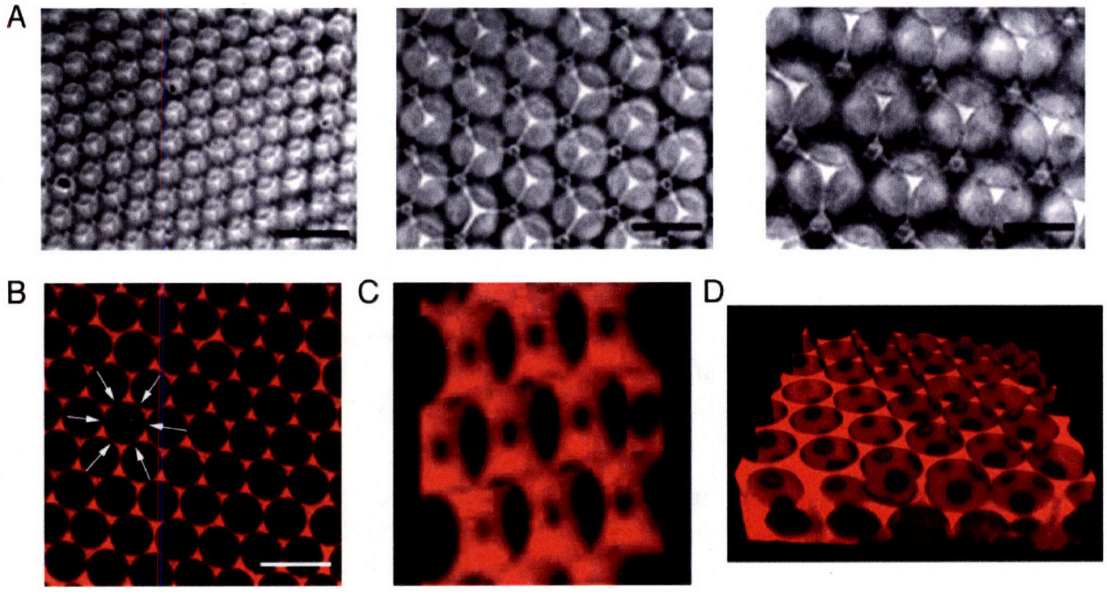

Figure 2-4 **Morphology of scaffolds in the hydrated state.** (A) Brightfield optical micrographs taken within hydrated PEG gels templated with 20, 40, or 60 μm diameter microspheres (scale bars 50 μm). (B) Confocal image of a fluorescently labeled, hydrated PEG scaffold taken through the mid-plane of a single layer within the structure (scale bar 40 μm). Breaks in fluorescence intensity around each void of the structure occur at open throat pores (denoted for

one void with arrows). (C) 3D reconstruction of serial *z*-section confocal images taken in 0.5 μm steps shows the lateral throat pores formed at points of sphere-sphere contact in the colloidal crystal template: a small section of one scaffold layer is shown at a 135° angle. (D) A 3D reconstruction of a fuller section of scaffold (210x210x55 μm) is shown.

To probe morphology within the center of mm-thick structures, cross-sections of dehydrated scaffolds were also examined by scanning electron microscopy (SEM). Upon dehydration, scaffolds shrank by ~ 40% (determined by comparison of confocal images of hydrated scaffolds to dehydrated EM images), but did so uniformly. Scaffold pores were close-packed and interconnected for distances spanning tens of layers (Figure 2-5A). Further, the surface of the scaffold was primarily open, with small pores resulting from the incomplete penetration of the precursor solution to the contact areas between templating spheres and the surface of the glass they were fabricated on (Figure 2-5, B-C). This open surface is in contrast to some stochastic porogen methods used for fabrication of tissue engineering scaffolds that create dense or nonporous skin layers which may block entry of cells into implanted structures (81, 141). However, the openness of the surface was highly dependent on the amount of polymer added to the template, and a partial skin of bulk gel sometimes formed if excess polymer was used.

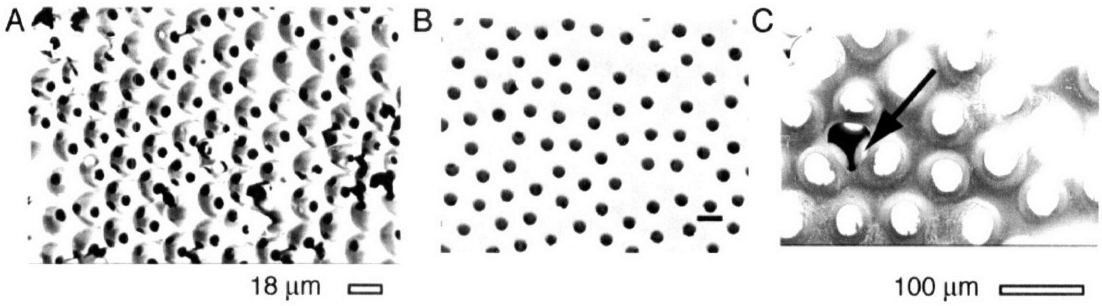

Figure 2-5 **Morphology of scaffold cross-sections and surfaces.** (A-B) Scanning electron micrographs of dehydrated scaffolds. (A) A cross-section spanning over ten layers of a scaffold made with a 20 μm void size is shown (scale bar 18 μm, corrected for shrinkage due to dehydration; 10 μm uncorrected). (B) Free surfaces of scaffolds also exhibited arrays of pores, as illustrated by this scaffold with a 20 μm void size (scale bar 20 μm, corrected). (C) Scanning electron micrograph of a lyophilized scaffold-template construct prior to sphere dissolution. The exposed microsphere surfaces are visible as bright spots. A small hole in the scaffold shows the microsphere bodies below (arrow). Scale bar 100 μm, uncorrected.

The size of the interconnecting throat pores was determined by software-aided analysis of SEM micrographs. The inter-layer throat pore size was consistently found to be ~25% of the main void size, as shown in Table 2-2. Thus, templated scaffolds with 40 μm or greater void size had throat pore diameters ≥ 10 μm, consistent with those reported to support tissue invasion *in vivo* (142-144).

Table 2-2 **Templated PEG scaffold pore sizes.**

Nominal cell size (μm)	Dehydrated throat pore diameter (μm)	Throat pore diameter, corrected[a] (μm)	No. pores examined
20	2.94 ± 0.57	5.15 ± 1.00	53
40	5.53 ± 0.87	9.67 ± 1.53	111
60	8.86 ± 1.81	15.5 ± 3.17	116

[a]Throat pore size determined from SEM micrographs of scaffolds was corrected by dividing by the fractional shrinkage observed in the dehydrated structure relative to the dimensions of the hydrated scaffold measured *in situ* by confocal microscopy.

2.3.3 Scaffold characterization: mechanical properties

The high degree of void interconnectivity observed in templated gels was achieved at significantly lower total porosities than are required in stochastic porogen methods (due to the ordered arrangement of void space), and this resulted in quantifiably improved mechanical properties. The compressive modulus of the original composition of gel precursor solution (PEGDMA and 0.6 mole % RGD-PEGA, see 2.2.3-2.2.4) was measured for the bulk gel and for scaffolds with three different pore sizes, and compared to theoretical predictions. Using a model of bending response in porous structures, Gibson and Ashby derived a relationship between the elastic modulus of cellular materials ($E_{cellular}$) and their solid counterparts (E_{solid}):

$$\frac{E_{cellular}}{E_{solid}} = C(1-P)^2 \qquad (1)$$

where C is a constant (typically ≈ 1) and P is the porosity. Equation (1) predicts the modulus of structures with 95-99% porosity to be 0.25%-0.01% of the bulk solid, in agreement with reported data on tissue engineering scaffolds (85, 128, 129). Such porosity levels lead to extremely low moduli for soft hydrogel structures, and thus prior studies of macroporous soft gels have thus typically been confined to small void sizes (127, 145) (≤ 15 μm) and/or low total porosities (146, 147) (≤ 35%). Compressive moduli of our templated PEG hydrogels in the hydrated state were found to be comparable to soft tissues, which range from ~1 to a few tens of kPa (148, 149). According to equation (1), $E_{templated}/E_{solid} = 0.120 \pm 0.05$ for the PEG hydrogels, which indicates ~ 65% porosity, in agreement with the results from confocal analysis described in the previous section. (A value of 0.067 would be predicted for close-packed void structures with the maximal theoretical porosity of 74%). Thus, the templated structure combines excellent cell interconnectivity with relative stiffnesses 10-1000-fold greater than those predicted for disordered structures, where high porosity is requisite for high interconnectivity ($E_{74\%\ porous}/E_{99\%\ porous} \approx 676$).

Table 2-3 **Templated PEG scaffold compressive moduli.**

Nominal cell size (μm)	Compressive modulus[a] (kPa)
20	16.0 ± 4.3
40	18.0 ± 4.2
60	22.6 ± 5.0

[a]Modulus of non-templated PEG hydrogel was 160 ± 53 kPa.

2.3.4 Generality of CCT approach for tissue engineering: gelatin scaffolds

An attractive feature of the colloidal crystal templating (CCT) approach is its potentially broad applicability for scaffold fabrication: any aqueous solution undergoing a permanent liquid-to-solid transition can in principle be templated with an ordered microstructure. To demonstrate this, we also templated the biological hydrogel formed by gelatin, by introducing heated gelatin solution into a colloidal template as done for the synthetic PEG hydrogels, and solidifying the solution by cooling followed by carbodiimide crosslinking (Figure 2-6).

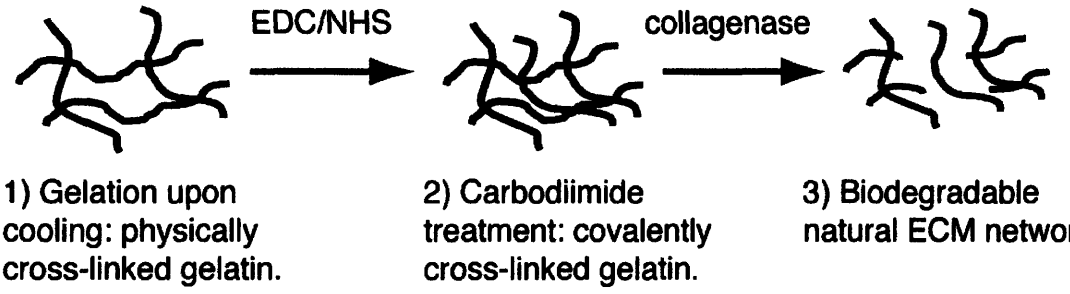

Figure 2-6 **Schematic of gelatin scaffold life-cycle.**

Gelatin hydrogels prepared in this manner were examined by optical and electron microscopy. Upon extraction of the templating microspheres, an ordered gelatin scaffold with interconnecting pores remained, as shown in the brightfield and electron micrographs of Figure 2-7. Throat pore diameters were consistently ~ 40% of the nominal pore diameter (cf. ~ 25% for PEG gels), thus creating large pathways for cell migration even at the minimum 20 μm void diameter, as shown in Table 2-4. Acetic acid treatment of the gelatin scaffolds did not negatively impact cell attachment to the templated scaffolds: NR6 fibroblasts and primary T cells attached and migrated within the ECM scaffolds as in the RGD-PEG scaffolds (see Chapter 4, and data not shown). Compressive moduli of gelatin scaffolds were determined as for the PEG gels, and mechanical properties, though reduced, remained suitable for mimicking soft tissues (see Table 2-4). Further, the drop in modulus from bulk to porous gelatin was again consistent with the Gibson-Ashby theory, with $E_{templated}/E_{solid} = 0.100 \pm 0.026$. Similar fabrication approaches should make the colloidal crystal templating technique applicable to a variety of biomaterials.

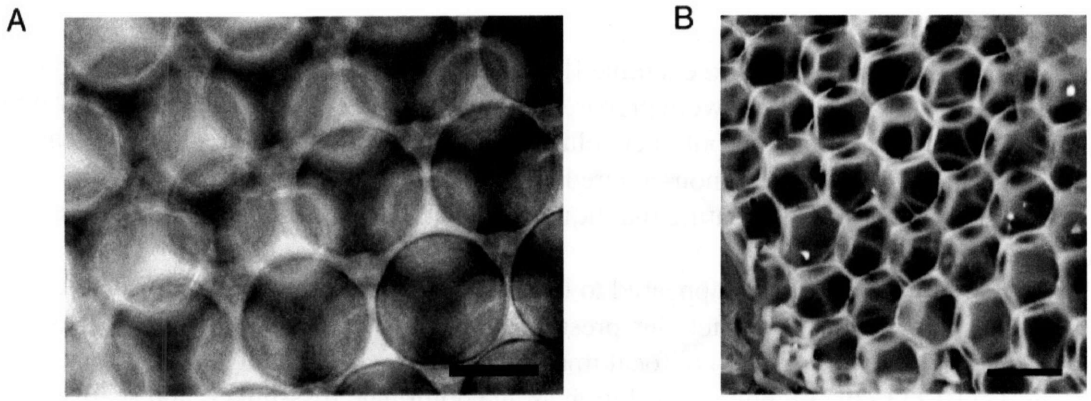

Figure 2-7 **Morphology of templated gelatin scaffolds.** (A) Brightfield optical micrograph of hydrated gelatin scaffold templated with 60 μm diameter microspheres (scale bar 40 μm). (B) SEM micrograph of freeze-fractured gelatin scaffold with 20 μm void size (scale bar 40 μm).

Table 2-4 **Templated gelatin scaffold pore sizes and compressive moduli.**

Nominal cell size (μm)	Throat pore diameter (μm)[a]	No. pores examined	Compressive modulus[b] (kPa)
20	8.82 ± 2.66	54	3.1 ± 0.7
40	16.7 ± 4.28	49	3.3 ± 1.7
60	21.8 ± 5.50	50	5.0 ± 2.5

[a] Corrected for shrinkage due to dehydration.
[b] Modulus of non-porous gelatin was 37.5 ± 13.7 kPa

2.3.5 Control over porosity at multiple length scales by sintering

The exact architecture of the scaffold pores was influenced both by the preparation of a microsphere template and by the subsequent infusion of a liquid precursor solution. Two length scales are of interest: the diameter of the main pore chamber, which was determined almost perfectly by the size of the templating microsphere, and the diameter of the interconnecting pores between chambers, which depended on a variety of factors, as outlined below.

In comparing hydrogel scaffolds prepared from PEG with those prepared from gelatin, it became apparent the relative size of the interconnecting pores depended on the material comprising the scaffold. In the case of PEG, interconnecting pores were typically 25 % of the nominal pore diameter (Table 2-3), while for gelatin this proportional size was 40%. A number of factors might contribute to this, such as relative surface energies and thus energy of adhesion between PMMA and PEG versus PMMA and gelatin, as well as differences in viscosity, vapor pressure, and related parameters.

Although these solid-liquid interactions (related to wetting) were very important, we reasoned that we could have some control over the throat pores by altering the structure of the templating spheres themselves. Specifically, we sought to increase the surface area of the contact points between spheres, where liquids do not tend to fully penetrate. This area could be increased by annealing the template at elevated temperature, a process known as sintering. Others have

described increased neck size in sintered PMMA microspheres that are about ten-fold larger in diameter than the ones used in our studies (150).

Confocal microscopy was used to examine fluorescent (rhodamine-doped) scaffolds prepared from sintered templates. Templates were prepared as usual, then kept in a heated oven for up to 24 hours prior to addition of the prepolymer solution. Sintered templates did not imbibe the precursor solution as quickly as did non-sintered templates; however, ultimate scaffold thicknesses were comparable, indicating that liquid did eventually reach the bottom of the template during centrifugation.

In initial experiments, sintering appeared to have a detrimental effect on the mechanical properties of the final scaffold product, due presumably to the increase in porosity. Scaffolds were soft and appeared collapsed in confocal images. This was corrected by adding 2 wt % bis/acrylamide (19:1) to the prepolymer solution as an additional cross-linker, and scaffolds made from this formulation were observed in an un-collapsed state. Confocal microscopy was used to obtain serial sections of these scaffolds, and the size of the intra-layer interconnecting throat pores was measured within reconstructed *y-z* planes using Volocity software. Figure 2-8 shows *x-y* and *y-z* views of non-sintered and sintered scaffolds. In the *x-y* views, the struts are clearly thicker in the non-sintered scaffolds, while in the *y-z* views the throat pores clearly have smaller average diameter.

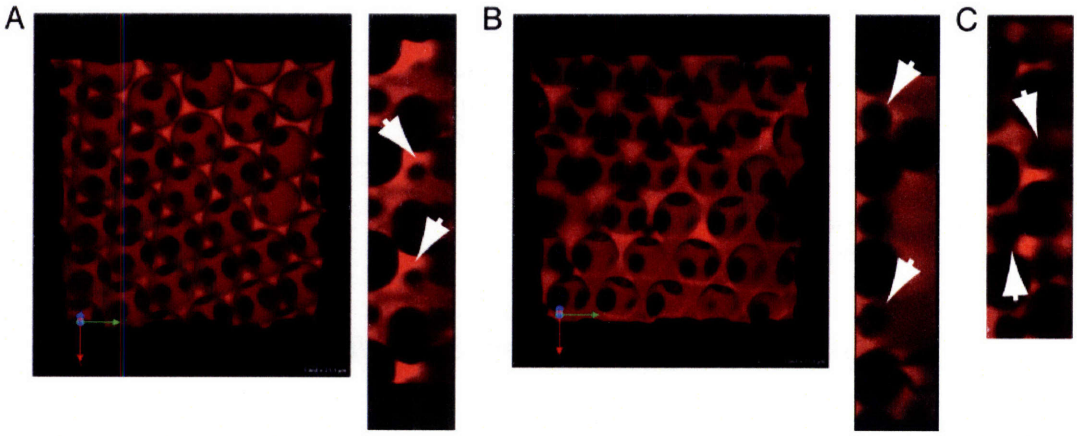

Figure 2-8 **Morphology of sintered scaffolds.** (A) Surface (*x-y*) and edge (*y-z*) views of non-sintered scaffolds. Struts between pores are relatively thick, and interconnecting pores are relatively small. (B) Surface and edge views for a scaffold made from a 24 h sintered template. Struts between pores are relatively thinner than for non-sintered scaffolds, though the bottom half of the *x-y* view exhibits some missing-pore defects. The side view demonstrates large throat pores, but also a large area of polymer without any pores. (C) A template sintered for 16 h was used to acquire this side view. Throat pores are comparably large, but defects in this area are less than in the 24 h case. White arrowheads indicate intra-layer throat pores.

We quantified the correlation between sintering time and resultant throat pore size when annealing at temperatures just below the glass transition temperature of PMMA (c. 200 °C), and the results are shown in Table 2-5 below. The average increase in pore size for the longest sintered template compared to an unmodified one is ~34%.

Table 2-5 **Sintering colloidal templates increases resulting scaffold throat pore size.**

Time sintered (h)	Throat pore size[a] (μm)
0	10.2 ± 1.9
8	10.8 ± 2.3
16	12.9 ± 2.5
24	13.7 ± 2.8

[a] Average ± standard deviation of pooled data from two independent experiments.

What this data does not indicate, however, is that sintering colloidal templates for extended periods of time caused melting defects over large surface areas of the resulting scaffolds. Figure 2-9 showcases the wide variation of scaffold quality when using a template sintered for 24 h: the left-hand image is nearly perfect, while the right-hand one has large gaps and some large areas of fused polymer.

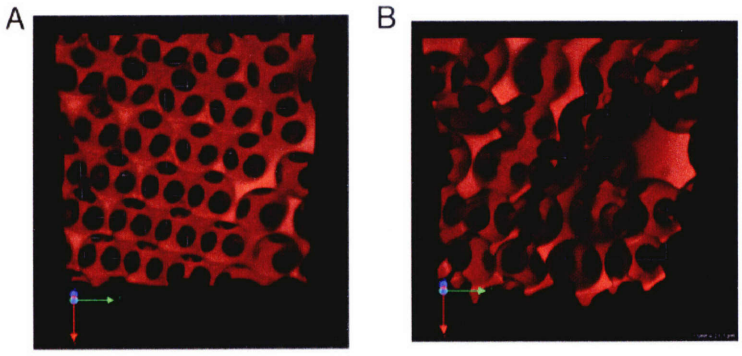

Figure 2-9 **Morphology of defect-free and damaged areas of scaffolds made from sintered templates.** (A-B) Both scaffolds were made from templates sintered for 24 h. (A) An almost defect-free area shows thin struts and large pores. (B) A highly damaged area shows large gaps as well as large areas of non-porous polymer.

In conclusion, although throat pore size in the un-damaged portions of scaffolds increased with sintering time, sintering is not a viable option for significantly altering scaffold architecture at this length scale only, without having undesirable effects on the regularity of the structure.

2.4 Discussion

We developed a novel method of fabricating porous hydrogel scaffolds that has several distinct advantages over most other methods of creating porosity to date. Previous methods of using porogens to create voids in a polymer matrix prior to dissolution of the porogen have been stochastic in nature, prepared by simple mixing of the particle (e.g., sodium chloride salt) and the polymer, or casting of the polymer onto a randomly arranged particle template (82-84). Even in recently developed 'salt fusion' methods, the particle template becomes connected but is not ordered in a crystalline fashion, which creates an inconsistent porosity that may be difficult to

predict (85). Such random mixing processes requires a high porogen fraction, and ultimately a high porosity in the structure (>95%) to achieve the high pore interconnectivity that is so crucial for nutrient diffusion and cell spreading. By creating an ordered crystal of particles – in our case, PMMA microspheres – and then infusing it with liquid, we were able to achieve high pore interconnectivity at ~ 65% porosity (74% theoretical).

The method of colloidal crystal templating, newly applied here to scaffolds appropriate for tissue engineering, may be used with any material that undergoes a permanent transition from liquid to solid (or semi-solid gel). Thus, we developed protocols for two very different common biomaterials: synthetic PEG, and the natural biopolymer gelatin. The PEG gels were solidified using photopolymerization chemistry, while gelatin was cooled from a hot solution and subsequently lyophilized and cross-linked by carbodiimide chemistry.

Microscopic examination of both types of gels showed similar structures: hexagonally close-packed, interconnected pores in three dimensions. However, PEG and gelatin scaffolds differed in several ways. The interconnecting throat pores in PEG scaffolds were ~ 25% of the main void diameter, while for gelatin this value was increased to 40%. This implies that the gelatin was not able to coat the microspheres as well as PEG was, which is supported by the fact that we needed to pre-wet templates with ethanol in order to improve penetration by gelatin. Further, gelatin scaffolds sometimes had a thick layer of bulk gel on the top face due to incomplete infusion, as ascertained by SEM (data not shown). The walls of the gelatin scaffolds also appeared to be thinner than those of the PEG scaffolds. This was likely due to the fact that, although gelatin was used at the same weight concentration as PEG, cross-linking efficiency for gelatin tends to be low and the final material is not expected to be as mechanically robust. In fact, for the 50-100 kDa gelatin used here, the average molecular weight between cross-links would be expected to be at least 2-4 times greater than that for PEGDMA (151).

Despite the slight expected difference in porosity for PEG versus gelatin scaffolds due to the throat pore and wall thickness disparities, mechanical properties testing of PEG and gelatin scaffolds indicated a similar overall porosity as compared to the bulk gels of each substance. The compressive modulus of solid PEG gel, at 160 ± 53 kPa, was four-fold higher than that of solid gelatin, at 37.5 ± 13.7 kPa. However, in both instances the compressive modulus of the porous scaffold was ten-fold lower than that of the bulk gel, at ~19 and ~ 4 kPa, respectively, in good agreement with Gibson-Ashby theory and our empirical determination of porosity. For comparison, scaffolds with 95% porosity would be expected to have moduli of 0.4 and 0.01 kPa.

Finally, we determined for the case of PEG gels whether it was feasible to independently vary porosity on multiple length scales. Some groups that use particulate leaching methods have improved the interconnectivity of their structures by fusing the particle template together (85, 128). Although our structures are already well interconnected, we used a similar strategy to attempt to change the throat pore size while leaving the main void size constant, by sintering PMMA microsphere templates at temperatures near the glass transition temperature of PMMA. We found that sintering did increase the size of the throat pores, by up to 34%. However, the increased pore size was associated with an increase in large melting defects that left large holes in the scaffold structure. This may be due to the change in polymer flow mechanisms that occurs at the transition when air becomes the dispersed phase rather than the continuous phase in the melting sphere template. Narkis has reported that this transition (and its attendant increase in template defects) occurs when the average radius of the necks between two spheres exceeds 30% of the particle radii (150). For our system, this occurs at a neck diameter of 12 μm for a 40 μm particle template. Since the throat pores are likely to be approximately the size of the polymer

necks, we cannot increase the throat pores to be much greater than 12 μm without incurring large defects, in agreement with our data described in section 2.3.5.

Two other groups concurrently developed tissue engineering scaffolds based on colloidal crystal templating similar to the ones we describe here (152, 153). Kotov used very slow (multi-day) evaporation at elevated temperatures to achieve colloidal crystals that could be infused with a biocompatible silica (152), and demonstrated by modeling that the diffusion of nutrients into these scaffolds is ~1/2 as fast as in free solution (154). Another group has since made porous scaffolds specifically from peptide-PEG gels, using a combination of gas-foaming and photopolymerization (155). Foaming processes result in structures with a disordered porosity and a wide distribution of pore sizes. Such structures are thus likely to be mechanically weak relative to ones made by colloidal crystal templating. Further, the more direct (rather than empirical) control over pore size in a templating approach may sometimes be desired.

We believe that the scaffolds we developed can be useful for soft tissue engineering applications where moderate mechanical strength and a high nutrient amount are required. In particular, we are interested in studying T cells in an artificial lymphoid-like environment, as the macroporous nature of the gel scaffold we have described here is well suited to mimic the lymph node T zone ECM.

3 Factors influencing T cell motility: adhesion proteins and chemokines

3.1 Introduction

Concurrently with initial studies of immune cells in our scaffold structures, we pursued simplified systematic methods to determine some basic parameters that could be used to influence T cell migration within the scaffolds. It is known that T cells isolated from murine secondary lymphoid organs or human peripheral blood are largely rounded and non-motile, even if cultured in contact with some adhesive substrates (39, 156-158). However, time-lapse fluorescence imaging of intact murine lymph nodes has revealed that T cells exhibit dramatic, sustained motility during homeostasis and during some phases of antigen (Ag) priming, which may be critical for efficient Ag surveillance ((10, 116, 159), reviewed in (39, 160)). Thus, the polarized, migrating phenotype of naïve lymphocytes *in vivo* is likely supported by signals present in the tissues. Along with the architecture and cellular composition, one notable feature of the lymph node microenvironment is the constitutive presence of high levels of the so-called homeostatic or lymphoid chemokines.

Homeostatic chemokines include CCL21, CCL19, and CXCL12 in the T cell areas of secondary lymphoid organs. These soluble small molecules act as biological signaling agents that may induce cell chemotaxis (migration induced by a gradient of the chemotactic factor) and/or chemokinesis (increase in cell velocity induced in uniform concentrations of the chemokine). During T cell transit across high endothelial cells (from blood to lymph nodes), pronounced chemokine concentration gradients might be encountered, and chemotaxis is likely the predominant mechanism at play. In contrast, the rapid, apparently randomly-directed migration of T cells observed *in vivo* (39, 159-161) could be the result of short-range direction and redirection in response to very localized chemokine gradients within the T cell zone (162), or alternatively, could represent a chemokinetic response to near-uniform levels of chemokine in the tissue. Using *in vitro* culture systems, Kaiser et al. recently reported that CCL19 secreted by mature dendritic cells (DCs) stimulated pronounced motility in co-cultured human naïve T cells; addition of soluble CCL19 at uniform concentrations to naïve T cells cultured on immature DCs (which do not produce CCL19) elicited a similar induction of random motility (158). In light of the evidence, we hypothesized that chemokinesis triggered by homeostatic chemokines could be a general mechanism supporting steady-state lymphocyte motility within secondary lymphoid organs. If true, chemokines could be directly used within artificial lymphoid tissue constructs without need to somehow present the chemokine in gradient form.

We began by determining if naïve T cells could be made to undergo chemokinesis by minimal signals in a 2D environment. Notably, in the first studies examining the effects of homeostatic chemokines on lymphocyte migration, chemokinesis was not observed (e.g., refs (21, 163, 164)). However, these *in vitro* studies utilized modified Boyden chamber assays, in which cells migrate across a thin porous membrane in response to chemoattractant; the type of migration elicited is assessed by introducing chemokine either to the culture chamber opposite the cells (to assay chemotaxis) or at equal concentrations on both sides of the membrane (for chemokinesis). The use of such 'checkerboard' filterplate assays to detect and distinguish

between types of migration can be problematic (165), and in some cases factors that appeared to be only chemotactic in such assays have shown clear chemokinetic effects when more direct assays of cell migration were employed (166).

We thus used direct videomicroscopic observation to test whether the most abundant chemokine in the T cell areas of lymph nodes and spleen, CCL21, could trigger chemokinesis in resting murine T lymphocytes. We found that this was the case, and that the strength of chemokinesis was influenced by the adhesive substrate presented to the cells. Further, using *in vitro* assays designed to model the relative infrequency of Ag-specific T cell—Ag-bearing DC encounters that occur during primary immune responses, we found that treatment of T-DC co-cultures with CCL21 led to an early increase in CD69 upregulation kinetics and a two-fold enhancement in the number of Ag-specific T cells recovered after 4 days. These results provide a possible explanation for the lack of naïve murine lymphocyte motility in purified cultures relative to their behavior in lymphoid organs, and suggest that the high levels of chemokines present in secondary lymphoid organs do not require concentration gradients to have a significant impact on lymphocyte migration. This foundational work paved the way for our studies of T cell behavior in 3D scaffolds, described in Chapter 4.

3.2 Materials and Methods

3.2.1 Cell isolation

All animal work was approved by the MIT Committee on Animal Care, in accordance with federal, state, and local regulations. C57Bl/6 and OT-II mice were obtained from Jackson Laboratory, as were Bl/6 transgenic mice expressing enhanced green fluorescent protein in all cells (GFP Bl/6 mice). DC were derived from the bone marrow of C57Bl/6 mice after Inaba's procedure, cultured with 5 ng/mL GM-CSF (R&D Systems), and used on day 7 (167). $CD4^+$ T cells were isolated from spleens or lymph nodes of 6-12 wk-old mice by MACS negative selection (Miltenyi Biotec $CD4^+$ T cell isolation kit), yielding > 90% $CD4^+$ cells, > 60% $CD62L^{hi}CD44^{low}$ naïve T cells. For some experiments, cells were further purified: $CD4^+$ T cells were separated into $CD62L^+$ and $CD62L^-$ fractions by MACS positive selection (Miltenyi $CD4^+CD62L^+$ T cell isolation kit), or were sorted into $CD62L^+CD44^{lo}$ and $CD62L^+CD44^{hi}$ populations on a FACSAria (BD Biosciences). Cells were cultured in RPMI 1640 medium supplemented with 10% fetal calf serum (FCS), 10 mM HEPES, 100 U/mL penicillin, 100 μg/mL streptomycin, 2 mM L-glutamine, and 50 μM 2-mercaptoethanol.

3.2.2 Cell treatments

Cells were incubated with 1-10,000 ng/mL recombinant mouse CCL19 or CCL21 (R&D Systems) for 20 min prior to initiation of imaging to allow the chemokine to take full effect. Phorbol-12-myristate-13-acetate (PMA) ester treatment (Sigma Aldrich) was performed at 50 ng/mL, with imaging likewise initiated at 20 min. For LFA-1 blocking studies, anti-LFA-1 clone M17/4 or isotype control antibody was used. All antibodies were from BD Pharmingen and used at 10 μg/mL. In videomicroscopy studies utilizing pertussis toxin (PTX), cells were treated with 100 ng/mL PTX or PTX B oligomer (Sigma) for 10 min at 37 °C, washed twice with warm medium, and rested for 90-120 min before use. In co-culture studies, both a high dose (100 ng/mL), and a low dose (2 ng/mL) of PTX were tested; results followed the same trends for both doses. For chemokine removal experiments, cells were washed in 10 mL warm medium,

incubated for 1 h in 2 mL fresh medium under light shaking (< 200 rpm), and washed twice more before imaging.

3.2.3 Videomicroscopy tracking of T cell polarization and chemokinesis.

Eight-well chambered coverslips (Lab-Tek, Nalge Nunc) were incubated with 5 μg/cm^2 of fibronectin (FN) for 2 hours at 21 °C, or 10 μg/mL recombinant ICAM-1/Fc or VCAM-1/Fc fusion proteins (R&D systems) overnight at 4 °C, prior to addition of cells (2-3x10^6) and chemokine. A fraction of CD4$^+$ T cells from C57Bl/6 mouse spleens (~20 %, for ease of automated tracking) were labeled with 2.5 μM Fura 2-AM (Molecular Probes) for 25 minutes at 37 °C. Similarly, splenic CD4$^+$ T cells from GFP mice used for chemokine response longevity studies were diluted to 20% with C57BL/6 CD4$^+$ T cells. Fura (for C57Bl/6 mice, exc 380 nm, em 510 nm) or green (for GFP mice, exc 488 nm, em 510 nm) fluorescence and bright-field images were acquired at 30 s intervals for 40 min on a Zeiss Axiovert 200 3D epifluorescence microscope equipped with environmental stage (37 °C, 5% CO_2) with the aid of Metamorph software (Universal Imaging, Inc.).

3.2.4 Image Analysis

Cell polarization and migration were analyzed with the aid of Metamorph and Volocity (Improvision, Inc.) software packages. Data were sharpened with the no-neighbors 2D deconvolution algorithm in Metamorph to facilitate cell tracking using Volocity. For each field, 26-44 cells were analyzed (depending on fluorescent cell density) based on intensity thresholding and size exclusion (to rid a small fraction of large cell contaminants); the dead cell population that developed during longevity experiments was excluded from analysis. A cell was scored as polarized at a single time-point if its shape factor (4π area/perimeter^2) did not exceed 0.85. To score average population behaviors, polarized cells were defined as those with a shape factor $\leq$ 0.85 in $\geq$ 15% of observed time-points. Migrating cells were defined as polarizing cells with time-averaged velocities $\geq$ 4 μm/min.

3.2.5 T-DC co-cultures

All experiments were performed in 96-well round-bottom plates (BD Falcon). To assay CD69 upregulation, duplicate samples of 2x10^5 total cells were prepared at an overall T:DC ratio of 1:1. A portion of day-6 DC were matured with lipopolysacharride (LPS, 1 μg/mL, Sigma) and pulsed with OVA peptide (ISQAVHAAHAEINEAGR, 500 nM, AnaSpec Corporate) for 16 h, while others were left untouched; mixtures of peptide-loaded (and washed) mature DC (OVA-mDC) and immature DC (iDC) were then prepared at a 1:20 ratio. OT-II CD4$^+$ T cells were also diluted 1:9 with C57Bl/6 CD4$^+$ T cells. T cells (with or without PTX pre-treatment) and DC mixtures were aliquotted in FN-treated wells, briefly centrifuged (1200 rpm, 1-2 min), then placed in culture in the presence or absence of 1 μg/mL CCL21, which was replenished at 48 h. CD69 upregulation was analyzed at times ranging from 24-96 h: duplicate samples were pooled, cells were stained with anti-CD69-FITC, anti-Vα2-PE, and anti-CD4-biotin followed by streptavidin-APC, and finally propidium iodide.

The effect of CCL21 on T cell proliferation was assessed by a CFSE dilution assay, using a similar co-culture system: OT-II T cells were labeled with 10 μM CFSE for 10 min and washed 3X prior to mixing with C57Bl/6 CD4$^+$ T cells at a 1:9 ratio. Triplicate co-cultures of 5x10^5 total cells were prepared at an overall T:DC ratio of 9:1 and an iDC:OVA-mDC ratio of 1:1; 1 μg/mL

CCL21 was added at time zero to CCL21-treated cultures. Proliferation in each well was assayed on day 4 by flow cytometry analysis of cultures stained with anti-Vα2-PE, anti-Vβ5-biotin (then streptavidin-APC), and propidium iodide. All data was collected on a Becton-Dickinson FACSCalibur using CellQuest software and analyzed with FlowJo software, using antibodies from Pharmingen.

3.2.6 T cell viability studies

T cells ($2x10^5$ in 200 μL per well) were labeled with CFSE as described above, incubated with or without 1 μg/mL CCL21 for 24 h, then stained with propidium iodide and analyzed by flow cytometry. Equal volumes were run from each sample, in order to determine both the percentage of live cells in the sample, and the absolute number of live cells in the sample.

3.2.7 DC phenotypic analysis

DCs (~$1x10^6$ in 1 mL per well) were left untreated or incubated with 1 μg/mL CCL21 and/or 1 μg/mL LPS on day 6. The next day, the following antibodies were used for staining (all at 10 μg/mL unless otherwise noted): CD16/32 blocking antibody, CD80-FITC, I-A^b–PE (2 μg/mL), and CD11c-biotin followed by streptavidin-APC and propidium iodide (1.25 μg/mL). Equal numbers of cells were analyzed per sample.

3.3 *Results*

3.3.1 CCL21 and CCL19 induce chemokinesis in resting CD4⁺ T cells exposed to an adhesive substrate

Many chemokines, including CCL19 and CCL21, are known to trigger polarization in resting T cells at uniform concentrations (168, 169). We confirmed that both CCL21 (Figure 3-1, A and B) and CCL19 (data not shown) elicited pronounced polarization of ~ 75% of freshly isolated murine (C57Bl/6 strain) $CD4^+$ T cells within 5 min, whereas the majority of untreated resting cells were round. In experiments where $CD62L^+CD44^{lo}$, $CD62L^+CD44^{hi}$, and $CD62L^-$ CD4 T cells were separated, all populations responded nearly equally to CCL21 (data not shown). When T cells were seeded on bare glass with soluble CCL21 and tracked by videomicroscopy, we observed not only rapid cell polarization, but also that a small fraction of cells (~3%) appeared to actively migrate (Figure 3-1B). Because polarization and adhesion are two prerequisites for T cell motility (156, 170), and CCL21 is known to induce adhesion to integrin ligands (111, 171), we tested whether motility would follow polarization if the cells were exposed to a suitable adhesive substrate.

$CD4^+$ T cells were seeded at relatively high densities (crudely mimicking the dense cellularity of SLO) on glass substrates coated with recombinant ICAM-1, with or without chemokine. T cells had low basal adhesion and motility when seeded on ICAM-1-coated substrates in the absence of chemokine; most cells moved only by convective drift and collisions with neighboring cells (Figure 3-1B, and data not shown). In contrast, addition of CCL21

stimulated migration in 60 ± 5 % of T cells (Figure 3-1B). As illustrated by single-cell migration paths (Figure 3-1C), CCL21-treated cells migrated substantial distances on ICAM-1 with no preferred direction, while the majority of cells remained relatively stationary in the absence of chemokine or slowly convected. Convecting vs. migrating cells were readily distinguished via single cell velocity time-courses (Figure 3-1D) and histograms of instantaneous velocities (Figure 3-1E); migrating T cells had peak speeds of up to 20 μm/min, while control cells had smoother velocity profiles with speeds rarely exceeding 10 μm/min. The time-averaged velocity of single cells exposed to CCL21 on ICAM-1-coated surfaces ($\langle v \rangle = 5.16 \pm 2.08$ μm/min) was likewise significantly higher ($p \leq 0.0001$) than that observed for cells on ICAM-1 with no chemokine (Figure 3-1F).

Importantly, chemokinetic migration was dependent on the presence of both chemokine and adhesive ligand: when the T cell integrin LFA-1 was blocked with an antibody, T cells on ICAM-1 substrates polarized, but failed to migrate (Figure 3-1G); isotype control antibody had no effect (data not shown). Treatment of T cells with pertussis toxin (PTX), which inhibits G-protein-coupled receptor signaling, reduced both polarization and migration ($p \leq 0.05$), whereas the PTX B oligomer (control) had no effect (Figure 3-1G). Blocking LFA-1-ICAM-1 interactions with an anti-LFA-1 antibody or treating the cells with PTX significantly reduced average cell velocities as well (Figure 3-1F). We tested whether the observed migration was a result primarily of increased adhesion to ICAM-1 rather than chemokinesis *per se*, by treating cells with the phorbol ester PMA, which increases T cell adhesion to ICAM-1 (172). PMA triggered polarization in a majority of cells, but did not induce migration on ICAM-1 (Figure 3-1G). Thus, CCL21 elicits chemokinesis from $CD4^+$ T cells, with migration dependent upon G-protein coupled receptor signaling and exposure to an adhesive substrate such as ICAM-1.

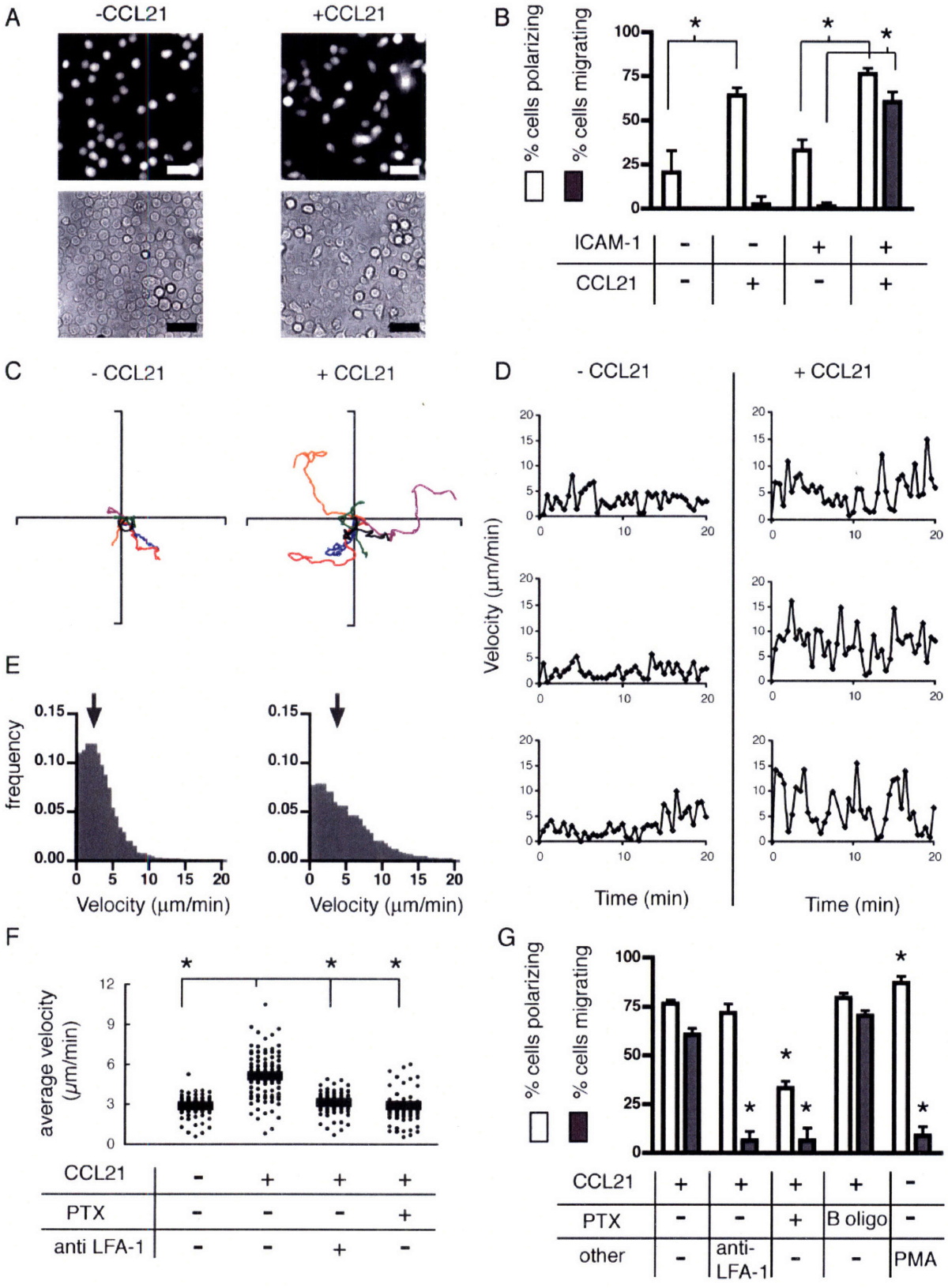
A
-CCL21
+CCL21
B
% cells polarizing
% cells migrating
100
75
50
25
0
*
*
*
ICAM-1 - - + +
CCL21 - + - +
C
- CCL21
+ CCL21
D
- CCL21
+ CCL21
Velocity (μm/min)
Time (min)
Time (min)
E
frequency
0.15
0.10
0.05
0.00
0 5 10 15 20
Velocity (μm/min)
Velocity (μm/min)
F
average velocity (μm/min)
12
9
6
3
0
*
*
*
CCL21 - + + +
PTX - - - +
anti LFA-1 - - + -
G
% cells polarizing
% cells migrating
100
75
50
25
0
CCL21 + + + + -
PTX - - + B oligo -
other - anti-LFA-1 - - PMA

Figure 3-1 **CCL21 synergizes with ICAM-1 to promote chemokinesis of freshly-isolated CD4$^+$ T cells.** (A) Fluorescence (top) and brightfield (bottom) images of C57Bl/6 CD4$^+$ T cells before (left) and 20 min after (right) addition of 1 μg/mL CCL21. A fraction of cells (20%) were labeled with Fura 2-AM for software-assisted tracking. Scale bars 20 μm. (B) Percent T cells polarizing and migrating on bare or ICAM-1-coated surfaces, with or without CCL21 addition. Ave. ± std. dev. shown for 3 independent experiments per condition. [* indicates bracketed conditions are statistically different ($p \leq 0.05$)] (C) 2D migration paths for 6 representative control (left) and CCL21-stimulated (right) cells over 20 min are shown; all axes 90 μm. (D) Single cell velocity time-courses for 3 of the individual control (left) and CCL21-stimulated (right) cell tracks shown in (C). (E) Instantaneous velocity distributions on ICAM-1-coated surfaces without (left) or with (right) CCL21 are shown ($n > 75$ cells each). (F) Time-averaged single-cell velocities on ICAM-1 surfaces with or without CCL21 addition and other treatments as shown; bars indicate the population average velocity. [* indicates conditions statistically different ($p \leq 0.0001$) from +CCL21 sample.] (G) Percent T cells polarizing and migrating on ICAM-1 coated surfaces after indicated treatments shown for 3 independent experiments per condition. [* indicates statistically different ($p \leq 0.05$) from +CCL21 only case.]

3.3.2 Chemokinesis occurs at physiological CCL21 doses and supports long-lived cell migration

Naïve T cells are estimated to spend 12-18 h in a single lymph node during their homeostatic recirculation between blood and secondary lymphoid tissues (162). In order for chemokinesis triggered by CCL21 to be relevant to T cells' search for antigen in lymph nodes, the migratory response would need to be sustained throughout a similar time period in response to chemokine doses present in the intact tissues. The concentration of CCL21 in secondary lymphoid organs has been estimated at ~2 and ~10 μg/mL by ELISA and Western blotting of tissue supernatants, respectively (25, 36, 38). Using videomicroscopy, we found an onset of T cell motility induced by 10-100 ng/mL CCL21, whereas the percentage of cells polarizing and migrating began to plateau between 100-1000 ng/mL (Figure 3-2A). (However, the average time that any particular cell spent polarized and the average single-cell velocity continued to increase up to at least 10 μg/mL – data not shown). Notably, the onset and plateau response in chemokinetic migration measured here parallels the dose response reported for chemotactic migration triggered by murine CCL21 (21).

To assess the longevity of the observed chemokinetic response, T cells seeded on ICAM-1 surfaces were tracked by videomicroscopy 20 min after addition of CCL21, and again 24 h later. Live T cell migration in response to CCL21 did not appear to weaken at all over 1 day (Figure 3-2B-D), whereas only minor basal motility (< 20 %) developed in samples not treated with CCL21 (Figure 3-2B). When we attempted to wash out the chemokine 24 h after addition (or 1 h; not shown), cell polarization was significantly reduced ($p \leq 0.0001$, Figure 3-2C). Thus, CCL21-driven responses are sustained at physiological concentrations over time periods consistent with lymphocyte residence in a given lymph node, and appear to be dependent on the persistent presence of chemokine.

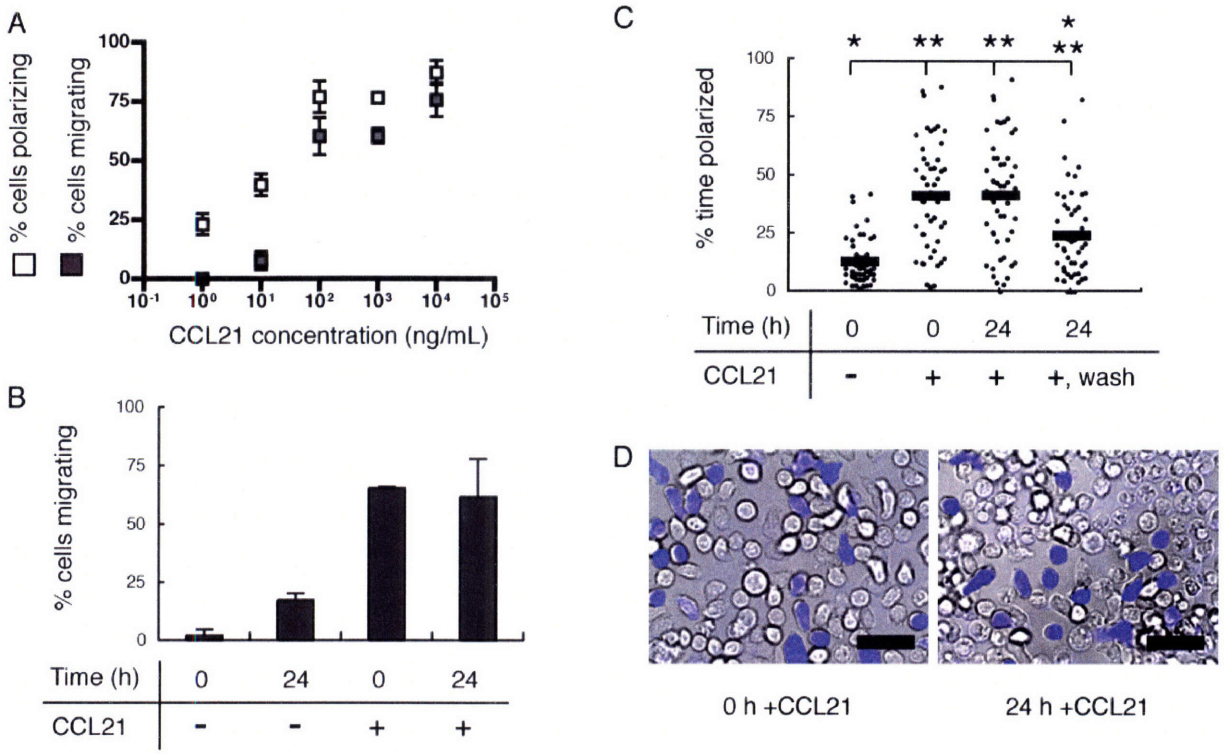

Figure 3-2 **Polarization and migration responses of CD4⁺ T cells triggered by CCL21 are sustained for at least 24 h in the presence of chemokine.** (A) Average percent cells polarizing and migrating at given doses of CCL21. (B) Average percent cells migrating at 0 and 24 h in the presence or absence of chemokine (error bars represent range). (C) Percent time polarized for individual cells from two pooled longevity and chemokine removal experiments: cells were observed at 0 h both before and after chemokine addition, 24 h later, and finally after washing. Horizontal bars denote pop. aves. [* and ** indicate conditions statistically different from +CCL21 ($p \leq 0.0001$) or control ($p \leq 0.001$) samples, respectively.] (D) For a sample treated with 1 μg/mL CCL21 at 0 h (left), many polarized cells remain at 24 h (right). Labeled cells (Fura 2-AM) shown in false color. Scale bars 20 μm.

3.3.3 CCL21 triggers chemokinesis on several adhesion ligands present in secondary lymphoid tissues

To determine whether CCL21 could synergize with other adhesion ligands present within T cells areas of secondary lymphoid organs to promote T cell migration, we observed CD4⁺ T cell motility on VCAM-1 and fibronectin (FN)-coated substrates for comparison to the response observed on ICAM-1 surfaces. T cell polarization induced by CCL21 was statistically identical on bare glass or in the presence of each adhesion ligand (Figure 3-3A). For all 4 surfaces, the population time-averaged velocity was increased in the presence of CCL21 (Figure 3-3B). (This was true even on bare glass where cells were non-adherent, due to increased convection caused by CCL21-induced polarization.) However, the CCL21-induced increase in mean velocity of T

cells was significantly greater for cells cultured on ICAM-1, VCAM-1, and FN compared to bare glass, suggesting that CCL21 can synergize with multiple adhesion ligands to promote T cell migration (Figure 3-3B, $p \leq 0.05$). The exact velocity profiles of both chemokine-treated and untreated cells depended on the surface (Figure 3-3C); this is to be expected, as cell migration rates are controlled by adhesion strength – which likely differs for each ligand at the single surface-coating densities tested here – as well as potential qualitative differences in the adhesion receptors involved (173). However, the responses measured here clearly indicate that chemokinesis induced by CCL21 in concert with an adhesive substrate is not limited to synergy with ICAM-1 alone.

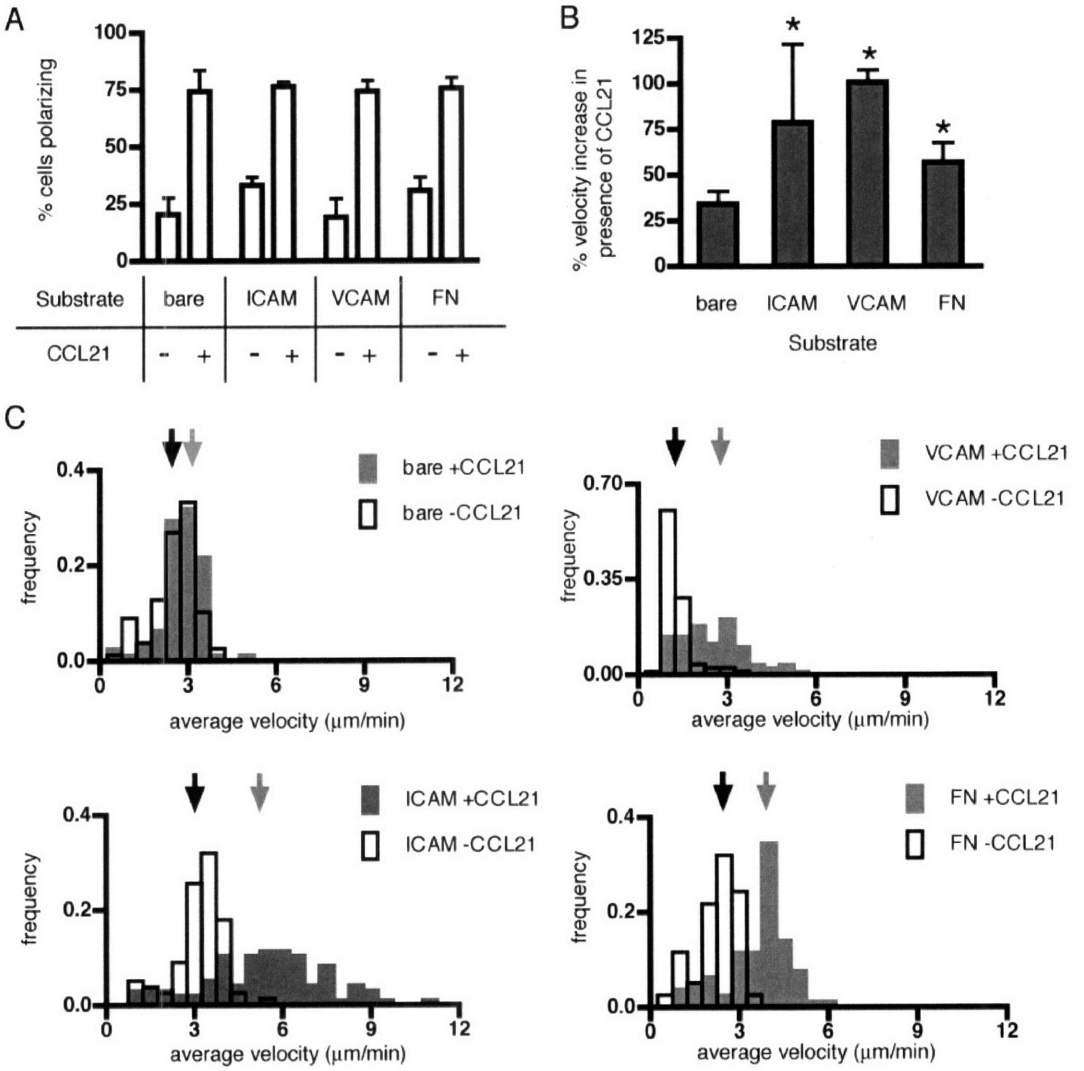

Figure 3-3 **CCL21 synergizes with several adhesion ligands present in secondary lymphoid tissues to promote random T cell motility.** (A) Percent $CD4^+$ T cells polarizing on bare glass, ICAM-1-, VCAM-1-, or FN-coated substrates with/without CCL21 (B) For each substrate, percent increase in average cell velocity with chemokine treatment (vs. untreated sample) is shown. [* indicates statistically different ($p \leq 0.05$) from bare glass case.] (A-B) show ave. ± std. dev for 3 independent experiments. (C) Histograms of time-averaged single cell velocities for

control and CCL21-stimulated cells on ICAM-1, VCAM-1, FN, and bare glass shown for 3 pooled experiments per condition ($n > 75$ cells each); arrows indicate population median velocity. CCL21 was used at 1 μg/mL for all experiments.

3.3.4 CCL21 impacts CD4$^+$ T cell priming under conditions of rare antigen specific T cell-DC encounters

To determine whether CCL21 could impact naïve T cell priming under conditions modeling the rarity of Ag-specific encounters *in vivo*, we prepared T cell-DC co-cultures where both Ag-specific T cells and peptide-bearing DCs were present at high dilution. We first assayed T cell activation kinetics via CD69 upregulation, reasoning that chemokinesis triggered by CCL21 might alter the rate of early priming events. Peptide-loaded mature bone marrow-derived DCs (OVA-mDC) were mixed with immature peptide-free DCs (iDC) at a ratio of 1:20 and plated in FN-coated round-bottom culture wells. A mixture of OVA peptide-specific transgenic CD4$^+$ T cells (OT-II (174)) and CD4$^+$ T cells from wild-type (C57Bl/6) mice (at a 1:9 ratio) was then added for an overall 1:1 T:DC ratio. Wells received CCL21 (1 μg/mL) at both 0 and 48 h or were left untreated, and CD69 upregulation was assessed as a function of time on equal numbers of live Ag-specific cells (identified as CD4$^+$Vα2$^+$PI^{lo} cells, a gating which included some wild-type cells, Figure 3-4A). As shown for a representative experiment in Figure 3-4B, the fraction of CD69^{hi} Vα2$^+$ cells was higher for CCL21-treated samples than for untreated controls at all time-points, by up to 1.5-fold at 48 h.

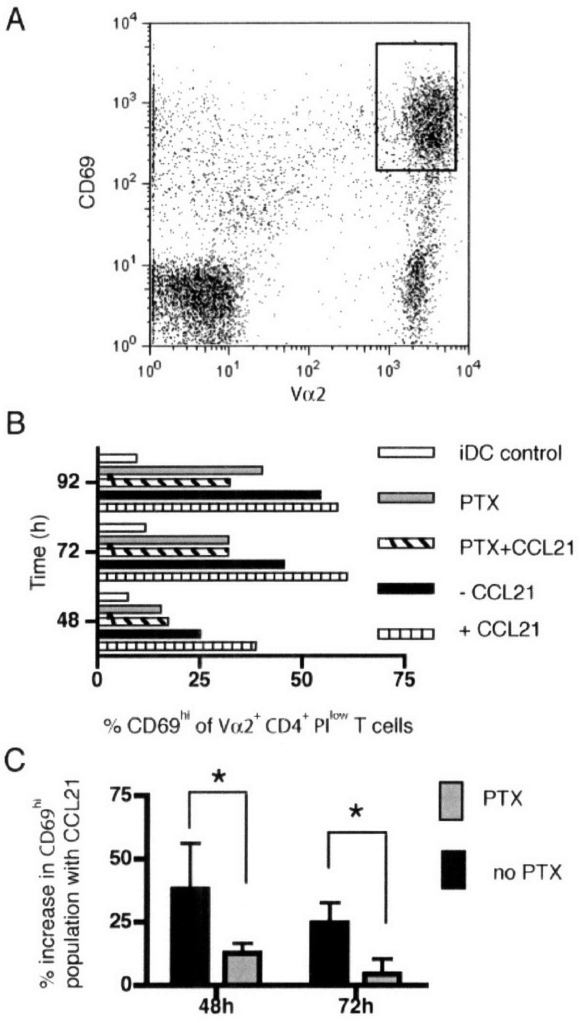

Figure 3-4 **CCL21 impacts kinetics of naïve T cell priming under conditions of rare Ag-specific T cell-rare Ag-bearing DC encounters.** (A-C) Co-cultures comprising 5% OVA-specific OT-II $CD4^+$ T cells, 45% C57Bl/6 $CD4^+$ T cells, 2.5% OVA-pulsed mature bone marrow-derived DC (OVA-mDC) and 47.5% immature DC (iDC) with/without CCL21 were analyzed by flow cytometry at the indicated times. (A) $V\alpha2^+CD69^{hi}$ cells from the $CD4^+PI^{lo}$ population were identified as shown by the rectangular gate. (B) Percent of $V\alpha2^+$ T cells that were also $CD69^{hi}$ shown over time for control (-CCL21), CCL21-treated (+CCL21), PTX-treated cells and without CCL21, and a control containing 50% T cells and 50% iDC are shown. A and B are data from 1 representative of 3 independent experiments. (C) % increase in $CD69^{hi}$ population for CCL21-treated samples (vs. relevant control), comparing PTX-treated (gray) and untreated (black) samples; data from three independent experiments, pooled. [* indicates bracketed samples statistically different ($p \leq 0.05$).]

To distinguish between effects of CCL21 on T cells and DCs in the co-culture, we also applied a PTX treatment strategy reported by Lo et al. to block G protein-coupled receptor signaling in a selected cell population for at least 26 hrs (175). PTX-treated T cells showed reduced CD69 upregulation compared to untreated T cells in the presence of CCL21, indicating that the primary effect of CCL21 in these co-cultures was mediated by T cells (Figure 3-4). The increase in the $CD69^{hi}$ population elicited by CCL21 was significantly greater for untreated versus PTX-treated co-cultures across multiple experiments ($p \leq 0.05$, Fig. 4C), and was most prominent at 48 hrs.

In order to examine the end-point effects of CCL21 on T cell priming, we performed a CFSE dilution assay to directly observe Ag-specific cell division. For this assay, OT-II T cells were again diluted 1:9 with polyclonal $CD4^+$ T cells, but a more physiological total T:DC ratio of 9:1 was used, and the DC population was equal parts iDC and OVA-mDC. OT-II T cells in the culture were labeled with CFSE to track cell division by flow cytometry. At 85 h, equal volumes of total cells were analyzed and the number of live OT-II cells ($V\alpha2^+V\beta5^+PI^{lo}$) and their CFSE fluorescence distribution were determined. In control co-cultures where all DCs were immature cells lacking antigen, no cell division was observed; in contrast, both PTX-treated and untreated OT-II cells proliferated when OVA-mDC were present (Figure 3-5A and data not shown), with similar cell division profiles irrespective of CCL21 treatment (2.88 ± 0.03 vs. 2.70 ± 0.02 mean divisions per cell in the presence or absence of chemokine, respectively, for the no PTX case).

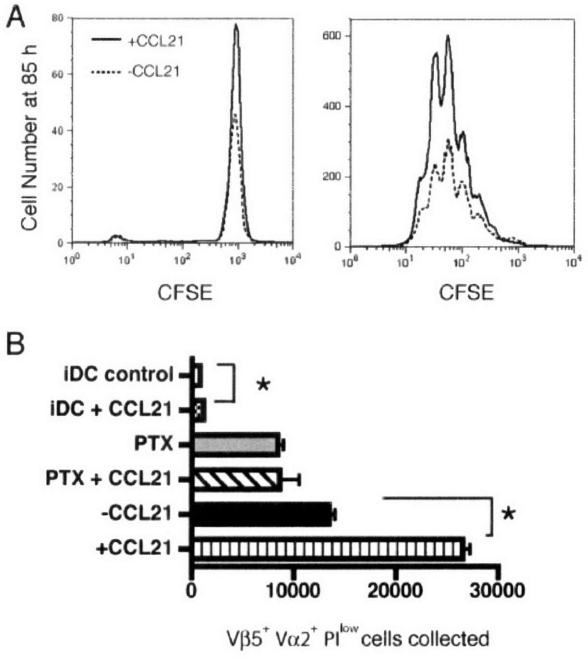

Figure 3-5 **CCL21 impacts naïve T cell proliferation under conditions of rare Ag-specific T-DC encounters.** Co-cultures comprising 9% OVA-specific OT-II CD4+ T cells, 81% C57Bl/6 $CD4^+$ T cells, 5% OVA-mDC and 5% iDC with/without CCL21 were analyzed by flow cytometry at 85 h. (A) Sample CFSE histograms are shown for control (left, iDC only) and experimental (right, with OVA-mDC) conditions. (B) OTII cell recovery for all conditions is shown. Ave ± std. dev. for 3 wells per condition. [* indicates bracketed conditions statistically different ($p \leq 0.05$)] (A-B) are from 1 representative of 5 experiments.

Equal numbers of OT-II cells were recovered from PTX-treated samples regardless of CCL21 treatment (Figure 3-5B). However, in both the presence and absence of OVA-mDC, the addition of CCL21 increased the number of OT-II T cells recovered significantly, by 2.0-fold and 1.4-fold, respectively ($p \leq 0.05$, Figure 3-5B). In comparing multiple similar experiments we found that the fold increase in T cell recovery was consistently greater in the presence of Ag-bearing DCs than in their absence (2.1 ± 0.4-fold in presence of Ag, 1.4 ± 0.1-fold in absence of Ag, $p \leq 0.05$), thus showing an Ag-specific effect.

The enhanced cell recovery in CCL21-treated co-cultures was not due to a direct survival signal delivered to resting T cells by chemokine, as purified T cells cultured alone for 24 h with or without CCL21 were recovered in equal numbers, with an equal percentage of dead cells (as determined by PI staining, see Figure 3-6). Nor did variations in T cell co-stimulation by DCs appear to play a role, which we concluded by observing the levels of the co-stimulation marker CD80 on LPS-matured and untreated DCs exposed to CCL21. As shown in Figure 3-7, there was a shift in CD80 levels observed for DCs treated with LPS, as is expected upon maturation; however, intensity data from CCL21-treated cells with or without concurrent LPS treatment overlap the data for their respective DCs (mature or immature) lacking CCL21 almost exactly.

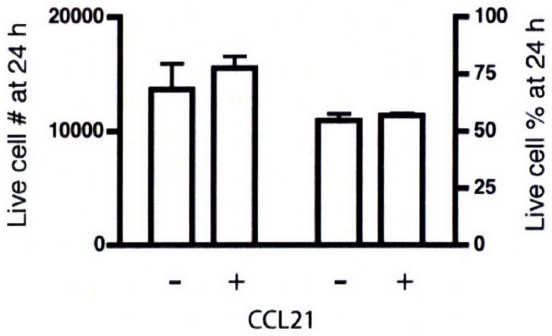

Figure 3-6 **CCL21 does not alter resting T cell viability.** Equal numbers (left) and an equal percentage (right) of live $CD4^+$ resting T cells were recovered from wells treated or not treated with CCL21. No other additives were used.

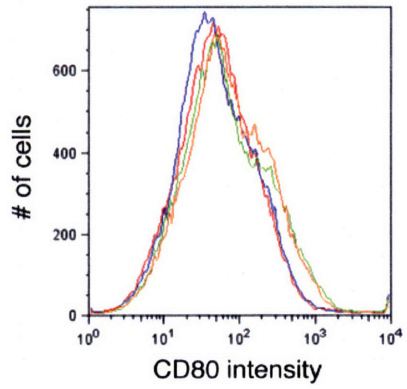

Figure 3-7 **CCL21 does not affect CD80 levels on immature or mature DC.** Flow cytometry analysis was performed on DCs cultured with the following factors: blue line – none, red line – CCL21 only, green line – LPS only, orange line – both LPS and CCL21. Cells were gated on the DC marker CD11c and PI staining was used to exclude dead cells.

Altogether, these results suggest that CCL21 signaling can impact the kinetics of early activation events and the ultimate number of expanded T cells while having a minor impact on the mean number of cell divisions, under conditions where Ag-specific T cells and peptide-bearing DCs are present at low frequency.

3.4 Discussion

Fewer than 1 in 1000 naïve T cells express receptors specific for any given antigen (9, 176), and in order for a primary immune response to occur, these scarce Ag-specific T cells must come into physical contact with rare but strategically-placed DCs (6, 177). Further, during Ag-limited infections or immunizations, only a fraction of DCs may present the relevant antigen to T cells. Recent studies have revealed sphingosine-1 phosphate receptor down-modulation on entry into lymph nodes and slow re-expression during trafficking through the lymphoid tissue as a possible molecular timer influencing naïve T cell residence times in lymph nodes (175). Rapid motility within lymph nodes may thus enable efficient detection of rare antigens prior to default trafficking of Ag-specific cells out of the organ. Here we tested whether chemokinesis could be one regulatory mechanism in secondary lymphoid organs for inducing favorable motility during both T cell priming and homeostatic trafficking.

We first showed, using direct videomicroscopic observation, that the homeostatic chemokine most abundant in T cell areas of secondary lymphoid organs – CCL21 – causes pronounced T cell migration in the absence of specific gradients, and that this response is critically dependent on the presence of appropriate ligands to promote cell adhesion, notably ICAM-1. In secondary lymphoid tissues where CCL21 (and CCL19) is constitutively produced, T cells are exposed to VCAM-1 on stromal cells and DCs (178), ICAM-1 on DCs (179) (and potentially stromal cells (178)), and possibly FN presented by fibroblastic reticular cells or exposed on the surface of a small fraction of reticular fibers not enveloped by reticular cells (2, 7). We found that all three of these ligands could support some degree of cell migration. Highly favorable T cell migration on ICAM-1 may reflect the need for rapid investigation of DC cell bodies. Notably, histological studies reveal that about 60% of T cells in lymph nodes are in contact with DCs at any given moment (177).

In order for chemokinesis to be relevant for T cell migration within secondary lymphoid organs, it should be sustained for the typical cell residence time: 12-18 h in the case of lymph nodes (162). We found that CCL21-induced chemokinesis is indeed sustained for at least 24 h, consistent with the finding in the human system that, in contrast to many chemokine/receptor interactions, CCL21 binding to CCR7 does not trigger receptor downmodulation (180). The residual cell polarization we observed after washing out chemokine may be due to the high-affinity nature of CCL21-CCR7 binding and possible chemokine sequestration by cell surface proteoglycans (110, 181), which complicate full separation of the cells from ligand. Nevertheless, we observed that the long-term chemokinetic response was dependent at least in part on the continued presence of CCL21.

Based on these findings, we sought to examine whether chemokinesis triggered by CCL21 could impact T cell priming, using a culture system designed to model the infrequency of Ag-specific T-DC contacts *in vivo*. We found that addition of CCL21 to T cell-DC co-cultures enhanced the initial kinetics of CD69 upregulation and led to 2-fold greater numbers of Ag-

specific OTII T cells recovered after 4 days. Because activated/expanded T cells are constitutively motile (182-185) we might expect that the presence of CCL21 would only alter the initial number of (otherwise non-motile) naïve T cells that would encounter a DC and begin proliferating. Naïve cells that did make contact with DCs and divide (in the presence or absence of chemokine) would thus proceed at equal rates to begin dividing, assuming equal rates of further cell division and no differences in cell death (we found similar fractions of apoptotic cells in cultures with or without CCL21, data not shown). In agreement with this hypothesis, CCL21-treated T cells had similar cell division profiles as control cells – only the recovery of Ag-specific T cells changed. Surprisingly, we found that addition of CCL21 to peptide-free co-cultures also increased the recovery of OTII cells, though control experiments revealed no evidence for a direct survival signal given to T cells by CCL21. This could be due to CCL21-driven T cell motility increasing Ag-independent T-DC contacts, which promote T cell survival (186, 187). We found that the increase in T cell recovery was consistently greater in the presence of Ag-bearing DCs than in their absence, suggesting an Ag-specific effect apart from survival cues imparted to T cells by immature DCs. However, we also cannot rule out the possibility that the viability of T cells is enhanced by CCL21 once they are activated.

These results suggested an influence of T cell chemokinesis on priming but were not definitive, since the receptor for CCL21, CCR7, is expressed by both naïve T cells and mature DCs (188), and CCR7 signaling is known to promote DC motility (189), dendrite extension (190), and enhance LPS-driven maturation (191). However, flow cytometry analysis of our LPS-matured DCs exposed to the prokaryotic-derived CCL21 used here showed no evidence of further maturation, nor were immature DCs matured by CCL21. More importantly, selective PTX-treatment of T cells alone largely abrogated the positive effects of CCL21 (Figure 3-4B and D, Figure 3-5B), suggesting that chemokine receptor signaling in T cells was responsible for the accelerated CD69 upregulation and enhanced proliferation of Ag-specific cells in our co-culture system. Notably, CD69 upregulation and proliferation of PTX-treated cells were slightly lower than for untreated T cells even in the absence of exogenously added CCL21, perhaps reflecting a contribution of other chemokine signals to the T cell response- e.g., CCL19, which is produced by mature DCs (192), and which has recently been shown by Kaiser et al. to promote T cell scanning of DCs (158).

Altogether, these findings suggest that the rapid migration of lymphocytes observed within the parenchyma of secondary lymphoid organs could be supported by chemokine signaling in the absence of significant concentration gradients. Recent analyses of T cell migration within intact SLO have so far failed to reveal evidence for chemotaxis during homeostatic lymphocyte trafficking once T and B cells reach their respective zones, which may reflect a truly random program for T cell scanning or the action of very local attraction gradients near antigen-presenting cells such as DCs (39, 116, 159). In either case, the data shown in this chapter suggest that homeostatic chemokines could function not only to direct lymphocytes to their respective compartments, but also to regulate the random motility of these cells in lymphoid organs observed during their constitutive surveillance for antigen. This knowledge can be applied to artificial immune constructs by modifying them to incorporate CCL21.

4 Providing a cell-supportive microenvironment in inverse opal scaffolds for lymphoid tissue engineering

4.1 Introduction

The goal of many immunotherapies is to trigger *de novo* immune responses or amplify existing responses (57). Immunotherapies are particularly attractive for cancer treatment: many tumors display weakly immunogenic antigens that stimulate a partial adaptive immune response, and the quantity (and type) of the resulting immune cell infiltrate correlates with increased survival in many cancers (41, 43). Thus, one strategy to activate or enhance immunity is to provide cues that drive the accumulation of adaptive immune cells at a tumor or infection site. Dendritic cells (DCs) capture and present foreign antigens to T cells, driving the latter's differentiation into effectors or memory cells that can eliminate infected or transformed cells. The co-localization of T cells and DCs at a tumor or infection site should therefore facilitate the uptake of antigen and priming of a productive immune response. Attracting immune cells to cancer sites has been achieved by injecting immune cell chemoattractants into tumors (54), antibody targeting of chemoattractant-inducing cytokines to tumors (52), and transfecting tumor cells to express such cytokines or chemokines themselves (53, 55) (see also section 1.2). In addition to attracting immune cells, the chemokine CCL21 is also able to dampen (54, 55) tumor immunosuppressive signals (44). However, to achieve significant effects, chemoattractant signals must be sustained by daily injections.

An alternative might be to use a tissue engineering-based approach, by implanting or injecting a scaffold/matrix to create a defined space for immune cell interactions. As in traditional tissue engineering strategies, this microenvironment could be populated by co-delivering specifically selected (e.g., disease-specific) autologous immune cells (193), recruiting host immune cells *in situ* from the local circulation, or via a combination of these two methodologies. The ability to specifically engineer this microenvironment to support the activation of T cells, localize it to relevant tissue sites (e.g., tumor biopsy sites), and to create depots of supportive chemokines/cytokines might provide important advantages over the strategies described above. Because the specific architecture and cell compartmentalization in secondary lymphoid organs is believed to make immune responses highly efficient (2, 3), a scaffold providing a defined space and supportive signals for lymphoid tissue neogenesis may also be superior to vaccination strategies based on the simple injection of purified disease-specific T cells or dendritic cells.

Notably, many of the cytokines that have been studied for driving site-specific immune cell accumulation play a role in lymphoid organogenesis (33, 38) and can induce local ectopic lymphoid tissue neogenesis ('tertiary' lymphoid tissue) (35, 36). In a murine system, Suematsu et al. used collagen sponges loaded with a cell line expressing the key developmental cytokine lymphotoxin to induce the local generation of lymphoid tissue within the implant, complete with organized T cell and B cell areas (119, 120). This study provides a provocative example of what may be possible with a tissue engineering-based approach; however, the use of transfected cell lines may not be attractive for clinical application due to safety and cost issues. We have thus

pursued suitable scaffolds and cytokine cues that could be combined to drive local immune cell accumulation and/or lymphoid tissue induction without the need for genetically engineered cells.

Scaffolds for such lymphoid tissue engineering should provide a mechanically robust, defined microenvironment for *ex vivo* cell loading and/or *in vivo* cell infiltration, as well as adhesion and motility cues to support cell migration and interactions. As described in Chapter 2, we and others have demonstrated the use of colloidal crystal templating to create macroporous 'inverse opal' hydrogels, which are composed of ordered, interconnected arrays of pores formed on the tens of microns length scale (152, 153, 194). We envisioned this macroporous network as an idealized surrogate for the reticular network in the T cell areas of secondary lymphoid organs, a matrix composed of collagen fibers spaced 5-30 μm apart (2, 3) and coated with basement membrane proteins (5) and cells.

In the present studies, we tested the ability of these inverse opal hydrogels to support the migration of primary T cells and dendritic cells, and explored strategies to provide motility-inducing cues within these structures. Because the frequency of antigen-specific T cells is very low (as few as 1 in 200,000 T cells in primary immune responses (9, 176)), T cell motility must be robust for efficient antigen surveillance. As described in Chapter 3, T cell migration is modulated by the cells' ability to adhere to their surroundings and by the presence of motility-inducing chemokines (170, 195, 196). Thus, we first tested T cell loading and migration within crosslinked poly(ethylene glycol) (PEG) inverse opal scaffolds surface-functionalized with the short adhesion peptide Arg-Gly-Asp-Ser-Pro (RGDSP) (see Figure 4-1A and B). Though RGD peptides supported the attachment and migration of an activated T cell clone through the matrix, we found that most primary T cells adhered poorly to RGD-functionalized gels. This finding may reflect the relatively low level of β1 integrins expressed by T cells (197) and the fact that integrins are known to bind RGD peptides with at least 10-fold lower affinities than complete adhesion proteins such as fibronectin (198).

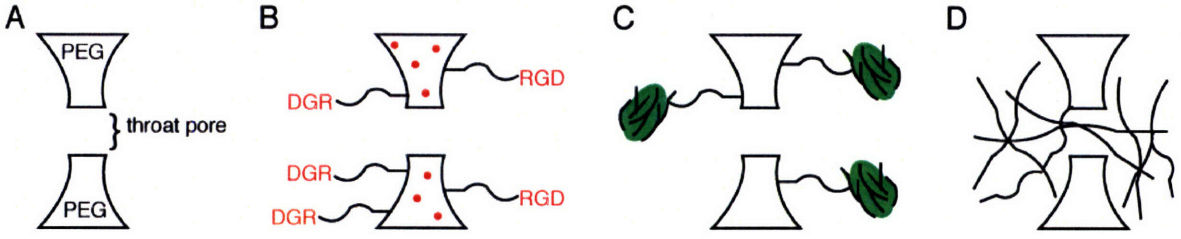

Figure 4-1 **Strategies for preparing adhesive scaffolds.** (A-D) depict a small portion of a macroporous PEG scaffold. (A) Schematic indicating scaffold parts. (B) Schematic of peptide labeling strategy: short adhesive peptides such as RGD were attached to cross-linked PEG scaffolds by PEG tethers. Red dots represent the co-polymerization of tethered RGD throughout the gel. (C) Schematic of protein attachment strategy: whole proteins (green globules) were attached specifically to scaffold surfaces by binding to functionalized PEG tethers after scaffold fabrication (functional bridging groups not shown). (D) Schematic of composite scaffold strategy: collagen gel was infused into PEG scaffolds after fabrication. Schematics not to scale.

To enhance T cell adhesion, we next functionalized scaffold surfaces with full-length adhesion proteins instead (Figure 4-1C). In particular, we tested intercellular adhesion molecule-1 (ICAM-1), an adhesion receptor expressed by lymph node fibroblasts and dendritic cells (178, 179) that normally line the ECM of lymphoid tissues (3, 6), and fibronectin, an extracellular

matrix protein that may be presented to T cells by reticular fibroblasts (5). T cells express the cognate receptors LFA-1 for ICAM-1 (170) and VLA-4 and VLA-5 for fibronectin (199). However, we found that T cells adhered only modestly to ICAM-coated scaffolds (and not at all to those coated with fibronectin), even in the presence of the adhesion- and migration-promoting chemokine CCL21. The cells exhibited a relatively poor ability to migrate from pore to pore within the 3D scaffold structure, irrespective of pore sizes.

This prompted us to evaluate a third strategy, this time forming a composite scaffold in which a fibrillar collagen matrix was polymerized in the internal voidspace of a PEG inverse opal hydrogel (Figure 4-1D). By this approach, we sought to combine collagen gels' ability to support rapid amoeboid migration of T cells (200-202) with the mechanical robustness and chemical flexibility of inverse opal synthetic gels. In these composite structures, T lymphocyte and DC loading into scaffolds was enhanced, and further, T cells were capable of rapid pore-to-pore migration. Finally, we implemented a strategy using heparin-conjugated PEG scaffolds to bind the chemokine CCL21 on the walls of the inverse opal supporting structures, as a potential means to deliver lymphoid tissue induction/motility signals within the composite scaffolds. These results demonstrate the successful fabrication of a scaffold supportive of lymphocyte migration, which could be further developed for use in cancer immunotherapy or to study factors controlling *de novo* formation of lymphoid tissue at ectopic sites.

The cellular environment in the lymph node is complex, even within the T zone alone. Because of their central role in the immune response and highly dynamic behavior, we were especially interested in T cells. However, in addition to our work with T cells, we also studied the behavior of dendritic cells and lymphoid stromal fibroblasts in lymphoid scaffolds, and this work will also be described in the proceeding chapter.

4.2 Materials and Methods

4.2.1 Scaffold chemistry and fabrication

Inverse opal scaffolds were prepared as described in sections 2.2.1- 2.2.4. For whole protein attachment, biotin-PEG-monoacrylate (biotin-PEGA) was included in the hydrogel precursor solution at 1:500 biotin-PEGA:PEGDMA by moles. Biotin-PEGA was prepared by mixing 1:1 moles EZ-link biocytin (Pierce) with acryloyl-PEG-NHS (Nektar Therapeutics) for 2.5 h in 0.1 M sodium bicarbonate buffer (pH 8.3), followed by dialysis for 1h (500 MW cutoff, Spectrum Laboratories, Inc.), filtering and lyophilization. Like peptide-PEGA, biotin-PEGA was stored at –20 °C in ~40 mg/mL aliquots.

4.2.2 NR6 fibroblast adhesion to PEG-RGD gels and scaffold

Adhesion of mouse fibroblasts (NR6 (203), a gift from Dr. Douglas Lauffenburger) to PEG gels modified with tethered RGD peptides was confirmed after the method of Hern and Hubbell (204). Thin solid gel films (22x22 mm^2, ~200 μm thick) were prepared by casting 100 μL of hydrogel precursor solution between glass slides and irradiating with a UV lamp for 90 seconds. Films were moved to 6-well polystyrene culture plates, pinned flat by sterile aluminum rings, sterilized with 70% ethanol, and exchanged into sterile complete RPMI culture medium. NR6 cells (5 x 10^3) were seeded on films in RPMI with or without 10% FCS, and incubated at 37°C 5% CO_2 for up to 12 hours. Per condition, three random fields were observed, and the number of both round and spread cells was recorded.

NR6 cells were also observed within PEG-RGD scaffolds. Fibroblasts (~$1x10^6$ per scaffold) were labeled with PKH26 red membrane dye (Sigma) according to the manufacturer's protocol, then loaded into scaffolds. Cells were incubated for 6-8 h, then fixed and stained with DAPI nuclear dye (Invitrogen) prior to observation.

4.2.3 T cell migration in PEG-RGD scaffolds

Primary $CD4^+$ T lymphocytes were isolated from the lymph nodes of OT-II mice and activated by exposure to peptide on the surface of gamma-irradiated antigen-presenting cells. These cells, or cells from the D10 $CD4^+$ T cell clone, were loaded into scaffolds by pipetting (10^6 cells in 20 μL with shaking for 15 minutes at 100 rpm). Cell-scaffold constructs were observed in time-lapse by optical microscopy.

4.2.4 Protein conjugation to biotinylated scaffolds

Fibronectin from bovine plasma (Sigma) was biotinylated using sulfosuccinimidyl-6'-(biotinamido)-6-hexanamido hexanoate (Pierce) per the manufacturer's instructions. Recombinant ICAM-1 (R&D Systems) was biotinylated using the Biotin-XX Microscale Protein Labeling Kit (Invitrogen) according to the manufacturer's instructions. For protein attachment, biotinylated scaffolds were sequentially incubated for 12-24 h at 4 °C with shaking in the following solutions: (1) 1 mL of 1 μg/mL streptavidin (SAv) or SAv-Alexa-647 (Invitrogen) in pH 7.4 phosphate buffered saline (PBS), (2) 1.5 mL PBS (2-3 exchanges), (3) 0.5 mL of 10 μg/mL biotinylated protein in PBS. Prior to use in cell motility or fluorescent visualization experiments, scaffolds were washed once per hour for 4-6 h in PBS.

4.2.5 Scaffold immunostaining

Attachment of adhesion proteins and chemokines was confirmed by immunostaining of scaffolds using the following antibodies: 10 μg/mL FITC-conjugated anti-ICAM-1 clone 3E2 (Pharmingen), 1 μg/mL anti-fibronectin clone 10 (Pharmingen) followed by 2 μg/mL PE-conjugated anti-mouse IgG_1 (Invitrogen), or 10 μg/mL anti-CCL21 clone 59106 (R&D Systems) followed by 10 μg/mL Alexa-546-conjugated anti-rat IgG (Invitrogen). Antibody staining and wash steps (3 quick rinses, then soak) were performed for 12 h at 4°C with shaking. Finally, scaffolds were observed on a Zeiss Axiovert 200 epifluorescence or on a Zeiss LSM 510 confocal microscope.

4.2.6 Cell preparation and labeling for protein and composite scaffolds

All animal studies were approved by the MIT Committee on Animal Care, and carried out in accordance with federal, state, and local regulations. Mice were obtained from Jackson Laboratory. $CD4^+$ T cells were isolated from spleens of 6-12 wk-old male BALB/c mice by magnetic bead negative selection: splenocytes were treated with a cocktail of biotinylated antibodies (1 μg/mL each anti-CD8α, anti-CD11b, anti-B220, and anti-NK1.1) after erythrocyte lysis with ammonium chloride, tagged with anti-biotin magnetic beads (Miltenyi Biotech) and sorted on a MidiMACS column according to the manufacturer's instructions (Miltenyi Biotech). T cell blasts were prepared by culturing the isolated cells in tissue culture wells previously coated with 10 μg/mL anti-CD3 and anti-CD28 (for 90 min at 37 °C) in complete RPMI medium (RPMI 1640 containing 10% fetal calf serum, 2 mM L-glut, 50 μM 2-mercaptoethanol, 10 mM HEPES, 100 U/mL penicillin, and 100 μg/mL streptomycin). The activated cells were split 1:2

and treated with 5 ng/mL IL-2 after 48 h. Cells were >96% $CD4^+$ at both day 3 and day 6 (as determined by flow cytometry), and were used on day 4-5. A fraction of T cells (30% for migration experiments, 100% for loading experiments) were labeled with 0.5 μM carboxymethylfluorescein diacetate (CMFDA) or 2.5 μM Fura-2 AM according to the manufacturer's instructions (Invitrogen).

Dendritic cells were prepared following a modification of the procedure of Inaba (167) by extracting bone marrow from the femur and tibia of BALB/c mice and culturing the recovered cells in complete RPMI supplemented every two days with 5 ng/mL GM-CSF (Peprotech). Cells were typically used on day 6, following 16 h treatment with 1 μg/mL lipopolysaccharide (LPS) to trigger maturation (Sigma). In some experiments, DCs were prepared from C57Bl/6 mice expressing enhanced green fluorescent protein in all cells (EGFP mice).

BLS4 fibroblasts were a generous gift from Dr. Tomoya Katakai. Cells were cultured in RPMI 1640 medium, passaged regularly, and labeled with DiI dye according to the manufacturer's protocol (Invitrogen) one day prior to use. Cells were treated with EDTA and trypsin to separate them from each other and the culture surface, then loaded in scaffolds in the usual fashion (~ 500,000 cells per scaffold).

4.2.7 Cell migration studies in protein and composite scaffolds

Excess liquid was removed from inverse opal gels by aspiration and a suspension of T cells or dendritic cells was pipetted onto the scaffold 10-15 μL at a time for 2-3 total additions. After each addition, the suspension was incubated 3 min on the gel and then centrifuged into the scaffold on a well plate carrier for 1 min at 800 rpm. Cells were loaded at $5x10^8$ cells/mL in medium or $2x10^8$ cells/mL in bovine type I collagen (2.2 mg/mL, Inamed PureCol), containing 4 μg/mL CCL21 for scaffold experiments, and 2 μg/mL for experiments in collagen alone. Cell-loaded scaffolds were observed on a Zeiss Axiovert 200 epifluorescence microscope equipped with a humidified environmental chamber (37 °C, 5% CO_2) and images were collected with a digital CCD camera (CoolSnap HQ, Photometrics) using Metamorph software (Molecular Devices, Inc.). To track single-cell migration, time-lapse images were collected for 40 min in 30 s intervals using a 40x oil immersion 1.3 N.A. objective. At each interval, a single fluorescence plane and a 10-plane z-stack of brightfield images collected through a total depth of 20 μm were collected in rapid succession using a high-speed pieozoelectric objective motor (Physik Instrumente).

4.2.8 Cell adhesion studies in protein and composite scaffolds

BLS4 fibroblast cells ($0.5\text{-}2.5x10^7$cells/mL) or dendritic cells ($1\text{-}5x10^8$ cell/mL) were loaded into scaffolds using the same procedure described for T cells (see previous section). However, BLS4 were kept in minimal amounts of medium (<100 μL) for 20-60 minutes to allow them to partially attach prior to addition of a larger pool of fresh warm medium (250-400 μL). Cell-scaffold constructs were observed after 0-24 h on an epifluorescence or confocal microscope maintained at 37 °C.

4.2.9 Migration analysis

Maximum projections of brightfield image stacks were prepared in Metamorph software. Individual cells were traced in brightfield or fluorescence images and tracked using Volocity software (Improvision, Inc.). For quantitative measurements, 15 cells were tracked for each of 2-

3 independent experiments. Statistical significance of measured differences in migration parameters was determined using one-way ANOVA, followed by Bonferroni's multiple comparison test for all pairs of samples, and Dunnett's test for all treated samples vs. controls (GraphPad Prism software).

4.2.10 Scaffold cross-section observation

Cell-loaded scaffolds were fixed in 4% paraformaldehyde (PFA) at 4 °C overnight, cut with a razor, and observed on a Zeiss LSM 510 confocal microscope using a 40x water immersion 0.8 N.A. objective. Alternatively, PFA-fixed scaffolds were dehydrated in ethanol and prepared for scanning electron microscopy as described in section 2.2.5.

4.2.11 Chemokine adsorption to scaffolds

Streptavidin-conjugated scaffolds were incubated with 0.5 mg/mL aqueous biotinylated heparin (Sigma, average MW 15 kDa), then washed in deionized water for 12 h each. Recombinant CCL21 (R&D Systems) was reconstituted in PBS with 0.1% bovine serum albumin (BSA) at 100 μg/mL, then diluted in water just prior to use (5-10 μg/mL). Heparin scaffolds were incubated in 0.3 mL of the diluted solution for 12-16 hrs at 4°C, followed by washing for 4 or 24 hrs with PBS/1% BSA depending on the subsequent assay.

4.3 Results

4.3.1 Integration of cells and porous hydrogel scaffolds

In the course of integrating cells with our newly developed porous scaffold, we pursued several cell loading strategies. These were modified over time depending on the properties of the current scaffold as it went through several stages of development, as well as depending on the cell type to be added.

The two main strategies we studied were pipetting of cells onto the scaffold and injection of cells into the scaffold. Either of these could be further modified by a centrifugation step (meant to improve cell loading in the center of the construct) or by an incubation and/or shaking step (also meant to improve uniformity of loading, and give time for adhesive cells to attach prior to the construct being moved to the observation dish). Injection by needle had the drawback of damaging the scaffold, difficulty in attaining reproducibility of cell entry and distribution, and the possibility of shear stresses harming the cells. Injection also appeared to work best when using scaffolds that were covalently attached to slides modified with silane-acrylates and a thin film of non-porous PEG; this way cells could not escape through the bottom of the porous gel, and were forced back up into the scaffold. However, attachment of scaffolds to glass slides reduced the surface area available for mass transport, and thus required harsh organic solvents (dichloromethane) to fully remove the templating microspheres.

Ultimately, we settled on the following basic procedure: 1) cells are suspended at high concentration in a small volume of medium (or collagen); 2) this suspension is pipetted on top of the scaffold, and incubated for a few minutes at 4 or 37 °C; 3) the scaffold-cell construct is briefly centrifuged to improve uniformity of cell loading; 4) the construct is placed in a pool of fresh medium or collagen. Although cell distribution continued to vary somewhat across

different fields of the scaffolds, and from scaffold to scaffold, this method was comparable to injection in final result without any of the drawbacks. In the main, our cell loading studies revealed that small, non-adhesive cells such as T lymphocytes require very high cell concentrations (>100M cells/mL) for sufficient loading within a macroporous scaffold, due to poor loading efficiency. Cell losses due to flow over the top and sides of the scaffold, as well as potentially from the surface pores, were the cause of this low efficiency. For large cells such as fibroblasts, a (100-1000)-fold lower cell concentration could be used.

An example of uniform cell loading is shown in the low-magnification scanning electron micrograph below of dendritic cells in a scaffold with a 40 μm void size (Figure 4-2). This protein-coated scaffold allowed some attachment of DCs, as shown in the higher magnification view. Examples of fibroblast cell loading will be shown in sections 4.3.3.5 and 4.3.4.5. We were most interested in T cell loading in scaffolds, as well as most challenged by it, due to the poor adhesiveness of T cells. As described in section 4.3.4, we found that the use of collagen gel within the synthetic polymer scaffold dramatically improved cell loading and retention.

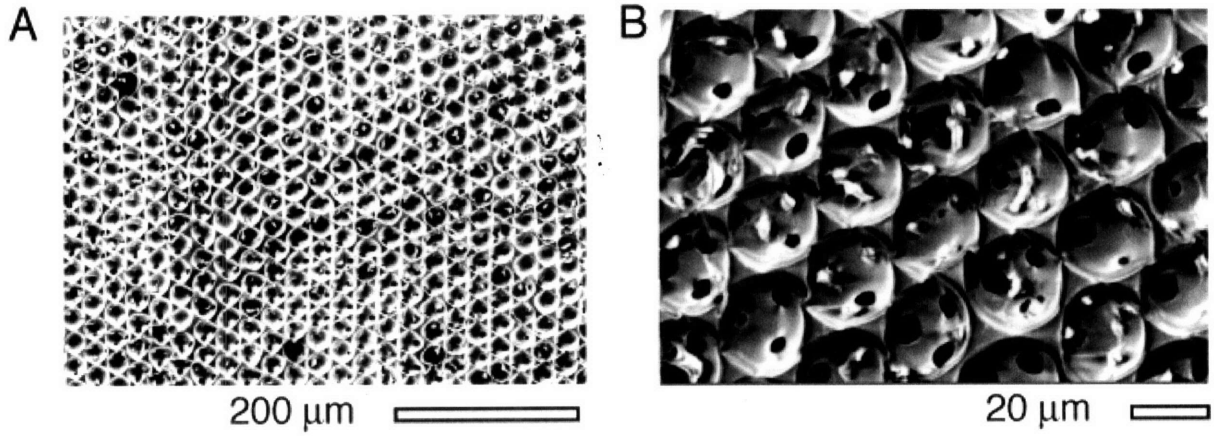

Figure 4-2 **Example of cell loading in protein-coated scaffolds.** (A) Scanning electron micrograph demonstrating dendritic cell loading across a large section of a protein-coated scaffold surface (original magnification 100x). (B) Closer view of cells attached to walls of scaffold (original magnification 800x).

4.3.2 PEG scaffolds with tethered adhesion peptides

PEG networks are readily functionalized with short peptides that support cell adhesion via specific integrin cell surface receptors (72, 77, 125). Given the simplicity of this approach, we began our studies by synthesizing PEG monoacrylates conjugated with the adhesion peptide (135) GWGRGDSP (RGD-PEGA), and tested the response of several cell types to these gels.

We first demonstrated that the RGD tethered to our PEG scaffolds remained functional after the fabrication process, which includes a long treatment in acetic acid. Since lymphoid stromal cells were not available at the outset of this thesis, we initially studied the response of generic fibroblasts to peptide-containing bulk gels and scaffolds. Specific adhesion of mouse fibroblasts expressing $\alpha_v\beta_3$ and $\alpha_5\beta_1$ integrins (NR6, (205)) to PEG gels modified with tethered RGD

peptides was confirmed after the method of Hern and Hubbell (204). Briefly, NR6 cells were seeded onto bulk gel films in cell culture medium with or without 10% fetal calf serum. The gels had been previously soaked in acetic acid and PBS to mimic the templated scaffold processing. As shown in Figure 4-3, 91.2 ± 1.8 % of cells spread on the RGDSP-containing gels by 12 hrs, while less than 1% of cells spread on control gels containing RDGSP in the presence of serum. Adhesion was well maintained under serum-free conditions (76.7 ± 5.7%), and did not occur in the presence of competitive soluble RGD ligand at short times.

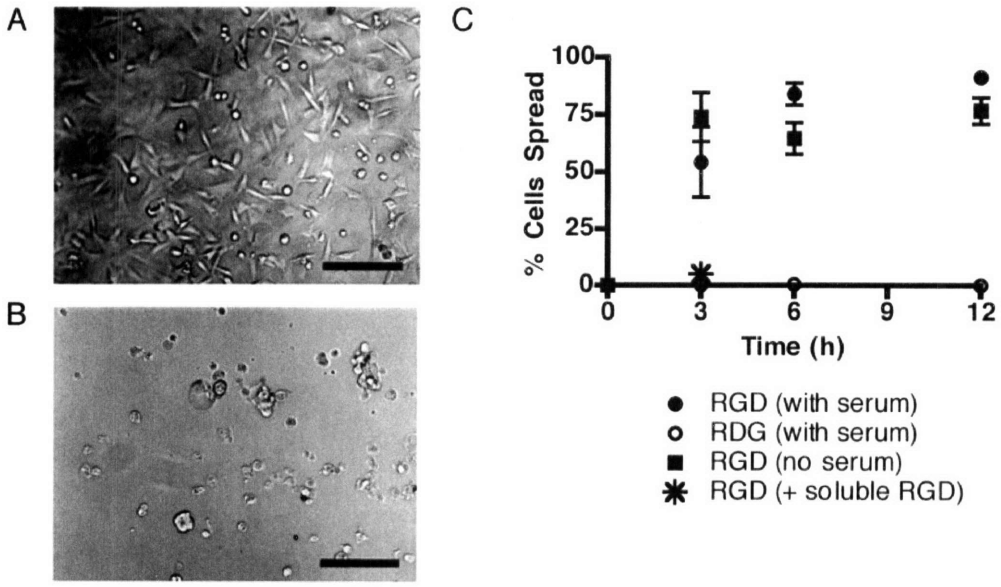

Figure 4-3 **Fibroblasts spread on RGD-modified bulk hydrogels.** (A) Brightfield images of NR6 fibroblasts spread on RGD-modified hydrogel films. (B) Brightfield images of films presenting RDG, on which fibroblasts were primarily rounded and clumped up. (C) Quantitative analysis of cell spreading on both films, with controls.

When we placed these fibroblasts in RGD-modified scaffolds, they were able to attach, spread, and remain viable over at least several days when cultured within scaffolds *in vitro* (Figure 4-4). We next loaded the RGD-functionalized scaffolds with a more motile cell type of interest to us – T cells. We used both a constitutively migratory T cell clone and activated primary T cells isolated from lymph nodes of OT-II mice, in order to address two issues. We aimed to discover both whether the scaffold architecture was open enough to sustain migration by moving cells and whether the scaffold adhesion peptides were relevant for primary T cells. We found that the connected cellular structure of templated gels provided functional pathways for cell migration within the scaffold: cells could readily traverse the interconnecting pores throughout the matrices in three dimensions (illustrated by time-lapse images shown in Figure 4-5). However, a majority of primary cells did not travel very far and seemed to readily detach from the walls of the structure, indicating that the RGD peptide may provide poor support for adhesion of primary T cells.

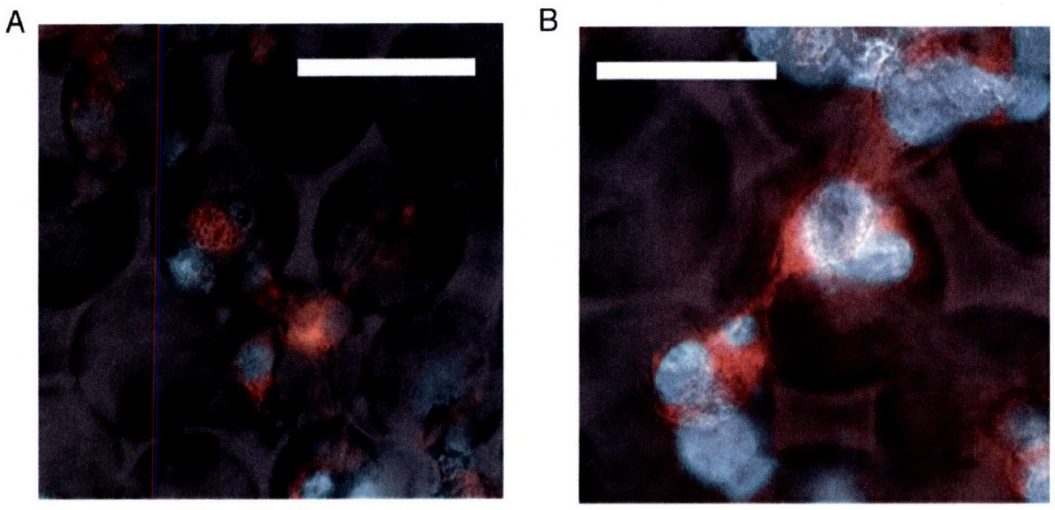

Figure 4-4 **Cell attachment in templated PEG-peptide hydrogels.** Overlaid brightfield optical and fluorescence micrographs of stained NR6 fibroblasts spread on RGD-functionalized PEG scaffolds with 40 (A) and 60 (B) μm void sizes, after 24 hrs (scale bars 50 μm). Fluorescence staining of cells within scaffold: red, PKH26 membrane dye, blue, DAPI nuclear stain.

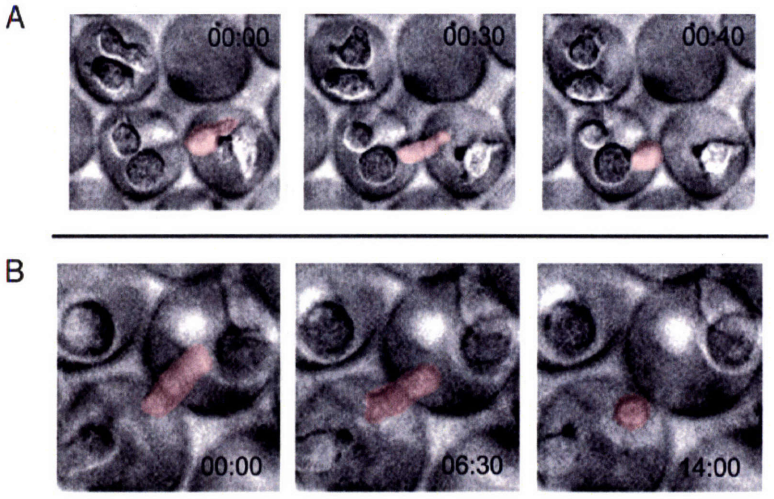

Figure 4-5 **Cell movement through templated PEG-peptide hydrogels.** (A-B) Time-lapse brightfield optical microscopy images of T lymphocytes migrating through throat pores in scaffolds. Primary $CD4^+$ T cells isolated from OT-II mice (A) and $CD4^+$ T cells (D10 clone) (B) are shown migrating in scaffolds with 20 and 30 μm voids, respectively. Times are elapsed min:sec; the cell of interest in each case has been identified with a false-color overlay.

4.3.3 PEG scaffolds surface-functionalized with whole adhesion proteins

Due to the limited response of primary T cells to peptide-functionalized scaffolds, we developed a method to coat scaffolds with whole adhesion proteins instead. Peptides typically consist of a single recognized epitope for binding, and thus provide incomplete adhesion signals to cells compared to proteins, which have multiple epitopes arranged in conformations ideally suited to binding. Despite the superior binding affinity of proteins compared to peptides, when we loaded T cells into scaffolds coated with intact ECM proteins such as fibronectin, we found no improvement in T cell motility. In contrast, scaffolds coated with ICAM-1 (normally a cell-cell adhesion protein) prompted robust migration in a fraction of T cells. We also observed the behavior of dendritic cells and stromal fibroblasts in protein-coated scaffolds, because of the importance of these cells in immune responses and lymph node structure, respectively. Both cell types formed adherent networks in the scaffolds, and DCs were able to migrate along scaffold walls. These experiments are elaborated in sections 4.3.3.1 – 4.3.3.5 below.

4.3.3.1 Functionalization of inverse opal hydrogels with lymphoid tissue-associated adhesion proteins

In Chapter 2 we reported a strategy for preparing macroporous hydrogel scaffolds by colloidal crystal templating, which could be functionalized with covalently tethered adhesion peptides incorporated during polymerization of the gel matrix (see Figure 2-1, and (194)). Due to the poor adhesion of most primary T cells to RGD-functionalized gels (as described in the previous section), we developed an alternative strategy to support T cell attachment and migration: conjugating full-length adhesion proteins to all of the internal and external free surfaces of porous scaffolds post-fabrication (see Figure 4-6). The method we developed to attach protein to scaffolds utilized biotin-streptavidin binding, which is one of the strongest naturally occurring non-covalent bonds in biological systems (with a dissociation constant K_D close to 10^{-15} M, (206)). Biotin was conjugated to the scaffold by first reacting biocytin (biotin-lysine, which has a single available amine group) with NHS-PEG-monoacrylate (Figure 4-7), then co-polymerizing the biotin-PEG-acrylate with PEGDMA as before (Figure 4-6). Finally, protein was conjugated to the resulting surface-accessible biotin groups by incubating templated scaffolds in a streptavidin solution followed by washing and binding of biotinylated ICAM-1 or fibronectin.

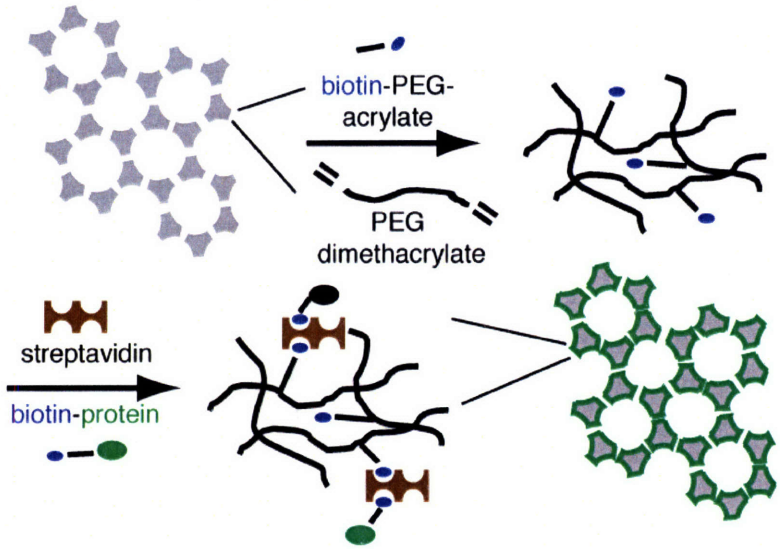

Figure 4-6 **Schematic demonstrating method for protein attachment to hydrogel scaffolds.**

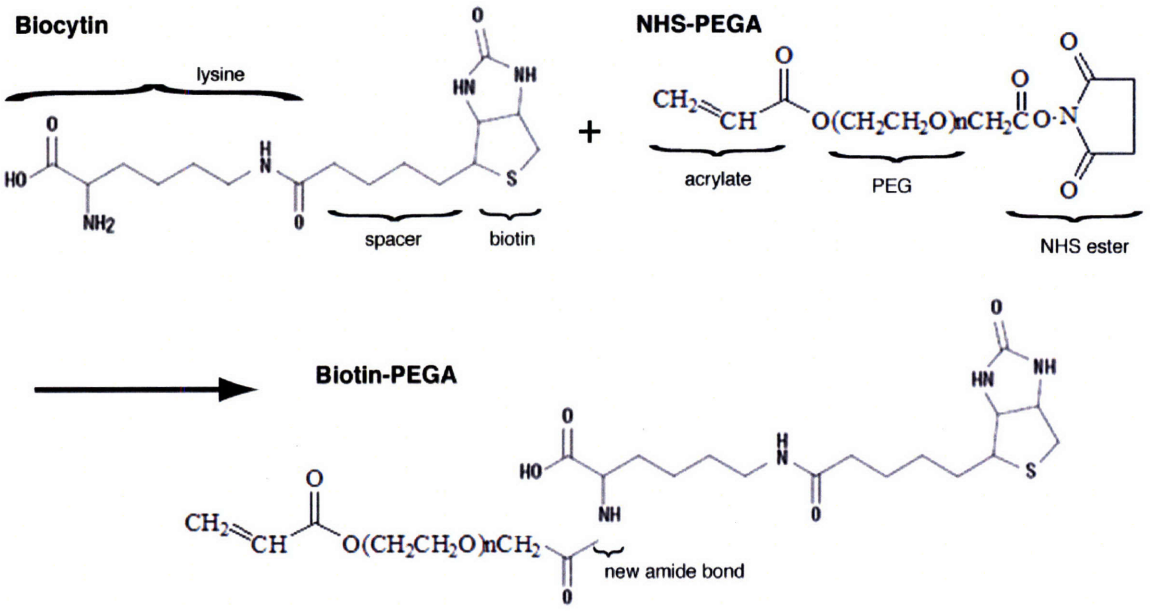

Figure 4-7 **Schematic of biotin-PEG-acrylate preparation.** NHS is N-hydroxysuccinimide ester; PEGA is poly(ethylene glycol) acrylate.

Inverse opal PEG scaffolds synthesized with 0.2 mole % biotin-PEG-acrylate (99.8 % PEG-dimethacrylate) avidly bound streptavidin on all of the interior surfaces of the 3D macroporous structure, as evidenced by confocal fluorescence images of biotinylated scaffolds following exposure to fluorescent streptavidin solutions and washing to remove unbound protein (Figure 4-8A). Confocal optical sectioning of scaffolds revealed that protein binding was largely confined to the surfaces of the scaffold pores and did not penetrate throughout the interior of scaffold struts, suggesting that the mesh size of the gel is too small for rapid diffusion of streptavidin into the PEG network. This is particularly apparent on a strut widened due to a template defect, as indicated by the arrow in Figure 4-8A, which highlights the lack of labeling on the interior of the 'solid' gel strut.

Once we had successfully prepared streptavidin-conjugated scaffolds, we biotinylated proteins at a fraction of their free amine groups by succinimidyl ester chemistry. The success and degree of the protein biotinylation reaction were demonstrated by measurement of biotin groups on the adhesion proteins: 10 biotin groups per fibronectin were observed by the HABA assay, while 4-6 biotin groups per ICAM-1 were observed by a FRET-based assay that requires only miniscule amounts of protein (see Appendix E.2).

To demonstrate specific coupling of these adhesion proteins to scaffolds, and to assure that protein incubated with the scaffold after the streptavidin conjugation step would remain attached, we performed immunostaining. Streptavidin-coated gels were incubated with biotinylated proteins, washed, and then stained with appropriate primary and secondary antibodies against either fibronectin or ICAM-1. Both proteins were robustly detected on the scaffold surfaces (Figure 4-8, B and C). The image section shown for ICAM-1 is slightly deeper into the scaffold than the section shown for fibronectin, and demonstrates that the proteins penetrate beyond the first layer of the scaffold. Thus, this conjugation strategy allows adhesion proteins to be coupled to the internal surfaces throughout inverse opal hydrogel scaffolds.

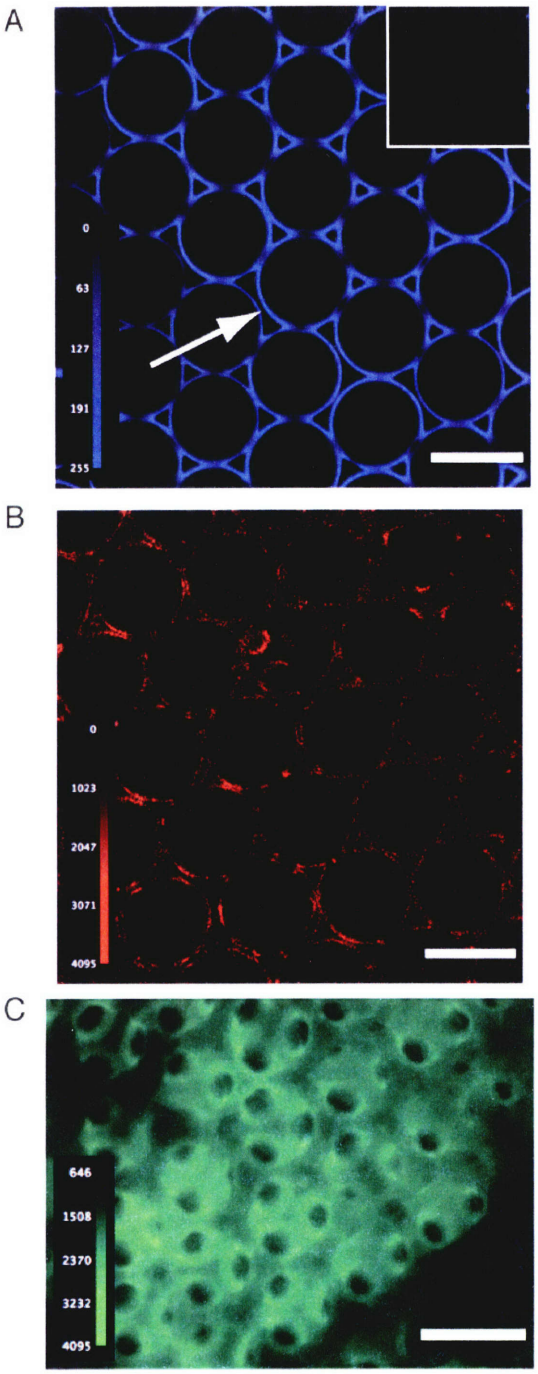

Figure 4-8 **Functionalization of macroporous hydrogels with whole proteins**. (A) Confocal images of a biotinylated scaffold (main) and a control non-biotinylated scaffold (inset) exposed to fluorescent streptavidin under the same conditions. Scale bar 41 μm. (B-C) Biotinylated proteins attached to streptavidin-conjugated scaffolds were detected by immunostaining. (B) Attachment of fibronectin is shown as obtained from confocal microscopy following immunostaining with an unlabeled rat anti-fibronectin and a phycoerythrin-conjugated anti-rat antibody (scale bar 41 μm). (C) Staining of ICAM-1 attached to a scaffold is shown in epifluorescence using a FITC-conjugated anti-ICAM-1 (scale bar 48 μm).

4.3.3.2 *T cell migration in protein-coated scaffolds*

We next characterized the migration of T cells within protein-coated and unmodified scaffolds. In these studies, we utilized murine primary T cells primed *in vitro* by antibodies to CD3 and CD28. Such activated cells may be expanded in great numbers from a single animal, and also are larger and constitutively more migratory than naïve T cells, making them a good candidate for screening the activity of different adhesion proteins coated on scaffolds. Although as a chemoattractant the lymphoid tissue chemokine CCL21 is known to be particularly potent for naïve T cells (21), with regard to chemokinesis we observed similar effects of CCL21 on activated T cells as those described in Chapter 3 for naïve T cells. Thus, we added CCL21 (at ~ 4 μg/mL) to promote cell motility within scaffolds loaded with fluorescently labeled T cell blasts. Cell migration was recorded by time-lapse brightfield and fluorescence videomicroscopy and analyzed at the single-cell level.

Unmodified PEG scaffolds with a 40 μm void size supported no T cell attachment and T cells were unable to migrate between pores of these structures (Figure 4-9A). T cells remained equally non-motile in fibronectin-coated scaffolds, even if present at high cell densities that forced many cells into contact with the walls. In contrast, ICAM-1 coated scaffolds supported avid migration for ~30% of loaded T cells even at low cell densities, as shown by representative cell migration paths (Figure 4-9B), and further evidenced by quantitative comparisons between cell motility in each of the scaffold conditions (Figure 4-9, C-F). In uncoated scaffolds, the average cell velocity was 4.3 μm/min, a somewhat high resting value due to jostling of the CCL21-stimulated T cells as they extended lamellipodia; however, no cells neared the typical ~10 μm/min values observed *in vivo* (116, 207). This average increased to ~ 6.1 μm/min for cells in ICAM-1 coated scaffolds, with several cells migrating at 7-8 μm/min and reaching maximum displacements of 40-60 μm in 15 min. However, many cells circled within their initial voidspace without traversing throat pores, as evidenced by the relatively high turning angles for all samples. The confinement ratio, defined as the end displacement divided by total distance traveled, also remained low (indicating significant confinement of the cell path) irrespective of the presence of fibronectin or ICAM-1. Although statistically significant changes in motility were seen for T cells in ICAM-1-coated scaffolds vs. unmodified scaffolds in all four parameters examined, the population behavior of T cells crawling in ICAM-1 coated scaffolds did not approach the rapid migration and high confinement ratios (low confinement) observed for T cell migration *in vivo*.

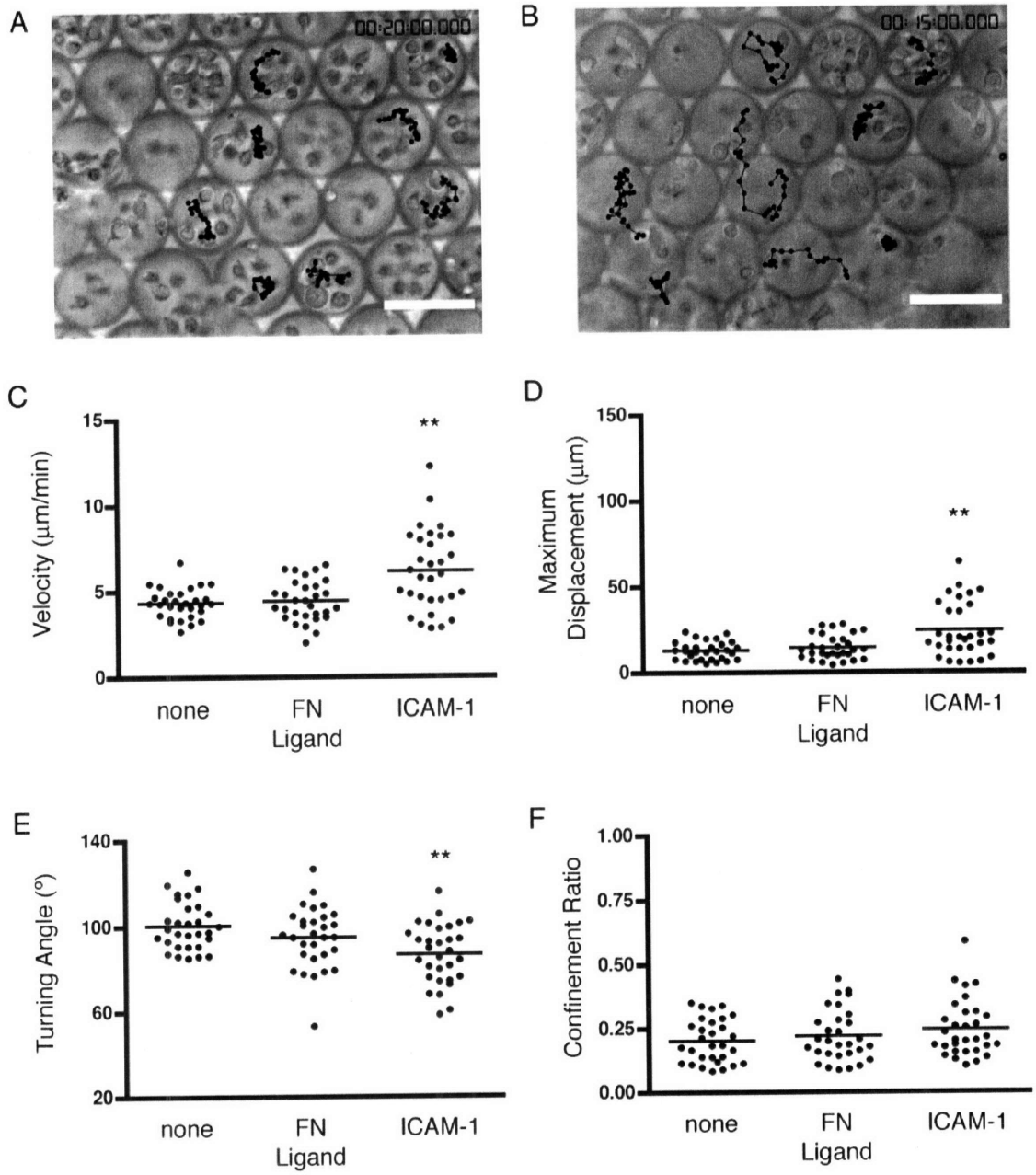

Figure 4-9 **A fraction of T cells migrate in ICAM-1 conjugated scaffolds.** (A-B) Brightfield images with overlaid migration paths of several representative T cells in a control scaffold (A) or ICAM-1 coated scaffold (B) over 15 min. Scale bars 48 μm. (C- F) Time-averaged migration properties of individual T cells in scaffolds, namely velocity (C), maximum displacement (D), turning angle (E), and confinement ratio (F). Each cell was analyzed for a 15 min timecourse; 15 cells from each of 2 independent experiments were analyzed. ** indicates $p < 0.01$ compared to no protein sample.

4.3.3.3 Interaction of dendritic cells with protein-coated scaffolds

Dendritic cells present antigen to naïve T cells in order to activate them, thus playing a major role in the primary immune response. Intravital imaging has shown that DCs are present in the lymph node primarily as stationary networks, with newly antigen-loaded DCs that enter from the periphery at first maintaining moderate cell velocities, and then eventually joining the network. Despite this immobility, due to their long dendrites and the way they are organized on the lymph node fibers (17), DCs are readily able to contact many T cells; in fact, about 60% of T cells in lymph nodes are in contact with a DC at any give time (177). We thus briefly studied the behavior of dendritic cells alone in protein-coated scaffolds, to see if we could recreate DC networks *in vitro*.

We found that the morphology and migratory behavior of DCs on our scaffolds was highly heterogeneous, depending on their maturation state as well as on biochemical signals presented by the scaffold. DC networks similar to those seen *in vivo* were sometimes observed on scaffolds coated with the ECM proteins fibronectin and/or laminin, as shown in Figure 4-10. As *in vivo*, a fraction of DCs migrated rather than remaining stationary (see Figure 4-11). However, this spreading and/or migratory behavior was not observed in all experiments utilizing DCs. Bone marrow-derived DCs are a heterogeneous group of cells, so it is not surprising that the fraction of adherent or migratory cells might vary from batch to batch. Moreover, the tendency of DCs to spread out and/or migrate is influenced by their maturation state (5), and merely recovering cells by pipetting (as well as manipulating them to introduce fluorescent labeling) can cause some degree of maturation (208). Determining the exact conditions necessary and sufficient for DC network formation and/or crawling, perhaps by performing parallel analyses of DC spreading by microscopy and DC maturation state by flow cytometry, is an area ripe for further study.

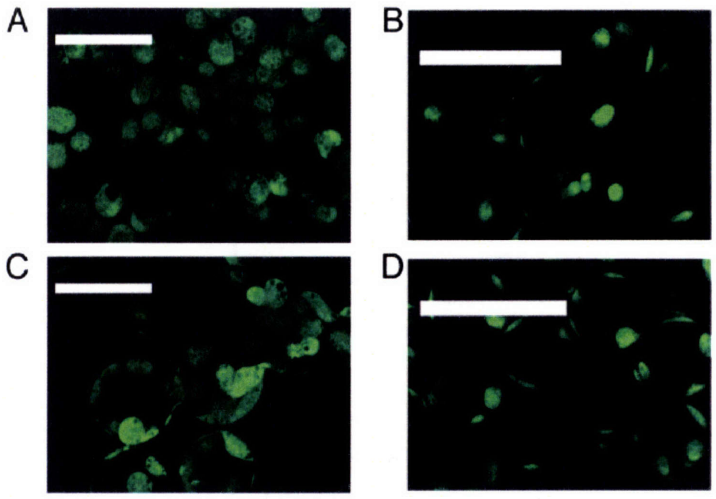

Figure 4-10 **Dendritic cell attachment to protein-coated scaffolds.** Overlays of brightfield and confocal fluorescence images are shown. Day 5 immature DCs were stained with CMFDA prior to loading in scaffolds. (A-B) DCs in scaffolds without protein remain primarily round after 2 h. (C-D) In fibronectin-coated scaffolds, ~50-70% of DCs are spread along the walls. Cells are shown at 40x magnification (A and C, scale bars 41 μm) and 20x magnification (B and D, scale bars 80 μm).

Figure 4-11 **Dendritic cell crawling on protein-coated scaffolds.** A dendritic cell is shown crawling along the wall of a laminin-coated scaffold pore. The DCs were derived from a transgenic mouse expressing enhanced green fluorescent protein in all of its cells and did not require external labeling.

4.3.3.4 Effect of CCL21 on naïve T cells in scaffolds with and without DCs

Having systematically studied the impact of homeostatic chemokines in a minimal, monolayer environment (see Chapter 3), we initiated some studies of CCL21-stimulated naïve T cells in our lymphoid tissue scaffolds, with and without DCs present. As on glass substrates, T cells exposed to CCL21 in lymphoid scaffolds exhibited striking morphology changes (see Figure 4-12). However, in medium pore sizes (40 μm) and in the absence of DCs, T cells did not migrate.

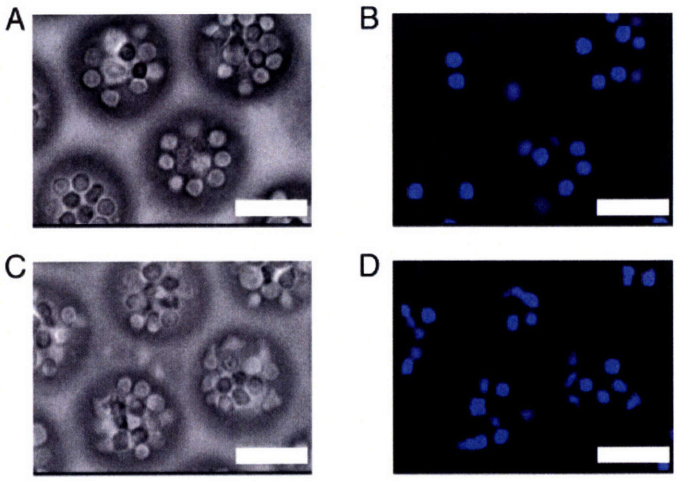

Figure 4-12 **CCL21 stimulation of naïve T cells in scaffolds.** Naïve T cells were added to fibronectin-conjugated scaffolds in the absence (A-B) or presence (C-D) of 1 μg/mL of CCL21. For improved visualization, ~50% of cells were labeled with fura-2AM dye. Brightfield (A and C) and fluorescence (B and D) images of the same two fields are shown, and an increase in cell polarization in the samples treated with CCL21 is apparent. Scale bars 25 μm. This data is representative of at least five experiments.

In contrast to the inability of naïve T cells to migrate on protein-coated scaffolds, when DCs were added at a high ratio (~2:1 of DC:T cells) under conditions where DCs adhered to the scaffold walls, a fraction of T cells were able to migrate vigorously in the presence of CCL21.

Figure 4-13 shows the path of one such naïve T cell traveling on a DC body, which traverses the entire pore diameter (40 μm) in ~3.5 min. Other T cells in the same experiment were able to cross throat pores that were straddled by DCs. We saw similar results with activated T cells, and Table 4-1 shows the effect of DCs on single-cell migration parameters seen for both naïve and activated T cells. In the presence of DCs, maximum values in the cell population for maximum displacements, confinement ratios, and velocities all increase, while minimum values stay the same or slightly increase as well. Activated T cells are clearly more migratory than naïve T cells, but in these experiments only a small fraction of cells were able to migrate on DCs whether the cells were activated or not.

In conclusion, the presence of supporting cells (their type, number, and ratio) is one parameter that can substantially influences the migration of T cells. However, due to our interest in co-attracting (rather than sequentially attracting) any desired cell types in the ultimate application (tissue engineering immunotherapy), as well for simplicity, the majority of our studies focused on inducing migration in one cell type at a time rather than studying cell interactions within the scaffolds.

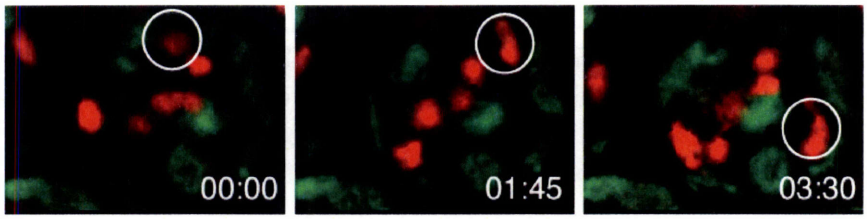

Figure 4-13 **Naïve T cell migration on DC 'carpets' in scaffolds.** Naïve T cells in the presence of both DCs and CCL21 were able to crawl along DC bodies within the scaffold structure, but were not able to migrate in scaffolds lacking DCs. An example of such migration is shown above, with T cells false-colored in red and DCs in green. Elapsed times are min:sec.

Table 4-1 **Effect of DCs on migration parameter ranges for T cells.**[a]

Sample[b]	Velocity (μm/min)	Maximum Displacement (μm)	Confinement Ratio
T_o - DCs	1.2 – 3.4	0.0 –17	0.07 – 0.34
T_o + DCs	0.56 – 5.5	2.3 – 25	0.08 – 0.55
T_b - DCs	2.5 – 4.4	8.9 – 18	0.07 – 0.15
T_b + DCs	3.5 – 7.9	11.6 – 57	0.10 – 0.76

[a] Migration parameters were determined for single cells, and the ranges of values observed in the entire population are shown.
[b] T_o are naïve T cells, and T_b are activated T cell blasts.

4.3.3.5 Lymphoid fibroblasts form networks in protein-coated scaffolds

Fibroblastic reticular cells (FRCs) surround the fibrous ECM scaffolding of the lymph node T zone, produce chemokines that act on lymphocytes (such as CCL21, (24)), and have long been inferred to influence T cell migration (2). In 2004, Katakai et al. derived a stromal cell line that expresses ER-TR7, one of the few proteins known to be produced specifically by FRCs in the lymph node T zone (178). Using this model cell line, Katakai showed that lymphocytes (and to a lesser extent inflammatory factors such as TNF-α and LT-β) promote ECM secretion by FRCs. Stromal cells in turn are known to improve T lymphocyte viability *in vitro* (209). FRCs also help maintain appropriate architecture in the lymph node via cell-matrix and cell-cell interactions, forming an interconnected living network in the T zone (4). Quite recently, the first dynamic *in vivo* demonstration that T cells in the lymph node preferentially crawl on FRCs was published (4). Due to their structural and functional importance in the lymph node, it would be desirable to have FRCs present in a tissue engineering construct for immunotherapy. We therefore briefly studied the response of lymphoid fibroblasts to the protein-coated version of scaffolds.

Using the FRC cell line derived in Katakai's group, we first studied whether a stromal cell network could self-assemble in our model lymphoid scaffolds. FRCs were initially round after being loaded into scaffolds, but over time spread and connected with other cells to form a network (see Figure 4-14, A-F). Network formation occurred only in the presence of the extracellular matrix protein fibronectin at short times. At longer times, some network formation could occur even in scaffolds lacking protein, perhaps due to the non-specific adsorption of serum proteins to the negatively charged groups (from the free carboxyl groups on biocytin) in the scaffold or due to ECM produced *in situ* by FRCs. It especially occurred in places where cells were nearby enough to contact each other. Unlike dendritic cells, which primarily lined the gel matrix walls, FRCs primarily extended processes that penetrated through interconnected pores; thus, the scaffold 'templates' the FRCs into an additional close-packed circular layer, which is offset from the porous gel template above and below those cells (Figure 4-14, C-F, Figure 4-15). This dictation of a regular cellular architecture by the ordered macroporosity is a unique feature of our system, and may find use in other tissue engineering applications.

In further contrast to DCs, this lymphoid fibroblast cell line appeared to have no influence on T cell migration in the co-loading studies that we performed (data not shown). However, it is possible that in an *in vivo* environment the fibroblasts might be exposed to factors that would upregulate adhesion molecules or otherwise influence their interaction with T cells. In support of this hypothesis, Bajenoff et al. recently showed *in vivo* that T cell migration within lymph nodes primarily occurs along FRCs (4). Thus, it is potentially useful to be able to support FRC networks in scaffolds for lymphoid tissue engineering applications.

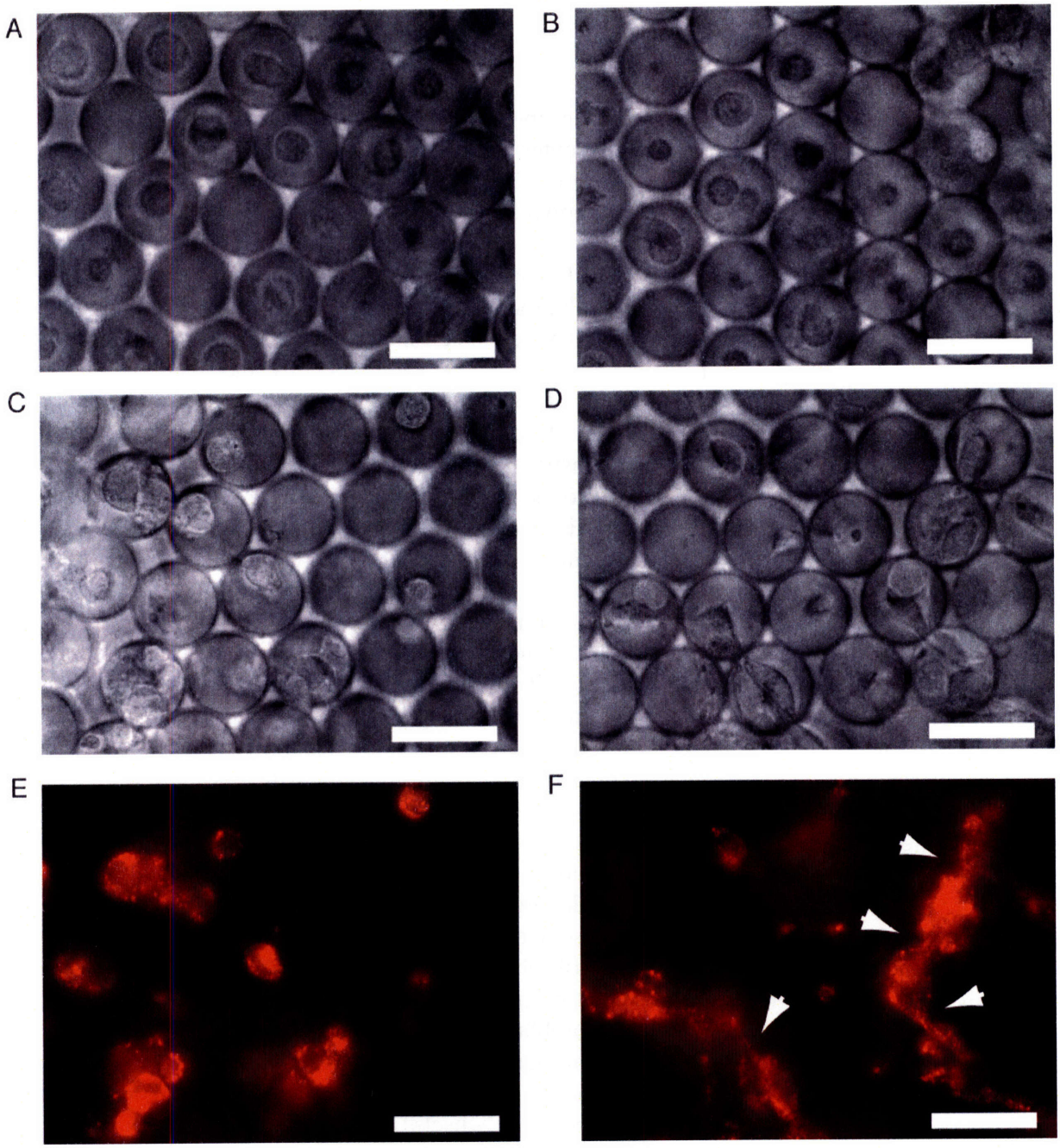

Figure 4-14 **Effect of fibronectin on lymphoid stromal cell network formation in scaffolds.** Cells from the BLS4 line were labeled with DiI fluorescent dye and loaded into unmodified (A, C, E) and protein-coated (B, D, F) scaffolds. (A-B) Brightfield images of cells just after loading. All cells are round at this time. (C-F) Brightfield (C-D) and red fluorescence (E-F) images after 9 h of cell incubation in scaffolds. Cells in the scaffolds without protein are slightly enlarged but do not extend many processes, while cells in the fibronectin-conjugated scaffold are forming multi-cell networks. Arrows indicate cell spreading through throat pores and multi-cell junctions. Areas of comparable cell density are shown. Scale bars 50 μm.

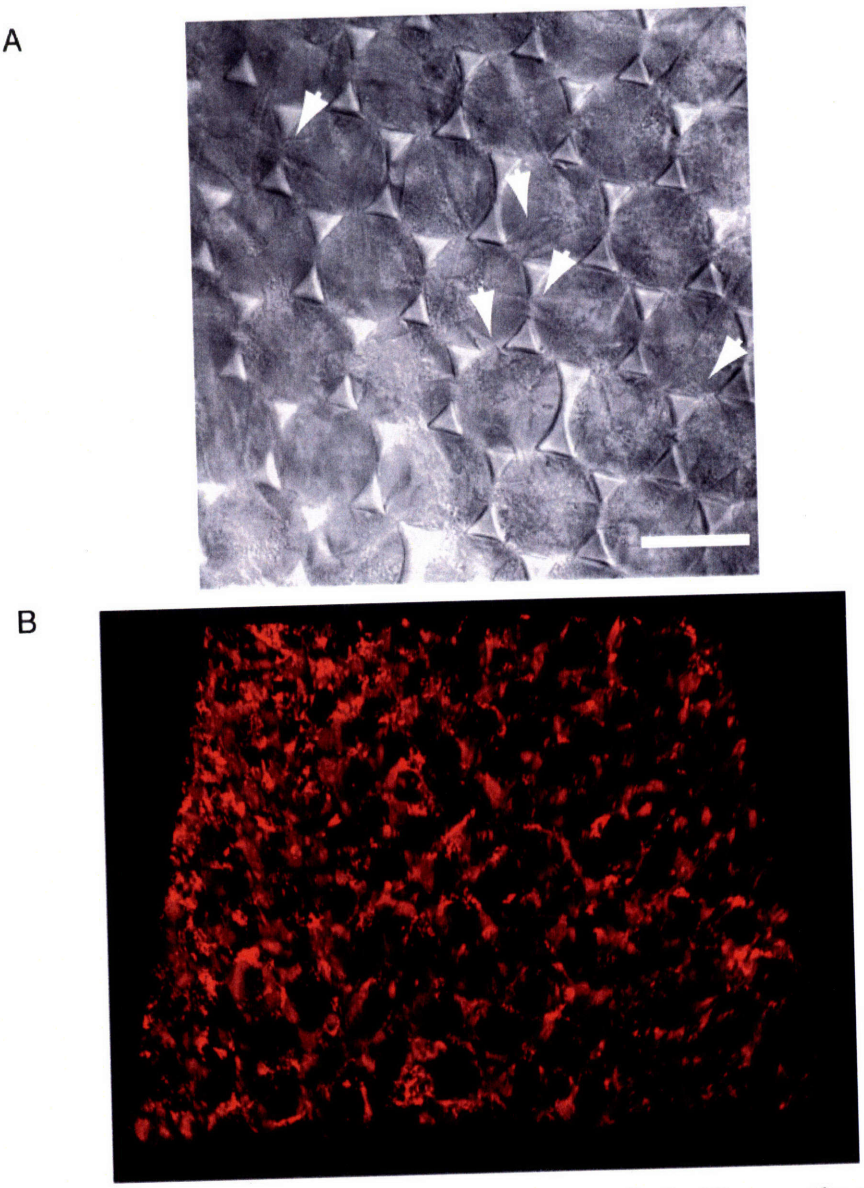

Figure 4-15 **Formation of large-area, 3D stromal cell networks in fibronectin-coated scaffolds.** (A) Brightfield image is shown from a porous layer near the scaffold surface, 16 h after seeding fibroblasts. Arrows indicate cell spreading through throat pores. Scale bar 41 μm. (C) A 3D view (~35 μm thick) of an extended FRC network made by computational reconstruction. Fibroblasts were labeled with DiI red fluorescent dye and observed at 14 h.

4.3.4 ***Polymer-collagen composite scaffolds for improved cell support***

Protein-coated scaffolds were a great improvement over peptide-containing scaffolds in promoting T cell motility, and also induced interesting networking behaviors by dendritic cells and lymphoid fibroblasts. More specifically, ICAM-1 presentation caused moderate migration in ~ 30% of T cells, while attachment of ECM proteins such as fibronectin and laminin promoted DC and FRC adhesion. However, as a therapeutic construct these scaffolds might be limited, as under no conditions that we tested (varying ligand, cell composition, and also pore size – not shown) did T cells migrate as rapidly as they are known to do *in vivo*. We reasoned that we could improve T cell migration, as well as cell retention, by loading collagen-cell suspensions within porous polymer scaffolds and then allowing the collagen to form a fibrillar gel. In this case, the polymer remains as a support with mechanical properties superior to collagen, allowing it to be implanted as a stable construct in tissue engineering applications. It also may be exploited for delivery of soluble factors, as will be described in section 4.3.5. Meanwhile, the collagen provides an excellent substrate for cell migration. As we did for the protein-coated scaffolds described in the previous section, we focused on T cell migration within composite scaffolds, but also briefly studied dendritic cell and fibroblast responses.

4.3.4.1 Fabrication of collagen-infused inverse opal scaffold

Though T cell migration was enhanced in ICAM-1-coated scaffolds relative to unmodified gel surfaces or fibronectin-coated structures, the majority of T cells exhibited low total displacement and remained confined to individual pores of the matrix for times exceeding 15 min. In contrast, T cells migrating through lymph nodes *in vivo* often travel 70-100 μm away from their origin within similar time spans (116). The videomicroscopy data from our experiments suggested to us that lymphocytes adhered weakly to the walls of the matrix and were easily dislodged by random contacts with neighboring cells or convective currents. To address these limitations we examined an alternative approach, in which we formed a composite matrix of PEG inverse opal hydrogels infused with a fibrillar collagen gel (Figure 4-16A). In this strategy, the inverse opal gel provides mechanical support (194) (and as shown later, the ability to reversibly bind chemokines) while a collagen matrix filling the voidspace of the inverse opal structure provides a physical meshwork that supports T cell migration (201, 202). To create the composites, cells suspended in collagen solution were pipetted onto PEG scaffolds rid of excess liquid, which imbibed the solution over periods of a few minutes at 4°C. Collagen fibrillogenesis and cell equilibration were then achieved by incubating the infused scaffolds at 37°C for 60 min.

The successful formation of the composite matrix was demonstrated by combined confocal reflectance (210) and fluorescence microscopy. The scaffold was visualized by conjugation of fluorescent streptavidin to its surfaces, while reflected light in the green and red part of the spectrum was used to visualize the collagen fibers polymerized in the scaffold voidspace (Figure 4-16B). The composite scaffold gave more reproducible results for cell loading and subsequent cell behavior, and allowed us to perform systematic studies of how architecture affects T cell migration. These studies are described in the following section.

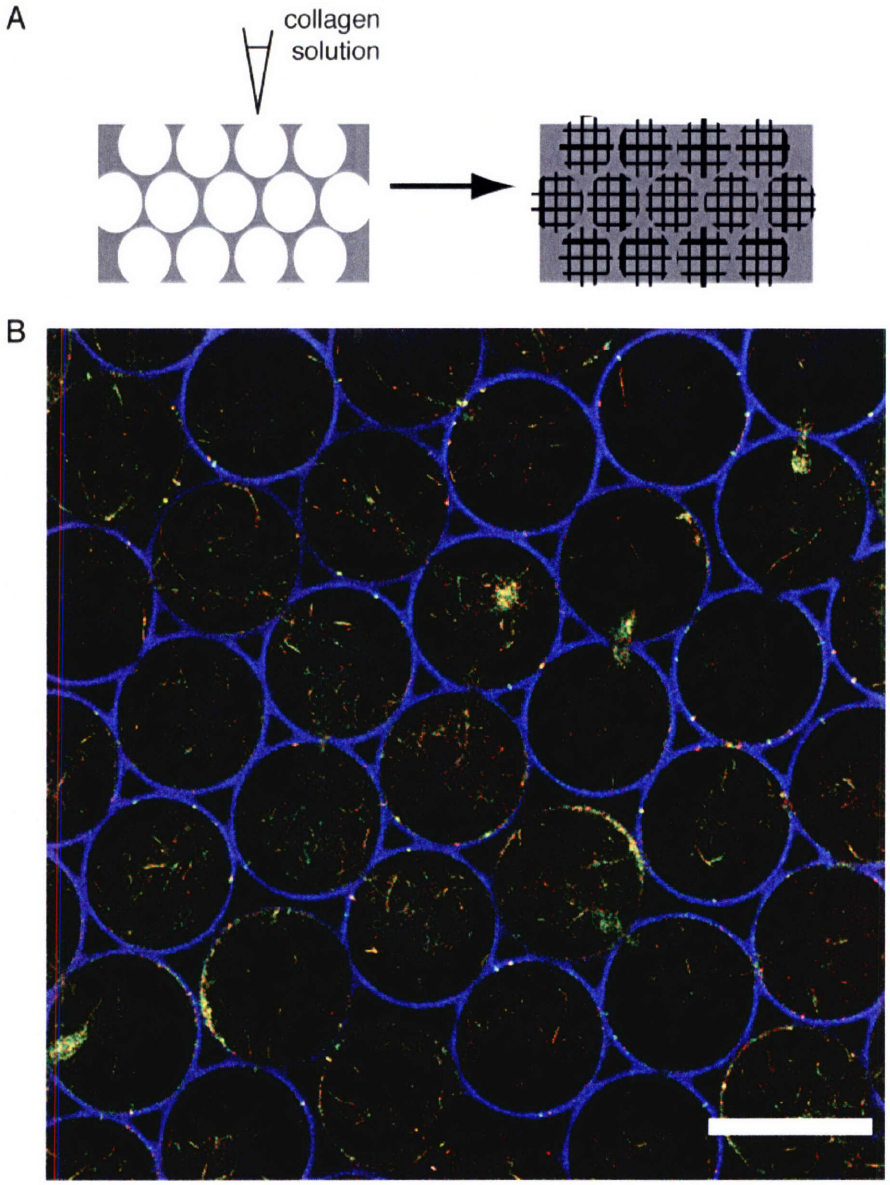

Figure 4-16 **Fabrication of composite polymer-collagen scaffolds**. (A) Schematic of composite scaffold fabrication. (B) Successful formation of composite was visualized by combined confocal reflectance (for collagen) and fluorescence (for scaffold labeled with fluorescent streptavidin) imaging. Collagen fibers are shown in green and red, scaffold is shown in blue. Scale bar 41 μm.

4.3.4.2 T cells migrate avidly in collagen composite scaffolds

Before examining T cell migration in inverse opal composite scaffolds, we first characterized T cell blast migration in neat 2.2 mg/mL collagen gels (i.e., in the absence of a supporting inverse opal structure) with or without the addition of the motility-stimulating chemokine CCL21, to provide a basis for comparison with the inverse opal composite matrices. As on 2D adhesive

substrates, we found that CCL21 treatment (at 2 μg/mL) of T cell blasts in 3D collagen also substantially increased their migration (Figure 4-17). Because activated T cells are more constitutively migratory than naïve T cells (156, 182, 183), a fraction migrated through collagen with *in vivo*-like characteristics even in the absence of CCL21. However, this fraction of highly motile cells was greatly increased by addition of CCL21 to the collagen gels, resulting in migration parameters similar to those seen *in vivo* (see also section 4.4), such as an average velocity of 8.9 μm/min (vs. 3.6 μm/min for the control), and an average turning angle of 53° (vs. 85° for the control).

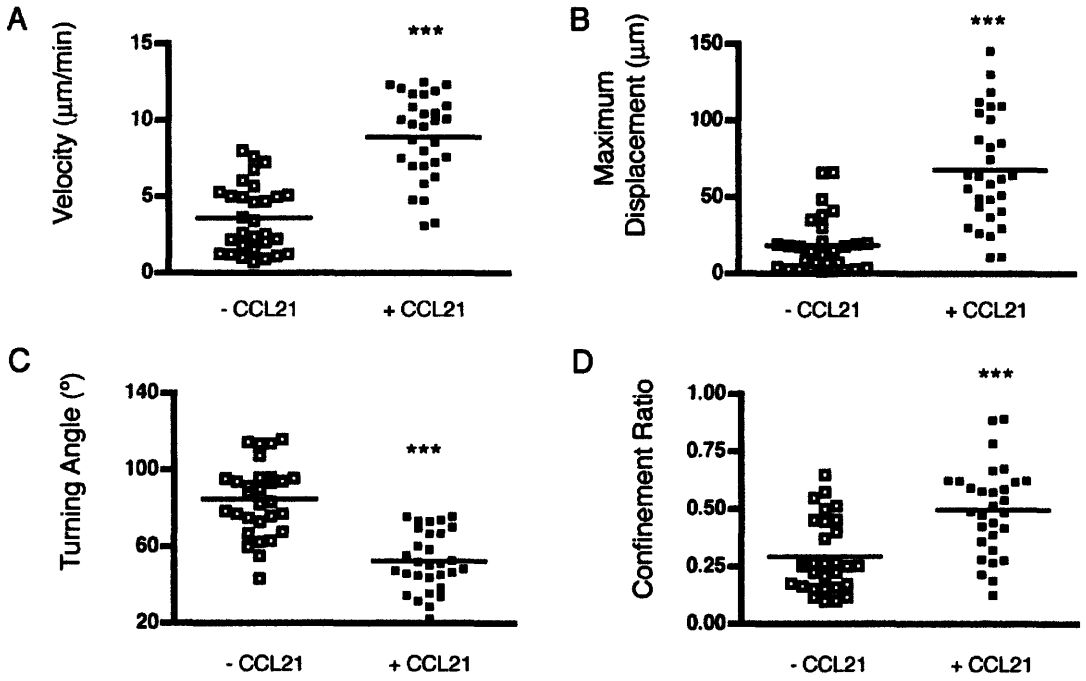

Figure 4-17 **The chemokine CCL21 enhances motility of primed T cells in 3D collagen gels.** A-D) Time-averaged properties for individual T cell blasts migrating in collagen are shown for cells treated with or without 2 μg/mL CCL21, namely velocity (A), maximum displacement (B), turning angle (C), and confinement ratio (D). Each cell was analyzed for a 15 min timecourse; 15 cells from each of 2 independent experiments were analyzed. *** indicates significant difference at $p < 0.0001$.

The same concentration of collagen was next infused into macroporous PEG gels. T cells in the resulting composite scaffolds exhibited increased motility compared to those in ICAM-1-coated scaffolds with the same (40 μm) void diameter (compare Figure 4-9 and Figure 4-18). For example, mean maximum displacements were increased by 50%. In this setting, we expected that lymphocyte displacement and migration parameters would be influenced by the inverse opal void size. Larger pore sizes give more space for cells to travel before encountering a wall that could halt their migration or reduce its circuit, while small throat pores on the order of cell size could prevent transit of cells through the portals entirely (throat pore diameter is ~ 25% of nominal pore diameter, see section 2.3.2). Indeed, when T cell migration was quantified for composite scaffolds formed using inverse opals with different void diameters, we found that T cell trafficking pore-to-pore within scaffolds increased as the void diameter increased (Figure 4-18).

Cells were rarely able to transit between voids in 20 μm scaffolds, exhibited moderate displacements in 40 μm scaffolds, and migrated avidly through 80 μm pore scaffolds. Cell tracks (Figure 4-18, A and B) show this phenomenon qualitatively. While paths in the 80 μm scaffold were rarely obstructed, circular paths were evident in the 40 μm scaffolds, where it appears as though cells were being guided by contact with the PEG gel pore walls. Scaffolds with 80 μm void diameters were statistically identical to collagen alone as a substrate for cell migration in terms of cells' maximum displacement and confinement ratios (Figure 4-18, C-F), and ranges of values were similar for all parameters but turning angle, in which there was clearly a confined population in the 80 μm scaffold that was absent in pure collagen, with angles > 90°. Interestingly, migration in 40 μm scaffolds was statistically different from that in 80 μm scaffolds ($p < 0.05$) for all parameters except velocity. This suggests that just as vigorously moving cells can nevertheless be differentially confined by the surrounding architecture.

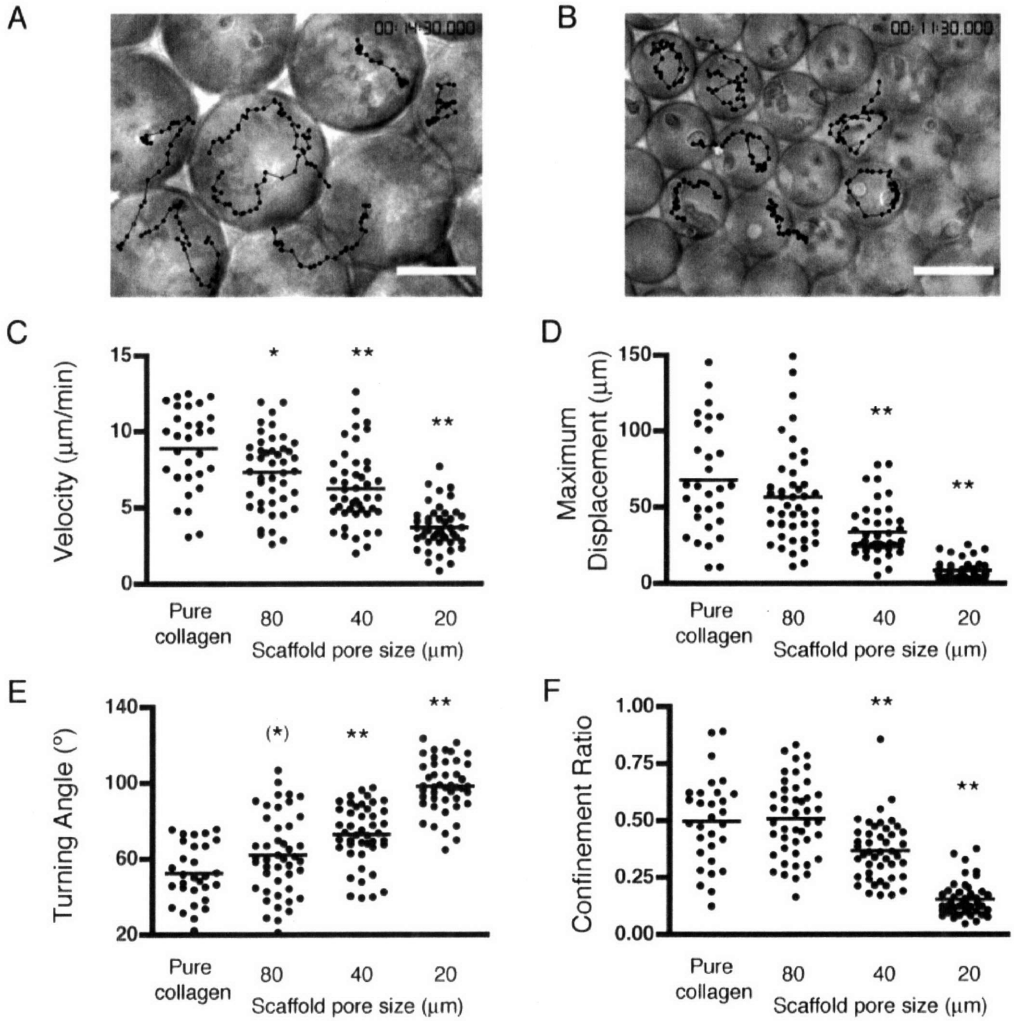

Figure 4-18 **T cell migration in composite scaffolds is robust and is affected by pore size.** A-B) Stills demonstrate migration paths of several T cells (in false color) in scaffolds with a main pore diameter of 80 μm (A) or 40 μm (B). C-F) Time-averaged properties for individual T cells are shown as a function of scaffold pore size (20, 40, or 80 μm) and in pure collagen. Shown are velocity (C, μm/min), maximum displacement (D, μm), turning angle (E, degree), and

confinement ratio (F, ratio of end displacement to total distance traveled). Each cell was analyzed for a 15 min timecourse; 15 cells from each of 2 (collagen) or 3 (scaffold) independent experiments were analyzed. Significant differences compared to collagen alone are indicated (** $p < 0.01$ by Dunnett and Bonferroni, * $p < 0.05$ by both tests, (*) $p < 0.05$ by Dunnett but > 0.05 by Bonferroni). Scale bars 24 μm.

In order to determine to what extent cell migration was random under the different conditions, we examined mean displacements for individual cells, plotted as a function of the square root of elapsed time. A linear relationship between mean displacement and root time indicates random cell migration, whereas a linear region followed by a plateau indicates confined migration, and a linear region followed by positive curvature indicates directed migration such as chemotaxis (39). (Note that the linear region is usually preceded by a brief non-linear regime due to the initial persistance of a cell in a given direction). The slope of the linear region indicates the relative motility of a given cell, with a motility coefficient defined analogously to a diffusion coefficient (slope^2/4 for migration in two dimensions). As shown in Figure 4-19A, most cells migrating in pure collagen moved randomly and exhibited a range of motility coefficients (i.e., slopes), but a few non-motile or circling cells were apparent (as curves with plateaus or dips). Cells behaved similarly in composite scaffolds with an 80 μm pore size (plots were mostly linear or with slight plateaus), and motility coefficients were statistically identical to the case of pure collagen (see Figure 4-19B and D). In agreement with the previous data analyses, in composite scaffolds with 40 μm pores (Figure 4-19C) many cell migration plots exhibited plateaus or dips, and cell motility coefficients were significantly lower. Thus, as scaffold pore size increased, cell migration became less obstructed and was primarily Brownian.

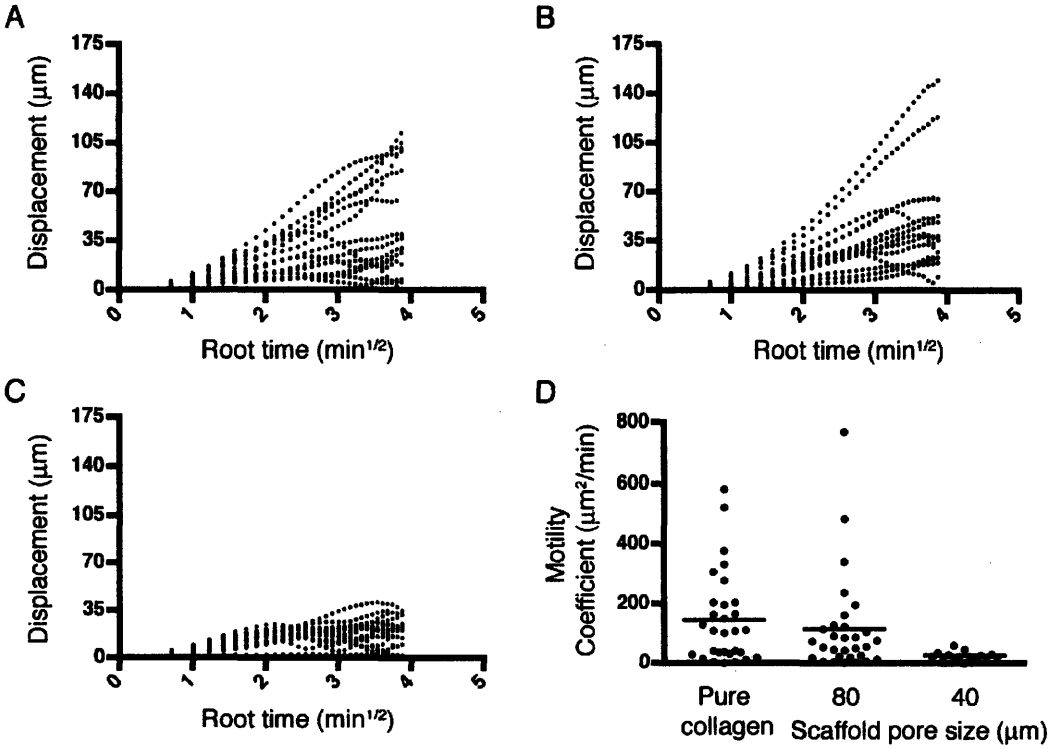

Figure 4-19 **T cell migration is largely random in composite scaffolds with high pore size.** (A-C) Mean displacement plots are shown for cells moving in pure collagen (A), in composite

scaffolds with 80 μm pores (B), and in composite scaffolds with 40 μm pores (C). One representative experiment (15 cells) is shown per condition. (D) Motility coefficients extracted from mean displacement plots are shown for the three cases. Data was analyzed from two representative experiments (30 cells) for the pure collagen and 80 μm conditions, and from one experiment for the 40 μm condition.

4.3.4.3 Full-thickness cell loading in composite scaffolds

While carrying out the migration studies just described, we discovered that cell loading in the composite collagen-infused structures appeared to be enhanced relative to loading of cells in inverse opal scaffolds that had been coated with adhesion proteins. Although observation of the outermost layers of gels by microscopy indicated that high cell density could be achieved in large areas of both protein-conjugated inverse opal gels and inverse opal-collagen composite gels, collagen-infused scaffolds were more uniformly filled with cells. We examined the extent of T cell loading in 3D by confocal imaging of thin sections cut through 1 mm-thick inverse opal-collagen composite scaffolds with 80 μm void diameters. This revealed T cell loading throughout the 1.2 mm thick scaffold cross-section (Figure 4-20). Similar experiments with mature dendritic cells showed that these larger cells could also be fully loaded through a scaffold with 80 μm pores as well. Figure 4-21 shows the center portions of two separate scaffold cross-sections, both of which have several DC clusters present. (This is clear in the brightfield images, although fixed DCs did not retain fluorescent dye well.) Both scaffolds also are brightly labeled with streptavidin all the way through, providing further confirmation of uniform protein conjugation throughout the scaffolds. In therapeutic strategies utilizing cells pre-loaded into scaffolds, full-thickness loading of cells, as well as full penetration of any delivered protein solutions, would be desirable for rapid and complete tissue formation.

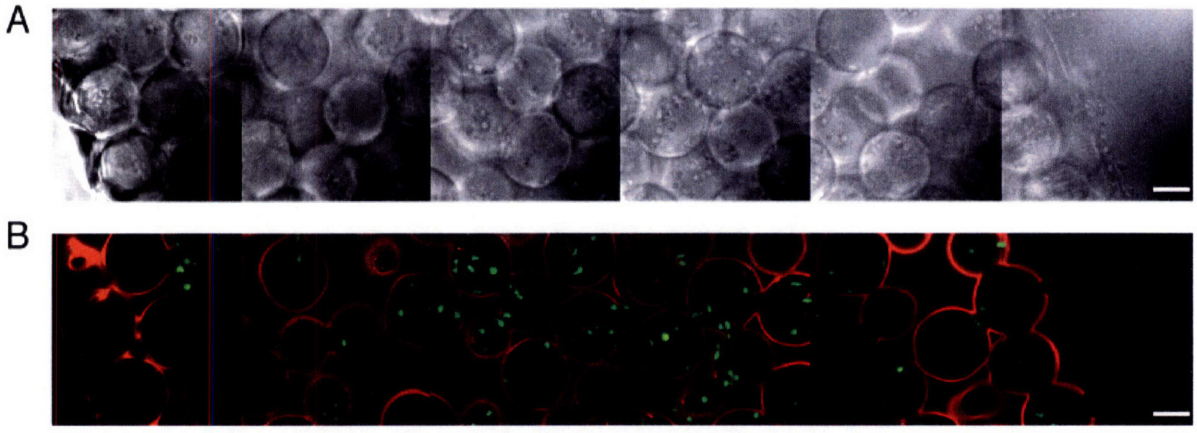

Figure 4-20 **Full-thickness loading of T cells in inverse opal-collagen composite scaffolds.** T cells suspended in collagen were infused into an 80 μm void diameter biotinylated PEG inverse opal scaffold. Cells were labeled with CMFDA to aid visualization by fluorescence, and the scaffold surfaces were visualized by coating with Alexa 647-conjugated streptavidin. Thin sections through the entire 1.2 mm-thick scaffold were cut and imaged en face by (A) brightfield and (B) confocal fluorescence microscopy. T cells are green and streptavidin red in the fluorescence overlay. Scale bars 41 μm.

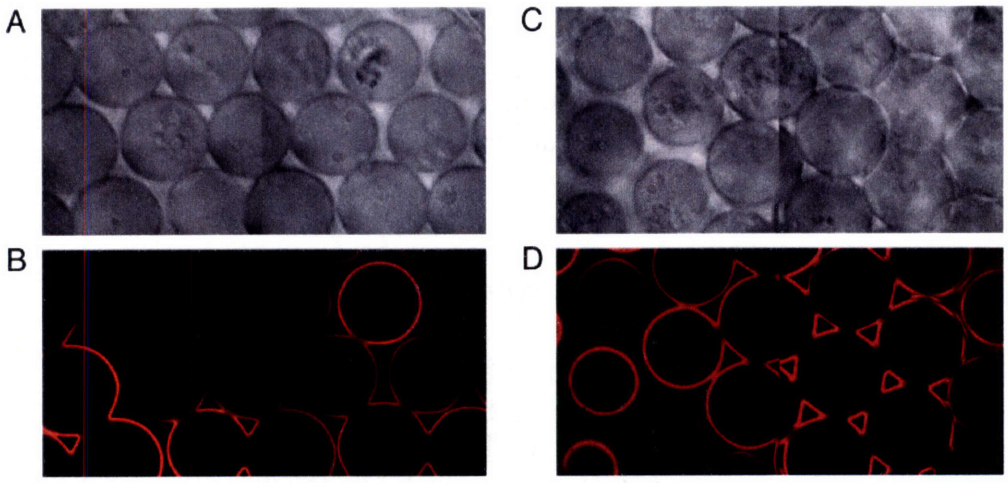

Figure 4-21 **Full-thickness loading of DCs in inverse opal-collagen composite scaffolds.** Dendritic cells suspended in collagen were infused into an 80 μm void diameter biotinylated PEG inverse opal scaffold. Cells were labeled with CMFDA (green) to aid visualization by fluorescence, and the scaffold surfaces were visualized by coating with Alexa 647-conjugated streptavidin (red). Thin sections through the entire 1.2 mm-thick scaffold were cut and imaged en face by (A, C) brightfield and (B, D) confocal fluorescence microscopy.

4.3.4.4 Dendritic cell behavior in composite scaffolds

We next investigated whether our inverse opal-collagen composite scaffolds could support migration of DCs, because of their importance in the immune response. DCs were loaded in composite scaffolds similarly to T cells and observed in time-lapse. Heterogeneous behavior was observed under the conditions tested, with some DCs migrating, others appearing to attach to the PEG scaffold walls, and yet others remaining relatively stationary in collagen away from the polymer scaffold walls. Much dendrite activity was seen in these LPS-matured cells. Migratory cells readily moved through pores in scaffolds with void sizes as small as 40 μm (10 μm throat pores), as shown in Figure 4-22. Thus, DCs can also traverse pores of the matrix to enter the gel or interact with T cells.

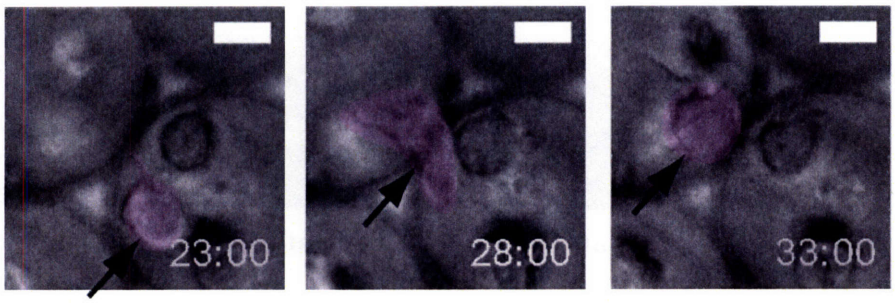

Figure 4-22 **Migration of dendritic cells pore-to-pore in inverse opal-collagen composite scaffolds.** Time-lapse brightfield images illustrate a dendritic cell (marked in false color) moving through a throat pore between voids in a 40 μm void size inverse opal-collagen composite scaffold. Scale bars 10 μm. Times shown are elapsed min:sec.

4.3.4.5 Lymphoid fibroblasts form networks in composite scaffolds

We tested this final iteration of artificial lymphoid constructs for their ability to support the formation of stromal cell networks. We again found that fibroblastic reticular cells from the BLS4 cell line could form networks in the scaffolds by extending processes through the scaffold throat pores. Uniformity of cell density was somewhat harder to control than for T cells, due to the fact that BLS4 stick to each other in culture even after brief trypsinization. Extended EDTA treatment can be used to separate individual cells better, but if done for too long then viability can suffer. However, parts of the cell networks were viable for at least four days, and networking behavior was observed in both 80 and 40 μm void size scaffolds (see Figure 4-23).

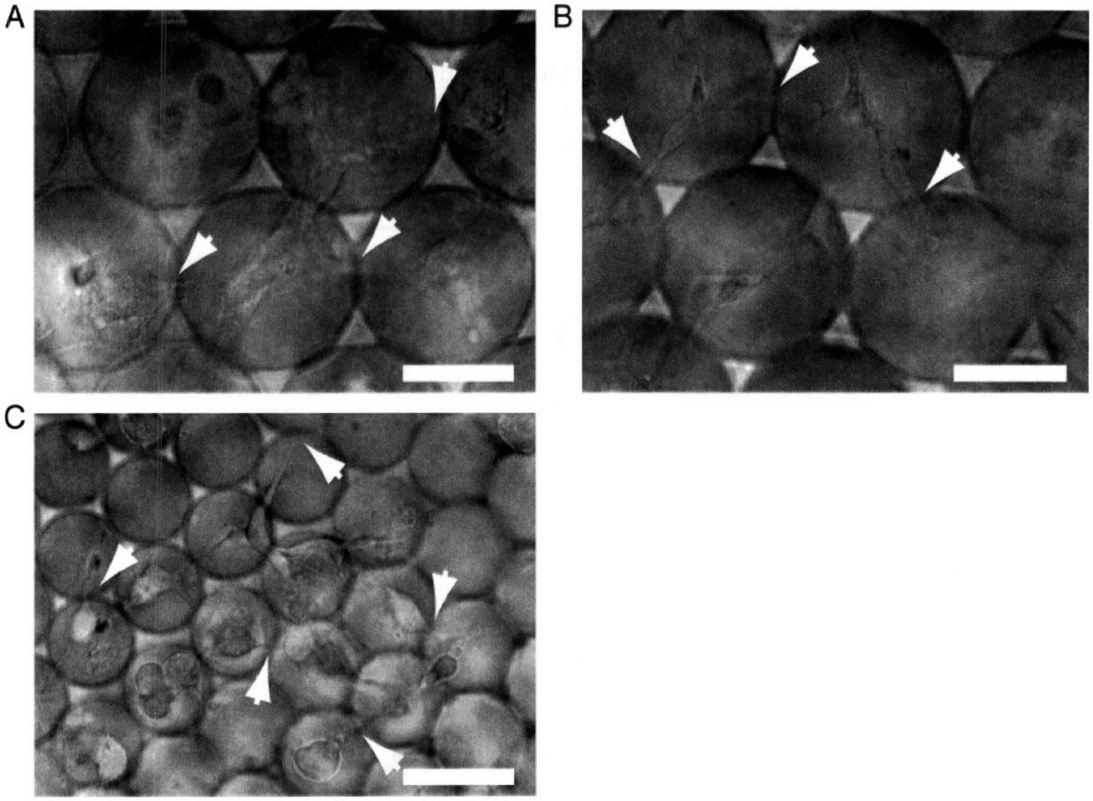

Figure 4-23 **Lymphoid fibroblasts form networks in composite scaffolds.** (A-C) are brightfield images with 50 μm scale bars. Arrows indicate cell spreading through throat pores. (A) BLS4 networks formed in composite scaffolds with an 80 μm void size by 22 hours. (B) Portions of the network remained viable for up to 4 days. (C) 40 μm scaffolds infused with collagen also were able to support some degree of BLS4 network formation (shown at 11 h).

4.3.5 Providing CCL21 chemokine directly from composite scaffolds

As discussed in section 1.1.3 and Chapter 3, the chemokine CCL21 provides critical signals for chemoattraction of lymphocytes and DCs to specific tissue sites (21, 38, 211, 212) and also

supports random migration of T cells in the absence of specific gradients (158, 196). While our studies show a useful role for this chemokine in supporting cell migration within PEG-collagen composite gels, soluble CCL21 added to the scaffold would be expected to rapidly diffuse away *in vivo*. In order to support both chemotaxis of host cells into the structure and chemokinesis of cells interacting within the scaffold, we anticipate that sustained delivery of CCL21 would be desirable. To this end, we tested a strategy for reversibly binding CCL21 to the surfaces of inverse opal PEG gels, in order to provide a depot that would sustain levels of chemokine in the composite scaffold over an extended time period.

To mimic the native interaction between basic chemokines such as CCL21 and polysacharrides such as heparin (see Figure 4-24), we exploited the biotin functional groups in the inverse opal scaffolds to bind biotinylated heparin to the scaffold surfaces via a streptavidin bridge. The heparin could in turn bind CCL21. Successful binding of biotinylated heparin to streptavidin-coated inverse opal PEG gels was indirectly confirmed by staining of gels with the cationic dye Toluidene blue (see Figure 4-25). Although non-heparinized scaffolds were faintly stained due to the free carboxyl groups in the biotin-lysine, only scaffolds that were sequentially incubated in both streptavidin and biotin-heparin were stained dark blue-purple.

Figure 4-24 **Schematic of heparin-chemokine interaction.** Adapted from (213). A fragment of heparin (circled) is shown using a ball-and-stick model, and the chemokine (CXCL12) is shown using a ribbon diagram. The type and positions of basic residues on the protein that interact directly with acidic groups on the heparin are indicated.

Figure 4-25 **Biotinylated heparin binds to streptavidin-coated scaffolds.** Scaffolds were stained with the cationic dye Toluidene blue to detect bound anionic heparin. While scaffolds incubated only with streptavidin (A) or only with biotin-heparin (B) stained faint blue, scaffolds that received both treatments (C) became a deep purple color.

To confirm that heparin-modified PEG gels would bind CCL21, scaffolds were incubated with chemokine, washed for 24 h, and then immunostained with anti-CCL21 and secondary fluorescent antibodies. Punctate spots of chemokine were clearly visible on the scaffold surfaces via confocal microscopy (Figure 4-26), while a control scaffold that received no chemokine was completely free of background staining (data not shown). Because CCL21 binding to heparin is reversible (with a dissociation constant K_D of ~5 nM for the human protein, (112)), we expected that scaffold-bound chemokine would become available to cells loaded in composite scaffolds over time. To test the functionality of chemokine loaded on the PEG gel surfaces of inverse opal-collagen composite scaffolds, we assayed the motility of naïve $CD4^+$ T cells loaded into composite scaffolds with or without surface-bound CCL21. As discussed in Chapter 3, naïve T cells have low basal motility; they have almost no motility in collagen in the absence of CCL21 under the conditions that we use. Thus, their motility provides a sensitive *in situ* assay for the presence of chemokine. Scaffolds loaded with chemokine were thoroughly washed (12x in 4 h) to rid free CCL21 and then loaded with cells suspended in collagen. Within 0.5 h, a fraction of the naïve T cells became motile in CCL21-loaded scaffolds, while none did in the control sample; this difference became more pronounced with time. We quantified cell migration at 5-6 h, as shown in Figure 4-26B-D; a fraction of the T cells were highly migratory in CCL21-loaded scaffolds, while essentially zero motility was observed in controls.

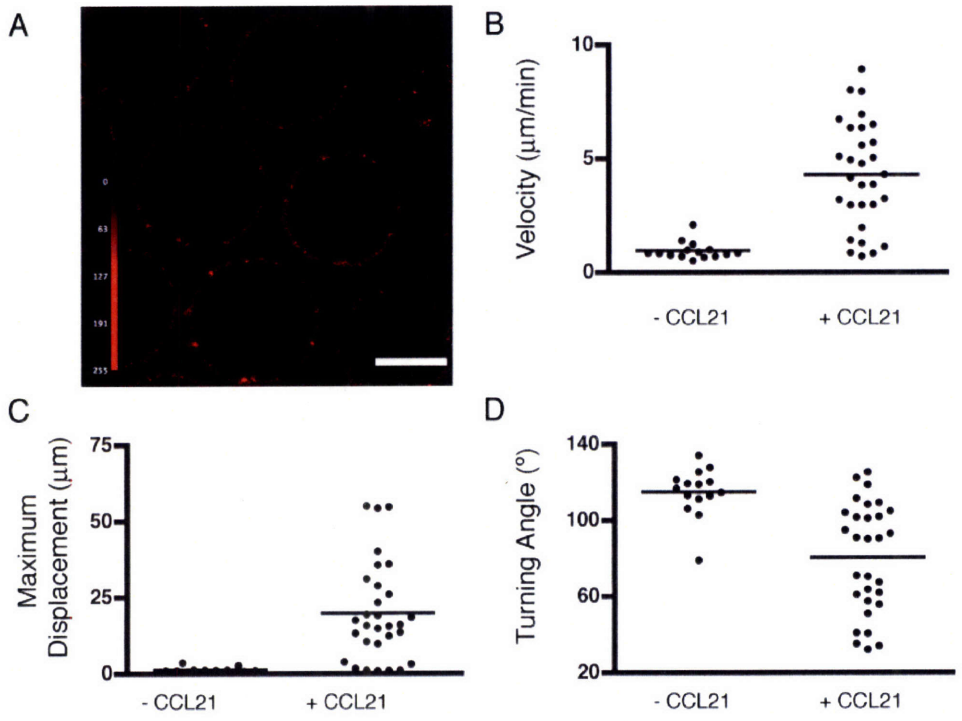

Figure 4-26 **Chemokine released from scaffolds remains functional.** (A) Immunofluorescence staining of CCL21 in an 80 μm void size scaffold. B-D) Time-averaged properties for individual naïve T cells migrating in composite scaffolds with or without heparin-immobilized CCL21 are shown, namely velocity (B), maximum displacement (C), and turning angle (D). Each cell was analyzed for a 10 min time course; 15 cells from each of 1 (control) or 2 (chemokine) independent experiments were analyzed. *** indicates significant difference at $p < 0.0001$.

These results suggest that the inverse opal gel can serve not only to provide mechanical support for the infused collagen matrix, but also act as a chemokine-binding depot to sustain the delivery of chemokines or other cytokines relevant to promoting a lymphoid tissue-like microenvironment.

4.4 Discussion

Boosting the adaptive immune response is a major goal of immunotherapy, particularly for the treatment of cancer (57). Thus far such therapies have primarily focused on the injection of cells or cytokines to increase infiltration of adaptive immune cells (or their activation) at tumor sites. Cytokine therapies have the disadvantage of requiring repeated dosing, while direct injections of cells without control over their microenvironment may cause inefficient or incomplete induction of immune responses. As an alternative approach, two strategies can be envisioned for using a synthetic scaffold to drive the local accumulation of adaptive immune cells involved in T cell priming. In an 'adoptive transfer' strategy, autologous T cells and dendritic cells could be isolated from peripheral blood or derived from peripheral blood monocytes, respectively (193). These cells could then be loaded *ex vivo* into scaffolds for implantation at a tumor site (e.g., during solid tumor resection), or alternatively, at a site well removed from the immunosuppressive tumor microenvironment. In an '*in vivo* assembly' strategy, scaffolds loaded with chemoattractants normally present in secondary lymphoid organs would chemoattract naïve lymphocytes and DCs from the local blood supply. Attracting rather than merely injecting DCs may be particularly important, as the presence of native DC at the tumor site improves tumor eradication even when utilizing cancer vaccines with transferred cells (214). While the second approach likely represents a greater technical challenge, it would of course simplify clinical application.

Here we have described the development and *in vitro* testing of a scaffold that could support either strategy of lymphoid or lymphoid-like tissue induction. In Chapter 2, we showed that an inverse opal structure allows gels with highly interconnected pores to be formed without the extreme deterioration in mechanical properties typical of random porogen methods, which require very high degrees of total porosity to achieve high interconnectivity of pores (194). Thus, in the inverse opal-collagen composite strategy examined here, the macroporous PEG structure provides mechanical support and ease of handling for implantation, while the softer collagen matrix within the pores supports rapid T cell migration. As shown in Figure 4-26, the scaffold can also act as a platform to depot chemokine for stimulating immune cell chemotaxis and chemokinesis.

We initially tested the feasibility of using a macroporous PEG scaffold modified at its surfaces with adhesion ligands (rather than infused with a collagen gel) as a support for cell migration. We compared scaffolds coated with ICAM-1 and fibronectin, two ligands present in secondary lymphoid organs. Although scaffolds presenting the key integrin ligand ICAM-1 significantly increased T cell velocity and displacement compared to scaffolds lacking protein, only a fraction of T cells rapidly migrated, and even those were not as motile as cells that have been observed *in vivo*. Meanwhile, the peptide RGD and whole fibronectin had no effect on T cell motility at all. These results may have been due to a variety of factors, including low T cell integrin expression, insufficient density of T cell packing in the scaffolds, inappropriate stiffness

of the substrate, or simply too low ligand density. We recognized that we would have to modify, perhaps radically, our approach to attaining rapid T cell migration *in vitro*. However, first we examined two other cell types of interest – DCs and FRCs – for insight as to how these protein-coated scaffolds were functioning.

The critical partner involved in triggering T cell mediated immune responses is the dendritic cell, a professional antigen presenting cell which activates and differentiates T cells into effector or memory cells capable of directly or indirectly attacking tumors and infected cells. DCs also likely play an interactive role in lymphoid tissue development through various feedback mechanisms in concert with T cells (36, 215, 216), making their presence important for the potential development of lymphoid neotissues. We found that dendritic cells cultured alone in scaffolds were able to spread and crawl on scaffold surfaces coated with fibronectin and/or laminin. Interestingly, in the presence of DCs and fibronectin, we saw that a fraction of T cells could migrate along the DC bodies about as well as on ICAM-1-coated scaffolds (see Table 4-1). However, even if this migration could be optimized (e.g., by changing relative cell ratios), we are potentially interested in co-attracting and co-infiltrating these cells into the scaffold, rather than relying on the infiltration of DCs first, followed by T cells. This may be an unlikely order of events *in vivo*, as evidenced by studies comparing the effects of ectopic expression of CCL21 in RAG-/- mice (which lack mature T and B cells) versus wild-type mice. In wild-type mice, DCs are recruited to the ectopic site of chemokine release, but this does not occur in RAG knockout mice, indicating a co-requisite role for T cells (36). Sequential cell addition *in vitro* might be more feasible than sequential attraction *in vivo*, but only if consistent conditions for DC spreading along the scaffold (rather than filling the pores) can be determined; otherwise it may be difficult to load T cells uniformly throughout the structure, due to pore blockage by DCs.

To complete our studies in protein-coated scaffolds, we observed the behavior of stromal fibroblasts in these structures, and found that they spread and connected to form intricate 3D networks. Unlike the case of DC networks, the presence of fibroblasts did not appear to influence T cell migration favorably (nor unfavorably). Thus, we found that varying the type of adhesion ligand presented on the scaffold or adding accessory cells affected T cell migration in only a minimal fashion in these inverse opal structures. Although there was a vast potential parameter space to explore in these factors alone (ligand concentration, cell density and ratios, etc.), we were concerned about heterogeneity of parameter values across the scaffold and thus reproducibility of experiments. Because relatively uniform T cell mobility is critical for antigen surveillance, we looked for alternative means to promote T cell migration within these structures.

Prior studies by Friedl et al. have shown that T cells migrate in collagen gels by an integrin-independent 'amoeboid' mechanism (200). This prompted us to test the infusion of inverse opal structures with collagen. In the presence of soluble CCL21, T cell migration in neat collagen gels quantitatively approached behavior recorded *in vivo*, including an average velocity of ~ 9 μm/min (10-11 μm/min in vivo (116, 207)), an average turning angle of 53° (63° in vivo(207)), and an average confinement ratio of 0.50 (0.56 *in vivo* (207), 0.48 for $CD8^+$ T cells (217)). Similar values (8-9 μm/min velocity) were also obtained by Gunzer et al. for T cells co-cultured for 2 days in collagen with dendritic cells (202), which are known to secrete a number of chemokines active on T cells (192).

In collagen-infused composite scaffolds, T cell migration was improved compared to protein-coated scaffolds, and was dependent on the pore size of the inverse opal polymer structure. The increased migration response reflected the ability of the cells to move effectively throughout the 3D voidspace of the PEG gels supported by the collagen fiber network, without requiring contact

with the PEG gel walls to adhere and migrate. Cell migration was enhanced at larger pore sizes, and for inverse opal structures with 80 μm void diameters, T cells were able to travel almost as freely as in neat collagen gels. Notably, because the modulus of porous materials scales with porosity, and porosity is equivalent in the inverse opal structures regardless of void diameters, the mechanical properties of the inverse opal gels are not decreased by increasing the void diameters (194, 218).

Due to the increased viscosity of collagen compared to culture medium, cell loading and retention for both T cells and dendritic cells was excellent in composite scaffolds, particularly in the very open 80 μm structures. Such full-thickness loading would be key for a therapeutic approach in which cells are expanded/activated *ex vivo* and then transferred back to a patient in scaffolds to drive an immune response. Others have used alginate or collagen-infused composite polymeric scaffolds to similarly achieve good cell retention and suitable mechanical properties in the same construct (219, 220).

As we had done for the protein-coated scaffolds, we tested DC and stromal fibroblast behavior in the composite scaffolds as well. Fewer DCs were associated with the walls of the inverse opal in the composite than in the protein-coated scaffolds, due to the presence of an adhesive substrate (collagen) within the pores as well. DCs are known to migrate through collagen, and we found that DCs in our composite structures could readily move through the collagen across PEG-outlined throat pores as small as 10 μm (void size 40 μm). Stromal fibroblasts of the BLS4 cell line were able to form networks in the collagen-infused structures as they did in the protein-coated scaffolds. Thus, we developed a scaffold that supported DC and rapid T cell migration, and could potentially be used in concert with stromal cells as well.

Finally, we tested a strategy for binding chemokine to the PEG surfaces of the composite scaffolds, to provide a chemokine depot that might support both chemotaxis of host cells into the structure and chemokinesis of cells interacting within the scaffold. We focused on the chemokine CCL21, which provides critical signals for immune cell homing to secondary lymphoid organs (21, 211) and also supports random migration of T cells in the absence of specific gradients (158, 196). Various methods have been used to incorporate growth factors and other biological signaling molecules in tissue engineering scaffolds (see section 1.3.4, (97)). One promising strategy for retaining long-term release and functionality is the use of heparin, which binds many cytokines. Heparin has been covalently attached to PEG scaffolds via methacrylation (104), to PLGA scaffolds (105) via carbodiimide chemistry, and by noncovalent interactions with PEG networks (106, 107); it has typically been used to release cytokines such as basic fibroblast growth factor (104-106). In our system we used biotin-streptavidin non-covalent interactions to attach heparin to PEG scaffolds. Heparin-conjugated scaffolds bound CCL21, and the functional release of this factor in composite scaffolds was demonstrated by the induction of naïve T cell motility within the composite gel. Future studies will be required to determine the limits to the amount of chemokine that can be delivered in this manner and whether slow release of chemokine from inverse opal surfaces can drive chemotaxis of lymphocytes or dendritic cells from the local bloodstream to enter the scaffold structure.

In conclusion, we have demonstrated a composite inverse opal-collagen hydrogel as a scaffold that can support the loading and robust migration of immune cells, as a first step toward *in vivo* engineering of T cell-mediated immune responses within a supporting synthetic microenvironment. For these *in vitro* studies we used nondegradable PEG gels; however, this system is readily modified to incorporate enzyme-sensitive peptides to tailor degradability (76). As stated previously, the poly(ethylene glycol) inverse opal component of this composite

provides mechanical support and sites to deliver supporting factors such as chemokines or other cytokines, while the infused fibrillar collagen provides a matrix for rapid lymphocyte motility. This general approach may be broadly useful as a strategy to combine the favorable properties of synthetic and biopolymeric hydrogels and allow each component to compensate for deficiencies in the properties of its partner.

5 Summary and Future Considerations

In this work, we designed, fabricated, and tested a novel macroporous hydrogel scaffold for lymphoid tissue engineering applications. Such a scaffold could be used for *in vitro* investigation of factors that modulate immune cell behaviors such as motility, and potentially developed as a construct for cancer immunotherapy. The *de novo* formation of lymphoid tissue at tumor sites has been shown to treat cancer in several animal models; previous research has utilized cytokine injection or antibody targeting of cytokines to tumors to attract immune cells and induce tissue formation (52-55). We propose that an implantable scaffold providing signals supportive of immune cell motility and lymphoid organ development could be used to induce lymphoid tissue formation at tumor sites, with distinct advantages over previous systems. First, a site-specific controlled release system for cytokines would be preferable to systemic injections, due to the frequency and potential toxicity of the latter method. Further, providing a defined space for cell interactions and neotissue development would likely promote more efficient immune cell compartmentalization and subsequent interactions than an injection of cytokines and/or cells alone. As a first step in development of a scaffold system suitable for clinical use, we performed *in vitro* studies of cell behavior in several iterations of scaffolds.

We were particularly interested in examining the migratory response of T cells in scaffold microenvironments with different architectures and biochemical signal presentation. Due to the low frequency of naïve T cells specific for any given antigen, their rapid, unobstructed migration is important for their ability to contact DCs bearing cognate antigen, which will initiate an immune response. We thus studied how different adhesion proteins, chemokines, underlying materials and pore sizes affected T cell migration. These studies were undertaken both to explore motility signals in a fundamental way, and in order to design a construct that could potentially be used for immunotherapy. The final design for this lymphoid scaffold was a PEG hydrogel with hexagonally close-packed arrays of interconnected pores (an 'inverse opal'), infused with a fibrillar collagen gel. The macroporous PEG provided relative mechanical stability (both compared to collagen and compared to scaffolds created with stochastic rather than ordered porogen methods), while the collagen provided a favorable matrix for T cell migration. Although smaller pores sizes physically constricted T cell migration paths, when an 80 μm pore size was used for the inverse opal, T cell migration was nearly identical to that in pure collagen. We also developed a preliminary method to deliver the chemokine CCL21 (which induces motility in several immune cell sub-sets, and also influences lymphoid organ development) from the surface of the PEG gel, for the purpose of attracting, organizing, and maintaining the motility of immune cells. In surface studies performed outside scaffolds, we showed that the chemokine CCL21 can promote T cell chemokinesis, i.e., motility in the absence of a concentration gradient. We then demonstrated that 3D scaffolds delivering CCL21 via surface-bound heparin could also induce naïve T cell chemokinesis within composite scaffolds. In the future, the maintenance and scale of CCL21 chemotaxis activity should also be demonstrated in the scaffolds, by attracting T cells and dendritic cells from a nearby chemokine-free tissue mimic such as collagen gel.

In early studies, we found that PEG gels coated with peptides or even whole adhesion proteins (in the absence of interstitial collagen gel) were not suitable as a microenvironment for T cell migration. The only protein we tested that was able to support any migration was ICAM-1, but it only did so for about 30% of cells, with an average velocity about ~30% lower than that seen *in vivo*. Cells were easily bumped off the walls by the movement of nearby cells or

convective currents in the medium. It is possible that if cells were packed to very high density in scaffolds (similarly to their dense packing in native secondary lymphoid organs) with pore diameters on the order of cell size, then the high surface area of protein might support cell migration, with a minimal effect of convection even in the absence of a collagen gel. However, scaffolds with small pores (e.g., 20 μm, with throat pores on the order of cell size at 5 μm) are by nature more difficult to load uniformly and to a high density with cells. One possibility for the future is to create thermoresponsive hydrogel scaffolds using polymers such as NIPAM (N-isopropylacrylamide). These could be loaded with cells at 4 °C in a large pore state, then transferred to 37 °C to shrink the pores around the cells. Initial experiments in our lab have shown that at least a 20-30% decrease in gel size is possible.

Another materials parameter worth exploring is the composition of the interstitial gel. Alginate, hyaluronic acid, fibrin, or the basement-membrane extract Matrigel™ might be biopolymers worth testing as alternatives to collagen. An ideal gel would not only support cell migration, but might also interact with CCL21 so as to slow but not completely halt its diffusion out of the scaffold. This may be one way to lengthen the time for CCL21 release, as long-term release may be needed to attract enough relevant immune cells in clinical application.

Besides experimentation with the biopolymer component as a diffusion barrier, further work should in general be performed to improve the chemokine delivery system and test its limits. Having already developed a method using biotin-streptavidin interactions for attachment of arbitrary adhesion proteins, we used this same method for attachment of biotinylated heparin, which was subsequently used to sequester chemokines. Noncovalent binding strategies are attractive because they do not require any (potentially destructive) modification of the attached protein. However, it may be more efficient to attach heparin to the scaffold in one rather than two steps, perhaps by including heparin-binding peptides in the PEG matrix as some other researchers have done (106, 108). The additional protection and de-protection steps necessitated by the lysine groups in the peptide might render this method ultimately labor-equivalent, however. It is also possible that loading chemokine-containing microspheres into scaffolds may be preferable to surface attachment, for two reasons. One is that the amount of chemokine loading would be more readily controlled by this method, simply by changing the number of microspheres added. Ultimately there would be a limit to the amount of chemokine that could be added, if the microspheres interfered with cell interactions within the structure. However, whereas with surface attachment there may be a need to saturate one porous layer of the polymer before the chemokine can diffuse further into the scaffold, this is not a concern with a microsphere system. Even more importantly, unlike with the multiple incubation steps required for our surface attachment method, microspheres could be quickly prepared and used to add chemokine just before use of the scaffold (or better still, lyophilized and stored for a period of months), allowing more flexibility in preparation. Clinically, this would seem to be the most feasible method. One other interesting approach might be to isolate CCL21-producing cells in polymer microspheres or vesicles that cannot be penetrated by large immune complexes, but that do let nutrients and small proteins such as chemokines pass. This would allow for unlimited production of CCL21, while avoiding some of the risks of using transfected cells that directly contact the blood or tissues.

As described above for the chemokine delivery aspect, but also more generally, the system that we designed requires perhaps an overly complex and time-consuming process. Initially we were interested in mimicking the lymph node T zone to as great a degree as possible. However, our many-step process suffers from reproducibility issues, while still not approaching the

complexity of the real biological system. Now that we are focused on a goal of immunotherapy, a simpler system could perhaps be designed. For example, an injectable rather than implantable polymer may be preferable in such a case, due to the gain in clinical simplicity. Cells and chemokines could both be readily suspended in such gels. However, chemokine may be depleted more quickly using this simple mixing (versus attachment) strategy, even if free heparin is also included to maintain chemokine activity. Further, if a natural gel such as collagen were used alone, we would lose the improvements in construct mechanical properties provided by the polymer, and its degradation rate *in vivo* would not be readily tunable. Alternatively, if a synthetic polymer were used alone as a bulk gel, it is not clear that T cell migration would be possible (unless the polymer had a collagen-like nanofibrous structure), and the diffusion and nutrient access provided by the porous structure would be lost. These trade-offs between complex composite versus simple gels can best be addressed by performing *in vivo* experiments to observe cell attraction to and organization within scaffolds/gels in treated animals. At this stage, the rate of material degradation will become important as well, as successful tissue engineering often requires a degradable material. Photopolymerized PEG gels can be made degradable by the inclusion of enzyme-sensitive cross-links (76), and preliminary studies in our lab have confirmed that these remain active after acetic acid treatment.

In summary, our *in vitro* studies thus far have revealed roles for adhesion proteins, cell composition, chemokines, and architecture in influencing T cell migration within 3D artificial structures. Such basic studies could be continued further, in concert with improvements to the scaffold as described above. The introduction of degradability, optimization of the chemokine delivery system, and simplifying the fabrication process could result in a clinically useful device.

REFERENCES

1. Abbas, A. K., and A. H. Lichtman. 2005. *Cellular and Molecular Immunology*. Elsevier Saunders, New York.
2. Gretz, J. E., A. O. Anderson, and S. Shaw. 1997. Cords, channels, corridors and conduits: critical architectural elements facilitating cell interactions in the lymph node cortex. *Immunol. Rev. 156:11-24.*
3. Katakai, T., T. Hara, J. H. Lee, H. Gonda, M. Sugai, and A. Shimizu. 2004. A novel reticular stromal structure in lymph node cortex: an immuno-platform for interactions among dendritic cells, T cells and B cells. *International Immunology 16:1133-1142.*
4. Bajenoff, M., J. G. Egen, L. Y. Koo, J. P. Laugier, F. Brau, N. Glaichenhaus, and R. N. Germain. 2006. Stromal cell networks regulate lymphocyte entry, migration, and territoriality in lymph nodes. *Immunity 25:989-1001.*
5. Sixt, M., N. Kanazawa, M. Selg, T. Samson, G. Roos, D. P. Reinhardt, R. Pabst, M. B. Lutz, and L. Sorokin. 2005. The conduit system transports soluble antigens from the afferent lymph to resident dendritic cells in the T cell area of the lymph node. *Immunity 22:19-29.*
6. Lindquist, R. L., G. Shakhar, D. Dudziak, H. Wardemann, T. Eisenreich, M. L. Dustin, and M. C. Nussenzweig. 2004. Visualizing dendritic cell networks in vivo. *Nat Immunol 5:1243-1250.*
7. Hayakawa, M., M. Kobayashi, and T. Hoshino. 1988. Direct contact between reticular fibers and migratory cells in the paracortex of mouse lymph nodes: a morphological and quantitative study. *Arch Histol Cytol 51:233-240.*
8. Fugmann, S. D., A. I. Lee, P. E. Shockett, I. J. Villey, and D. G. Schatz. 2000. The RAG proteins and V(D)J recombination: complexes, ends, and transposition. *Annu Rev Immunol 18:495-527.*
9. von Andrian, U. H., and C. R. Mackay. 2000. T-cell function and migration. Two sides of the same coin. *N Engl J Med 343:1020-1034.*
10. Bousso, P., and E. Robey. 2003. Dynamics of CD8+ T cell priming by dendritic cells in intact lymph nodes. *Nat Immunol 4:579-585.*
11. von Andrian, U. H., and T. R. Mempel. 2003. Homing and cellular traffic in lymph nodes. *Nat Rev Immunol 3:867-878.*
12. Marrack, P., and J. Kappler. 2004. Control of T cell viability. *Annu Rev Immunol 22:765-787.*
13. Banchereau, J., and R. M. Steinman. 1998. Dendritic cells and the control of immunity. *Nature 392:245-252.*
14. Zinkernagel, R. M. 1996. Immunology taught by viruses. *Science 271:173-178.*
15. Abbas, A. K., K. M. Murphy, and A. Sher. 1996. Functional diversity of helper T lymphocytes. *Nature 383:787-793.*
16. Kaech, S. M., E. J. Wherry, and R. Ahmed. 2002. Effector and memory T-cell differentiation: implications for vaccine development. *Nat Rev Immunol 2:251-262.*
17. Miller, M. J., A. S. Hejazi, S. H. Wei, M. D. Cahalan, and I. Parker. 2004. T cell repertoire scanning is promoted by dynamic dendritic cell behavior and random T cell motility in the lymph node. *Proc Natl Acad Sci U S A 101:998-1003.*

18. Cohen, M. C., and S. Cohen. 1996. Cytokine function: a study in biologic diversity. *Am J Clin Pathol 105:589-598.*
19. Cyster, J. G. 1999. Chemokines and cell migration in secondary lymphoid organs. *Science 286:2098-2102.*
20. Stein, J. V., and C. Nombela-Arrieta. 2005. Chemokine control of lymphocyte trafficking: a general overview. *Immunology 116:1-12.*
21. Gunn, M. D., K. Tangemann, C. Tam, J. G. Cyster, S. D. Rosen, and L. T. Williams. 1998. A chemokine expressed in lymphoid high endothelial venules promotes the adhesion and chemotaxis of naive T lymphocytes. *Proc Natl Acad Sci U S A 95:258-263.*
22. Legler, D. F., M. Loetscher, R. S. Roos, I. Clark-Lewis, M. Baggiolini, and B. Moser. 1998. B cell-attracting chemokine 1, a human CXC chemokine expressed in lymphoid tissues, selectively attracts B lymphocytes via BLR1/CXCR5. *J Exp Med 187:655-660.*
23. Reif, K., E. H. Ekland, L. Ohl, H. Nakano, M. Lipp, R. Forster, and J. G. Cyster. 2002. Balanced responsiveness to chemoattractants from adjacent zones determines B-cell position. *Nature 416:94-99.*
24. Luther, S. A., H. L. Tang, P. L. Hyman, A. G. Farr, and J. G. Cyster. 2000. Coexpression of the chemokines ELC and SLC by T zone stromal cells and deletion of the ELC gene in the plt/plt mouse. *Proc Natl Acad Sci U S A 97:12694-12699.*
25. Stein, J. V., A. Rot, Y. Luo, M. Narasimhaswamy, H. Nakano, M. D. Gunn, A. Matsuzawa, E. J. Quackenbush, M. E. Dorf, and U. H. von Andrian. 2000. The CC chemokine thymus-derived chemotactic agent 4 (TCA-4, secondary lymphoid tissue chemokine, 6Ckine, exodus-2) triggers lymphocyte function-associated antigen 1-mediated arrest of rolling T lymphocytes in peripheral lymph node high endothelial venules. *J Exp Med 191:61-76.*
26. Forster, R., A. Schubel, D. Breitfeld, E. Kremmer, I. Renner-Muller, E. Wolf, and M. Lipp. 1999. CCR7 coordinates the primary immune response by establishing functional microenvironments in secondary lymphoid organs. *Cell 99:23-33.*
27. Ansel, K. M., V. N. Ngo, P. L. Hyman, S. A. Luther, R. Forster, J. D. Sedgwick, J. L. Browning, M. Lipp, and J. G. Cyster. 2000. A chemokine-driven positive feedback loop organizes lymphoid follicles. *Nature 406:309-314.*
28. Alimzhanov, M. B., D. V. Kuprash, M. H. Kosco-Vilbois, A. Luz, R. L. Turetskaya, A. Tarakhovsky, K. Rajewsky, S. A. Nedospasov, and K. Pfeffer. 1997. Abnormal development of secondary lymphoid tissues in lymphotoxin beta-deficient mice. *Proc Natl Acad Sci U S A 94:9302-9307.*
29. Futterer, A., K. Mink, A. Luz, M. H. Kosco-Vilbois, and K. Pfeffer. 1998. The lymphotoxin beta receptor controls organogenesis and affinity maturation in peripheral lymphoid tissues. *Immunity 9:59-70.*
30. De Togni, P., J. Goellner, N. H. Ruddle, P. R. Streeter, A. Fick, S. Mariathasan, S. C. Smith, R. Carlson, L. P. Shornick, J. Strauss-Schoenberger, and et al. 1994. Abnormal development of peripheral lymphoid organs in mice deficient in lymphotoxin. *Science 264:703-707.*
31. Koni, P. A., R. Sacca, P. Lawton, J. L. Browning, N. H. Ruddle, and R. A. Flavell. 1997. Distinct roles in lymphoid organogenesis for lymphotoxins alpha and beta revealed in lymphotoxin beta-deficient mice. *Immunity 6:491-500.*
32. Honda, K., H. Nakano, H. Yoshida, S. Nishikawa, P. Rennert, K. Ikuta, M. Tamechika, K. Yamaguchi, T. Fukumoto, T. Chiba, and S. I. Nishikawa. 2001. Molecular basis for

hematopoietic/mesenchymal interaction during initiation of Peyer's patch organogenesis. *J Exp Med 193:621-630.*

33. Cupedo, T., G. Kraal, and R. E. Mebius. 2002. The role of CD45+CD4+CD3- cells in lymphoid organ development. *Immunol Rev 189:41-50.*
34. Luther, S. A., T. Lopez, W. Bai, D. Hanahan, and J. G. Cyster. 2000. BLC expression in pancreatic islets causes B cell recruitment and lymphotoxin-dependent lymphoid neogenesis. *Immunity 12:471-481.*
35. Sacca, R., C. A. Cuff, W. Lesslauer, and N. H. Ruddle. 1998. Differential activities of secreted lymphotoxin-alpha3 and membrane lymphotoxin-alpha1beta2 in lymphotoxin-induced inflammation: critical role of TNF receptor 1 signaling. *J Immunol 160:485-491.*
36. Fan, L., C. R. Reilly, Y. Luo, M. E. Dorf, and D. Lo. 2000. Cutting edge: ectopic expression of the chemokine TCA4/SLC is sufficient to trigger lymphoid neogenesis. *J Immunol 164:3955-3959.*
37. Chen, S. C., G. Vassileva, D. Kinsley, S. Holzmann, D. Manfra, M. T. Wiekowski, N. Romani, and S. A. Lira. 2002. Ectopic expression of the murine chemokines CCL21a and CCL21b induces the formation of lymph node-like structures in pancreas, but not skin, of transgenic mice. *J Immunol 168:1001-1008.*
38. Luther, S. A., A. Bidgol, D. C. Hargreaves, A. Schmidt, Y. Xu, J. Paniyadi, M. Matloubian, and J. G. Cyster. 2002. Differing activities of homeostatic chemokines CCL19, CCL21, and CXCL12 in lymphocyte and dendritic cell recruitment and lymphoid neogenesis. *J Immunol 169:424-433.*
39. Sumen, C., T. R. Mempel, I. B. Mazo, and U. H. von Andrian. 2004. Intravital microscopy: visualizing immunity in context. *Immunity 21:315-329.*
40. Zhang, L., J. R. Conejo-Garcia, D. Katsaros, P. A. Gimotty, M. Massobrio, G. Regnani, A. Makrigiannakis, H. Gray, K. Schlienger, M. N. Liebman, S. C. Rubin, and G. Coukos. 2003. Intratumoral T cells, recurrence, and survival in epithelial ovarian cancer. *N Engl J Med 348:203-213.*
41. Dunn, G. P., A. T. Bruce, H. Ikeda, L. J. Old, and R. D. Schreiber. 2002. Cancer immunoediting: from immunosurveillance to tumor escape. *Nat Immunol 3:991-998.*
42. Jemal, A., R. Siegel, E. Ward, T. Murray, J. Xu, C. Smigal, and M. J. Thun. 2006. Cancer statistics, 2006. *CA Cancer J Clin 56:106-130.*
43. Galon, J., A. Costes, F. Sanchez-Cabo, A. Kirilovsky, B. Mlecnik, C. Lagorce-Pages, M. Tosolini, M. Camus, A. Berger, P. Wind, F. Zinzindohoue, P. Bruneval, P. H. Cugnenc, Z. Trajanoski, W. H. Fridman, and F. Pages. 2006. Type, density, and location of immune cells within human colorectal tumors predict clinical outcome. *Science 313:1960-1964.*
44. Ahmad, M., R. C. Rees, and S. A. Ali. 2004. Escape from immunotherapy: possible mechanisms that influence tumor regression/progression. *Cancer Immunol Immunother 53:844-854.*
45. Pinzon-Charry, A., T. Maxwell, and J. A. Lopez. 2005. Dendritic cell dysfunction in cancer: a mechanism for immunosuppression. *Immunol Cell Biol 83:451-461.*
46. de Visser, K. E., A. Eichten, and L. M. Coussens. 2006. Paradoxical roles of the immune system during cancer development. *Nat Rev Cancer 6:24-37.*
47. Baniyash, M. 2006. Chronic inflammation, immunosuppression and cancer: new insights and outlook. *Semin Cancer Biol 16:80-88.*
48. Rosenberg, S. A., J. C. Yang, and N. P. Restifo. 2004. Cancer immunotherapy: moving beyond current vaccines. *Nat Med 10:909-915.*

49. Kaldjian, E. P., J. E. Gretz, A. O. Anderson, Y. Shi, and S. Shaw. 2001. Spatial and molecular organization of lymph node t cell cortex: a labyrinthine cavity bounded by an epithelium-like monolayer of fibroblastic reticular cells anchored to basement membrane-like extracellular matrix. *Int. Immunol. 13:1243-1253.*
50. Hjelmstrom, P. 2001. Lymphoid neogenesis: de novo formation of lymphoid tissue in chronic inflammation through expression of homing chemokines. *J Leukoc Biol 69:331-339.*
51. Barone, F., M. Bombardieri, A. Manzo, M. C. Blades, P. R. Morgan, S. J. Challacombe, G. Valesini, and C. Pitzalis. 2005. Association of CXCL13 and CCL21 expression with the progressive organization of lymphoid-like structures in Sjogren's syndrome. *Arthritis Rheum 52:1773-1784.*
52. Schrama, D., P. thor Straten, W. H. Fischer, A. D. McLellan, E. B. Brocker, R. A. Reisfeld, and J. C. Becker. 2001. Targeting of lymphotoxin-alpha to the tumor elicits an efficient immune response associated with induction of peripheral lymphoid-like tissue. *Immunity 14:111-121.*
53. Yu, P., Y. Lee, W. Liu, R. K. Chin, J. Wang, Y. Wang, A. Schietinger, M. Philip, H. Schreiber, and Y. X. Fu. 2004. Priming of naive T cells inside tumors leads to eradication of established tumors. *Nat Immunol 5:141-149.*
54. Sharma, S., M. Stolina, J. Luo, R. M. Strieter, M. Burdick, L. X. Zhu, R. K. Batra, and S. M. Dubinett. 2000. Secondary lymphoid tissue chemokine mediates T cell-dependent antitumor responses in vivo. *J Immunol 164:4558-4563.*
55. Vicari, A. P., S. Ait-Yahia, K. Chemin, A. Mueller, A. Zlotnik, and C. Caux. 2000. Antitumor effects of the mouse chemokine 6Ckine/SLC through angiostatic and immunological mechanisms. *J Immunol 165:1992-2000.*
56. Hromas, R., C. H. Kim, M. Klemsz, M. Krathwohl, K. Fife, S. Cooper, C. Schnizlein-Bick, and H. E. Broxmeyer. 1997. Isolation and characterization of Exodus-2, a novel C-C chemokine with a unique 37-amino acid carboxyl-terminal extension. *J Immunol 159:2554-2558.*
57. Rosenberg, S. A. 2001. Progress in human tumour immunology and immunotherapy. *Nature 411:380-384.*
58. Wu, X., Y. Li, B. Crise, and S. M. Burgess. 2003. Transcription start regions in the human genome are favored targets for MLV integration. *Science 300:1749-1751.*
59. Ratner, B., A. Hoffman, F. J. Schoen, and J. Lemons. 1996. Biomaterials Science. Academic Press, San Diego, California.
60. Langer, R., and J. P. Vacanti. 1993. Tissue engineering. *Science 260:920-926.*
61. Ma, P. X., and J. H. Elisseeff. 2006. Scaffolding in Tissue Engineering. CRC Press, Taylor & Francis Group, Boca Raton, FL.
62. Yang, S., K. F. Leong, Z. Du, and C. K. Chua. 2001. The design of scaffolds for use in tissue engineering. Part I. Traditional factors. *Tissue engineering 7:679-689.*
63. Hutmacher, D. W. 2001. Scaffold design and fabrication technologies for engineering tissues-- state of the art and future perspectives. *J Biomater Sci Polym Ed 12:107-124.*
64. Hoffman, A. S. 2001. Hydrogels for biomedical applications. *Ann N Y Acad Sci 944:62-73.*
65. Lee, K. Y., and D. J. Mooney. 2001. Hydrogels for tissue engineering. *Chem Rev 101:1869-1879.*

66. Elisseeff, J. 2004. Injectable cartilage tissue engineering. *Expert Opin Biol Ther 4:1849-1859.*
67. Burdick, J. A., and K. S. Anseth. 2002. Photoencapsulation of osteoblasts in injectable RGD-modified PEG hydrogels for bone tissue engineering. *Biomaterials 23:4315-4323.*
68. Atala, A., W. Kim, K. T. Paige, C. A. Vacanti, and A. B. Retik. 1994. Endoscopic treatment of vesicoureteral reflux with a chondrocyte-alginate suspension. *J Urol 152:641-643; discussion 644.*
69. Kuo, C. K., and P. X. Ma. 2001. Ionically crosslinked alginate hydrogels as scaffolds for tissue engineering: part 1. Structure, gelation rate and mechanical properties. *Biomaterials 22:511-521.*
70. Tabata, Y., and Y. Ikada. 1998. Protein release from gelatin matrices. *Advanced Drug Delivery Reviews 31:287-301.*
71. Bryant, S. J., and K. S. Anseth. 2003. Controlling the spatial distribution of ECM components in degradable PEG hydrogels for tissue engineering cartilage. *J Biomed Mater Res A 64:70-79.*
72. Nguyen, K. T., and J. L. West. 2002. Photopolymerizable hydrogels for tissue engineering applications. *Biomaterials 23:4307-4314.*
73. Schmedlen, R. H., K. S. Masters, and J. L. West. 2002. Photocrosslinkable polyvinyl alcohol hydrogels that can be modified with cell adhesion peptides for use in tissue engineering. *Biomaterials 23:4325-4332.*
74. Lu, S., and K. S. Anseth. 1999. Photopolymerization of multilaminated poly(HEMA) hydrogels for controlled release. *J Control Release 57:291-300.*
75. Harris, J. M., and S. Zalipsky. 1997. Poly(ethylene glycol): Chemistry and Biological Applications. American Chemical Society, Washington, DC.
76. West, J. L., and J. A. Hubbell. 1999. Polymeric biomaterials with degradation sites for proteases involved in cell migration. *Macromolecules 32:241-244.*
77. Lutolf, M. P., G. P. Raeber, A. H. Zisch, N. Tirelli, and J. A. Hubbell. 2003. Cell-responsive synthetic hydrogels. *Adv Mater 15:888-+.*
78. Gobin, A. S., and J. L. West. 2003. Val-ala-pro-gly, an elastin-derived non-integrin ligand: smooth muscle cell adhesion and specificity. *J Biomed Mater Res A 67:255-259.*
79. Sherwood, J. K., S. L. Riley, R. Palazzolo, S. C. Brown, D. C. Monkhouse, M. Coates, L. G. Griffith, L. K. Landeen, and A. Ratcliffe. 2002. A three-dimensional osteochondral composite scaffold for articular cartilage repair. *Biomaterials 23:4739-4751.*
80. Tsang, V. L., and S. N. Bhatia. 2004. Three-dimensional tissue fabrication. *Adv Drug Deliv Rev 56:1635-1647.*
81. Mooney, D. J., D. F. Baldwin, N. P. Suh, J. P. Vacanti, and R. Langer. 1996. Novel approach to fabricate porous sponges of poly(D,L-lactic-co-glycolic acid) without the use of organic solvents. *Biomaterials 17:1417-1422.*
82. Harris, L. D., B. S. Kim, and D. J. Mooney. 1998. Open pore biodegradable matrices formed with gas foaming. *Journal of biomedical materials research 42:396-402.*
83. Holy, C. E., S. M. Dang, J. E. Davies, and M. S. Shoichet. 1999. In vitro degradation of a novel poly(lactide-co-glycolide) 75/25 foam. *Biomaterials 20:1177-1185.*
84. Liao, C. J., C. F. Chen, J. H. Chen, S. F. Chiang, Y. J. Lin, and K. Y. Chang. 2001. Fabrication of porous biodegradable polymer scaffolds using a solvent merging/particulate leaching method. *J Biomed Mater Res 59:676-681.*

85. Murphy, W. L., R. G. Dennis, J. L. Kileny, and D. J. Mooney. 2002. Salt fusion: An approach to improve pore interconnectivity within tissue engineering scaffolds. *Tissue Eng 8:43-52.*
86. Ma, Z., C. Gao, Y. Gong, and J. Shen. 2003. Paraffin spheres as porogen to fabricate poly(L-lactic acid) scaffolds with improved cytocompatibility for cartilage tissue engineering. *J Biomed Mater Res B 67B:610-617.*
87. Gotoh, T., Y. Nakatani, and S. Sakohara. 1998. Novel synthesis of thermosensitive porous hydrogels. *J Appl Polym Sci 69:895-906.*
88. Vidaurre, A., I. Cortazar, and J. Meseguer. 2003. Water sorption properties of poly(ethyl acrylate-co-hydroxyethyl methacrylate) macroporous hydrogels. *Macromol. Symp. 200:283-290.*
89. Flynn, L., P. D. Dalton, and M. S. Shoichet. 2003. Fiber templating of poly(2-hydroxyethyl methacrylate) for neural tissue engineering. *Biomaterials 24:4265-4272.*
90. Behravesh, E., and A. G. Mikos. 2003. Three-dimensional culture of differentiating marrow stromal osteoblasts in biomimetic poly(propylene fumarate-co-ethylene glycol)-based macroporous hydrogels. *Journal of biomedical materials research part A 66A:698-706.*
91. Kabiri, K., H. Omidian, and M. J. Zohuriaan-Mehr. 2003. Novel approach to highly porous superabsorbent hydrogels: synergistic effect of porogens on porosity and swelling rate. *Polym Int 52:1158-1164.*
92. Chen, J., H. Park, and K. Park. 1999. Synthesis of superporous hydrogels: hydrogels with fast swelling and superabsorbent properties. *J Biomed Mater Res 44:53-62.*
93. Stein, A., and R. C. Schroden. 2001. Colloidal crystal templating of three-dimensionally ordered macroporous solids: materials for photonics and beyond. *Curr Opin Solid St M 5:553-564.*
94. Adams, M. D., A. R. Kerlavage, R. D. Fleischmann, R. A. Fuldner, C. J. Bult, N. H. Lee, E. F. Kirkness, K. G. Weinstock, J. Gocayne, O. White, G. Sutton, J. A. Blake, R. C. Brandon, M. W. Chiu, R. A. Clayton, R. T. Cline, M. D. Cotton, J. E. Hughes, L. D. Fine, L. M. Fitzgerald, et al. 1995. Initial assessment of human gene diversity and expression patterns based upon 83 million nucleotides of cDNA sequence. *Nature (Suppl.) 377:3-74.*
95. Langer, R. 1990. New methods of drug delivery. *Science 249:1527-1533.*
96. Uhrich, K. E., S. M. Cannizzaro, R. S. Langer, and K. M. Shakesheff. 1999. Polymeric systems for controlled drug release. *Chem Rev 99:3181-3198.*
97. Babensee, J. E., L. V. McIntire, and A. G. Mikos. 2000. Growth factor delivery for tissue engineering. *Pharm Res 17:497-504.*
98. Chen, R. R., and D. J. Mooney. 2003. Polymeric growth factor delivery strategies for tissue engineering. *Pharm Res 20:1103-1112.*
99. Sheridan, M. H., L. D. Shea, M. C. Peters, and D. J. Mooney. 2000. Bioabsorbable polymer scaffolds for tissue engineering capable of sustained growth factor delivery. *J Control Release 64:91-102.*
100. Peters, M. C., P. J. Polverinin, and D. J. Mooney. 2001. Engineering vascular networks in porous polymer matrices. *J Biomed Mater Res 60:668-678.*
101. Ennett, A. B., D. Kaigler, and D. J. Mooney. 2006. Temporally regulated delivery of VEGF in vitro and in vivo. *J Biomed Mater Res A 79:176-184.*

102. Mann, B. K., R. H. Schmedlen, and J. L. West. 2001. Tethered-TGF-beta increases extracellular matrix production of vascular smooth muscle cells. *Biomaterials 22:439-444.*
103. Gobin, A. S., and J. L. West. 2003. Effects of epidermal growth factor on fibroblast migration through biomimetic hydrogels. *Biotechnol Prog 19:1781-1785.*
104. Benoit, D. S., and K. S. Anseth. 2005. Heparin functionalized PEG gels that modulate protein adsorption for hMSC adhesion and differentiation. *Acta Biomater 1:461-470.*
105. Yoon, J. J., H. J. Chung, H. J. Lee, and T. G. Park. 2006. Heparin-immobilized biodegradable scaffolds for local and sustained release of angiogenic growth factor. *J Biomed Mater Res A 79:934-942.*
106. Zhang, L., E. M. Furst, and K. L. Kiick. 2006. Manipulation of hydrogel assembly and growth factor delivery via the use of peptide-polysaccharide interactions. *J Control Release 114:130-142.*
107. Seal, B. L., and A. Panitch. 2003. Physical polymer matrices based on affinity interactions between peptides and polysaccharides. *Biomacromolecules 4:1572-1582.*
108. Pratt, A. B., F. E. Weber, H. G. Schmoekel, R. Muller, and J. A. Hubbell. 2004. Synthetic extracellular matrices for in situ tissue engineering. *Biotechnol Bioeng 86:27-36.*
109. Witt, D. P., and A. D. Lander. 1994. Differential binding of chemokines to glycosaminoglycan subpopulations. *Curr Biol 4:394-400.*
110. Tanaka, Y., D. H. Adams, S. Hubscher, H. Hirano, U. Siebenlist, and S. Shaw. 1993. T-cell adhesion induced by proteoglycan-immobilized cytokine MIP-1 beta. *Nature 361:79-82.*
111. Bromley, S. K., and M. L. Dustin. 2002. Stimulation of naive T-cell adhesion and immunological synapse formation by chemokine-dependent and -independent mechanisms. *Immunology 106:289-298.*
112. Uchimura, K., M. Morimoto-Tomita, A. Bistrup, J. Li, M. Lyon, J. Gallagher, Z. Werb, and S. D. Rosen. 2006. HSulf-2, an extracellular endoglucosamine-6-sulfatase, selectively mobilizes heparin-bound growth factors and chemokines: effects on VEGF, FGF-1, and SDF-1. *BMC Biochem 7:2.*
113. Ueno, T., K. Hara, M. S. Willis, M. A. Malin, U. E. Hopken, D. H. Gray, K. Matsushima, M. Lipp, T. A. Springer, R. L. Boyd, O. Yoshie, and Y. Takahama. 2002. Role for CCR7 ligands in the emigration of newly generated T lymphocytes from the neonatal thymus. *Immunity 16:205-218.*
114. Christopherson, K. W., 2nd, J. J. Campbell, J. B. Travers, and R. A. Hromas. 2002. Low-molecular-weight heparins inhibit CCL21-induced T cell adhesion and migration. *J Pharmacol Exp Ther 302:290-295.*
115. Tangemann, K., M. D. Gunn, P. Giblin, and S. D. Rosen. 1998. A high endothelial cell-derived chemokine induces rapid, efficient, and subset-selective arrest of rolling T lymphocytes on a reconstituted endothelial substrate. *J Immunol 161:6330-6337.*
116. Miller, M. J., S. H. Wei, M. D. Cahalan, and I. Parker. 2003. Autonomous T cell trafficking examined in vivo with intravital two-photon microscopy. *Proc Natl Acad Sci U S A 100:2604-2609.*
117. Bajenoff, M., S. Granjeaud, and S. Guerder. 2003. The strategy of T cell antigen-presenting cell encounter in antigen-draining lymph nodes revealed by imaging of initial T cell activation. *J Exp Med 198:715-724.*

118. Castellino, F., A. Y. Huang, G. Altan-Bonnet, S. Stoll, C. Scheinecker, and R. N. Germain. 2006. Chemokines enhance immunity by guiding naive CD8+ T cells to sites of CD4+ T cell-dendritic cell interaction. *Nature 440:890-895.*
119. Suematsu, S., and T. Watanabe. 2004. Generation of a synthetic lymphoid tissue-like organoid in mice. *Nat Biotechnol 22:1539-1545.*
120. Okamoto, N., R. Chihara, C. Shimizu, S. Nishimoto, and T. Watanabe. 2007. Artificial lymph nodes induce potent secondary immune responses in naive and immunodeficient mice. *J Clin Invest.*
121. Lutolf, M. P., J. L. Lauer-Fields, H. G. Schmoekel, A. T. Metters, F. E. Weber, G. B. Fields, and J. A. Hubbell. 2003. Synthetic matrix metalloproteinase-sensitive hydrogels for the conduction of tissue regeneration: engineering cell-invasion characteristics. *Proc Natl Acad Sci U S A 100:5413-5418.*
122. Mann, B. K., A. S. Gobin, A. T. Tsai, R. H. Schmedlen, and J. L. West. 2001. Smooth muscle cell growth in photopolymerized hydrogels with cell adhesive and proteolytically degradable domains: synthetic ECM analogs for tissue engineering. *Biomaterials 22:3045-3051.*
123. Williams, C. G., A. N. Malik, T. K. Kim, P. N. Manson, and J. H. Elisseeff. 2005. Variable cytocompatibility of six cell lines with photoinitiators used for polymerizing hydrogels and cell encapsulation. *Biomaterials 26:1211-1218.*
124. Bryant, S. J., C. R. Nuttelman, and K. S. Anseth. 2000. Cytocompatibility of UV and visible light photoinitiating systems on cultured NIH/3T3 fibroblasts in vitro. *J Biomater Sci Polym Ed 11:439-457.*
125. Drury, J. L., and D. J. Mooney. 2003. Hydrogels for tissue engineering: scaffold design variables and applications. *Biomaterials 24:4337-4351.*
126. Ellis, D. L., and I. V. Yannas. 1996. Recent advances in tissue synthesis in vivo by use of collagen-glycosaminoglycan copolymers. *Biomaterials 17:291-299.*
127. Dziubla, T. D., M. C. Torjman, J. I. Joseph, M. Murphy-Tatum, and A. M. Lowman. 2001. Evaluation of porous networks of poly(2-hydroxyethyl methacrylate) as interfacial drug delivery devices. *Biomaterials 22:2893-2899.*
128. Ma, P. X., and J. W. Choi. 2001. Biodegradable polymer scaffolds with well-defined interconnected spherical pore network. *Tissue Eng 7:23-33.*
129. Hou, Q. P., D. W. Grijpma, and J. Feijen. 2003. Preparation of interconnected highly porous polymeric structures by a replication and freeze-drying process. *J Biomed Mater Res B 67B:732-740.*
130. Shapiro, L., and S. Cohen. 1997. Novel alginate sponges for cell culture and transplantation. *Biomaterials 18:583-590.*
131. Blanco, A., E. Chomski, S. Grabtchak, M. Ibisate, S. John, S. W. Leonard, C. Lopez, F. Meseguer, H. Miguez, J. P. Mondia, G. A. Ozin, O. Toader, and H. M. van Driel. 2000. Large-scale synthesis of a silicon photonic crystal with a complete three-dimensional bandgap near 1.5 micrometres. *Nature 405:437-440.*
132. Xia, Y. N., B. Gates, Y. D. Yin, and Y. Lu. 2000. Monodispersed colloidal spheres: Old materials with new applications. *Adv Mater 12:693-713.*
133. Stein, A. 2001. Sphere templating methods for periodic porous solids. *Micropor Mesopor Mat 44-45:227-239.*
134. Jiang, P., J. F. Bertone, and V. L. Colvin. 2001. A lost-wax approach to monodisperse colloids and their crystals. *Science 291:453-457.*

135. Ruoslahti, E., and M. D. Pierschbacher. 1987. New perspectives in cell adhesion: RGD and integrins. *Science 238:491-497.*
136. van Wachem, P. B., J. A. Plantinga, M. J. B. Wissink, R. Beernink, A. A. Poot, G. H. M. Engbers, T. Beugeling, and etc. 2001. In vivo biocompatibility of carbodiimide-crosslinked collagen matrices: effects of crosslink density, heparin immobilization, and bFGF loading. *J Biomed Mater Res 55:368-378.*
137. Ito, K., K. Tanaka, H. Tanak, G. Imai, S. Kawaguchi, and S. Itsuno. 1991. Poly(ethylene oxide) macromonomers. 7. Micellar polymerization in water. *Macromolecules 24.*
138. Irvine, D. J., A. Stachowiak, and S. Jain. 2003. Engineering biomaterials for control of immune cell functions. *Mater. Sci. Forum 426-432:3213-3218.*
139. Hughes, B. D. 1996. *Random Walks and Random Environments.* Clarendon Press, Oxford.
140. Blease, J., J. W. Essam, and C. M. Place. 1976. Critical behaviour of the percolation probability for the bond problem on a three dimensional lattice. *Phys Lett 57A:199-200.*
141. Gomes, M. E., A. S. Ribeiro, P. B. Malafaya, R. L. Reis, and A. M. Cunha. 2001. A new approach based on injection moulding to produce biodegradable starch-based polymeric scaffolds: morphology, mechanical and degradation behaviour. *Biomaterials 22:883-889.*
142. Hulbert, S. F., F. A. Young, R. S. Mathews, J. J. Klawitter, C. D. Talbert, and F. H. Stelling. 1970. Potential of ceramic materials as permanently implantable skeletal prostheses. *J Biomed Mater Res 4:433-456.*
143. Taylor, S. R., and D. F. Gibbons. 1983. Effect of surface texture on the soft tissue response to polymer implants. *J Biomed Mater Res 17:205-227.*
144. Chirila, T. V., I. J. Constable, G. J. Crawford, S. Vijayasekaran, D. E. Thompson, Y. C. Chen, W. A. Fletcher, and B. J. Griffin. 1993. Poly(2-hydroxyethyl methacrylate) sponges as implant materials: in vivo and in vitro evaluation of cellular invasion. *Biomaterials 14:26-38.*
145. Pradas, M. M., J. L. G. Ribelles, A. S. Aroca, G. G. Ferrer, J. S. Anton, and P. Pissis. 2001. Porous poly(2-hydroxyethyl acrylate) hydrogels. *Polymer 42:4667-4674.*
146. Liu, Q., E. L. Hedberg, Z. W. Liu, R. Bahulekar, R. K. Meszlenyi, and A. G. Mikos. 2000. Preparation of macroporous poly(2-hydroxyethyl methacrylate) hydrogels by enhanced phase separation. *Biomaterials 21:2163-2169.*
147. Barbucci, R., and G. Leone. 2004. Formation of defined microporous 3D structures starting from cross-linked hydrogels. *J Biomed Mater Res 68B:117-126.*
148. Samani, A., J. Bishop, C. Luginbuhl, and D. B. Plewes. 2003. Measuring the elastic modulus of ex vivo small tissue samples. *Phys Med Biol 48:2183-2198.*
149. Yeh, W. C., P. C. Li, Y. M. Jeng, H. C. Hsu, P. L. Kuo, M. L. Li, P. M. Yang, and P. H. Lee. 2002. Elastic modulus measurements of human liver and correlation with pathology. *Ultrasound Med Biol 28:467-474.*
150. Narkis, M. 1979. Sintering Behavior of Poly(Methyl Methacrylate) Particles. *Polymer Engineering and Science 19:889-892.*
151. Kuijpers, A. J., G. H. Engbers, J. Krijgsveld, S. A. Zaat, J. Dankert, and J. Feijen. 2000. Cross-linking and characterisation of gelatin matrices for biomedical applications. *J Biomater Sci Polym Ed 11:225-243.*
152. Kotov, N. A., Y. Liu, S. Wang, C. Cumming, M. Eghtedari, G. Vargas, M. Motamedi, J. Nichols, and J. Cortiella. 2004. Inverted colloidal crystals as three-dimensional cell scaffolds. *Langmuir 20:7887-7892.*

153. Marshall, A., and B. Ratner. 2005. Quantitative characterization of sphere-templated porous biomaterials. *Tissue Eng 9:337-345.*
154. Shanbhag, S., J. Woo Lee, and N. Kotov. 2005. Diffusion in three-dimensionally ordered scaffolds with inverted colloidal crystal geometry. *Biomaterials 26:5581-5585.*
155. Sannino, A., P. A. Netti, M. Madaghiele, V. Coccoli, A. Luciani, A. Maffezzoli, and L. Nicolais. 2006. Synthesis and characterization of macroporous poly(ethylene glycol)-based hydrogels for tissue engineering application. *J Biomed Mater Res A 79:229-236.*
156. Negulescu, P. A., T. B. Krasieva, A. Khan, H. H. Kerschbaum, and M. D. Cahalan. 1996. Polarity of T cell shape, motility, and sensitivity to antigen. *Immunity 4:421-430.*
157. Wilkinson, P. C. 1986. The locomotor capacity of human lymphocytes and its enhancement by cell growth. *Immunology 57:281-289.*
158. Kaiser, A., E. Donnadieu, J. P. Abastado, A. Trautmann, and A. Nardin. 2005. CC chemokine ligand 19 secreted by mature dendritic cells increases naive T cell scanning behavior and their response to rare cognate antigen. *J Immunol 175:2349-2356.*
159. Okada, T., M. J. Miller, I. Parker, M. F. Krummel, M. Neighbors, S. B. Hartley, A. O'Garra, M. D. Cahalan, and J. G. Cyster. 2005. Antigen-engaged B cells undergo chemotaxis toward the T zone and form motile conjugates with helper T cells. *PLoS Biol 3:e150.*
160. Huang, A. Y., H. Qi, and R. N. Germain. 2004. Illuminating the landscape of in vivo immunity: insights from dynamic in situ imaging of secondary lymphoid tissues. *Immunity 21:331-339.*
161. Miller, M. J., O. Safrina, I. Parker, and M. D. Cahalan. 2004. Imaging the single cell dynamics of CD4+ T cell activation by dendritic cells in lymph nodes. *J Exp Med 200:847-856.*
162. Cyster, J. G. 2005. Chemokines, sphingosine-1-phosphate, and cell migration in secondary lymphoid organs. *Annu Rev Immunol 23:127-159.*
163. Yoshida, R., M. Nagira, T. Imai, M. Baba, S. Takagi, Y. Tabira, J. Akagi, H. Nomiyama, and O. Yoshie. 1998. EBI1-ligand chemokine (ELC) attracts a broad spectrum of lymphocytes: activated T cells strongly up-regulate CCR7 and efficiently migrate toward ELC. *Int Immunol 10:901-910.*
164. Campbell, J. J., J. Hedrick, A. Zlotnik, M. A. Siani, D. A. Thompson, and E. C. Butcher. 1998. Chemokines and the arrest of lymphocytes rolling under flow conditions. *Science 279:381-384.*
165. Frow, E. K., J. Reckless, and D. J. Grainger. 2004. Tools for anti-inflammatory drug design: in vitro models of leukocyte migration. *Med Res Rev 24:276-298.*
166. Dunzendorfer, S., A. Kaser, C. Meierhofer, H. Tilg, and C. J. Wiedermann. 2000. Dendritic cell migration in different micropore filter assays. *Immunol Lett 71:5-11.*
167. Inaba, K., M. Inaba, N. Romani, H. Aya, M. Deguchi, S. Ikehara, S. Muramatsu, and R. M. Steinman. 1992. Generation of large numbers of dendritic cells from mouse bone marrow cultures supplemented with granulocyte/macrophage colony-stimulating factor. *J Exp Med 176:1693-1702.*
168. Nombela-Arrieta, C., R. A. Lacalle, M. C. Montoya, Y. Kunisaki, D. Megias, M. Marques, A. C. Carrera, S. Manes, Y. Fukui, A. C. Martinez, and J. V. Stein. 2004. Differential requirements for DOCK2 and phosphoinositide-3-kinase gamma during T and B lymphocyte homing. *Immunity 21:429-441.*

169. Brown, M. J., R. Nijhara, J. A. Hallam, M. Gignac, K. M. Yamada, S. L. Erlandsen, J. Delon, M. Kruhlak, and S. Shaw. 2003. Chemokine stimulation of human peripheral blood T lymphocytes induces rapid dephosphorylation of ERM proteins, which facilitates loss of microvilli and polarization. *Blood 102:3890-3899.*
170. Dustin, M. L., and J. A. Cooper. 2000. The immunological synapse and the actin cytoskeleton: molecular hardware for T cell signaling. *Nat Immunol 1:23-29.*
171. Laudanna, C., J. Y. Kim, G. Constantin, and E. Butcher. 2002. Rapid leukocyte integrin activation by chemokines. *Immunol Rev 186:37-46.*
172. Dustin, M. L., and T. A. Springer. 1989. T-cell receptor cross-linking transiently stimulates adhesiveness through LFA-1. *Nature 341:619-624.*
173. Palecek, S. P., J. C. Loftus, M. H. Ginsberg, D. A. Lauffenburger, and A. F. Horwitz. 1997. Integrin-ligand binding properties govern cell migration speed through cell-substratum adhesiveness. *Nature 385:537-540.*
174. Barnden, M. J., J. Allison, W. R. Heath, and F. R. Carbone. 1998. Defective TCR expression in transgenic mice constructed using cDNA-based alpha- and beta-chain genes under the control of heterologous regulatory elements. *Immunol Cell Biol 76:34-40.*
175. Lo, C. G., Y. Xu, R. L. Proia, and J. G. Cyster. 2005. Cyclical modulation of sphingosine-1-phosphate receptor 1 surface expression during lymphocyte recirculation and relationship to lymphoid organ transit. *J Exp Med 201:291-301.*
176. Blattman, J. N., R. Antia, D. J. Sourdive, X. Wang, S. M. Kaech, K. Murali-Krishna, J. D. Altman, and R. Ahmed. 2002. Estimating the precursor frequency of naive antigen-specific CD8 T cells. *J Exp Med 195:657-664.*
177. Westermann, J., U. Bode, A. Sahle, U. Speck, N. Karin, E. B. Bell, K. Kalies, and A. Gebert. 2005. Naive, effector, and memory T lymphocytes efficiently scan dendritic cells in vivo: contact frequency in T cell zones of secondary lymphoid organs does not depend on LFA-1 expression and facilitates survival of effector T cells. *J Immunol 174:2517-2524.*
178. Katakai, T., T. Hara, M. Sugai, H. Gonda, and A. Shimuzu. 2004. Lymph node fibroblastic reticular cells construct the stromal reticulum via contact with lymphocytes. *Journal of Experimental Medicine 200:783-795.*
179. de la Fuente, H., M. Mittelbrunn, L. Sanchez-Martin, M. Vicente-Manzanares, A. Lamana, R. Pardi, C. Cabanas, and F. Sanchez-Madrid. 2005. Synaptic clusters of MHC class II molecules induced on DCs by adhesion molecule-mediated initial T-cell scanning. *Molecular Biology of the Cell 16:3314-3322.*
180. Bardi, G., M. Lipp, M. Baggiolini, and P. Loetscher. 2001. The T cell chemokine receptor CCR7 is internalized on stimulation with ELC, but not with SLC. *Eur J Immunol 31:3291-3297.*
181. Proudfoot, A. E., T. M. Handel, Z. Johnson, E. K. Lau, P. LiWang, I. Clark-Lewis, F. Borlat, T. N. Wells, and M. H. Kosco-Vilbois. 2003. Glycosaminoglycan binding and oligomerization are essential for the in vivo activity of certain chemokines. *Proc Natl Acad Sci U S A 100:1885-1890.*
182. Bromley, S. K., D. A. Peterson, M. D. Gunn, and M. L. Dustin. 2000. Cutting edge: hierarchy of chemokine receptor and TCR signals regulating T cell migration and proliferation. *J Immunol 165:15-19.*
183. Ratner, S., R. K. Jasti, and G. H. Heppner. 1988. Motility of murine lymphocytes during transit through cell cycle. Analysis by a new in vitro assay. *J Immunol 140:583-588.*

184. Smith, A., Y. R. Carrasco, P. Stanley, N. Kieffer, F. D. Batista, and N. Hogg. 2005. A talin-dependent LFA-1 focal zone is formed by rapidly migrating T lymphocytes. *J Cell Biol 170:141-151.*
185. Volkov, Y., A. Long, S. McGrath, D. Ni Eidhin, and D. Kelleher. 2001. Crucial importance of PKC-beta(I) in LFA-1-mediated locomotion of activated T cells. *Nat Immunol 2:508-514.*
186. Ge, Q., D. Palliser, H. N. Eisen, and J. Chen. 2002. Homeostatic T cell proliferation in a T cell-dendritic cell coculture system. *Proc Natl Acad Sci U S A 99:2983-2988.*
187. Kondo, T., I. Cortese, S. Markovic-Plese, K. P. Wandinger, C. Carter, M. Brown, S. Leitman, and R. Martin. 2001. Dendritic cells signal T cells in the absence of exogenous antigen. *Nat Immunol 2:932-938.*
188. Dieu, M. C., B. Vanbervliet, A. Vicari, J. M. Bridon, E. Oldham, S. Ait-Yahia, F. Briere, A. Zlotnik, S. Lebecque, and C. Caux. 1998. Selective recruitment of immature and mature dendritic cells by distinct chemokines expressed in different anatomic sites. *J Exp Med 188:373-386.*
189. Riol-Blanco, L., N. Sanchez-Sanchez, A. Torres, A. Tejedor, S. Narumiya, A. L. Corbi, P. Sanchez-Mateos, and J. L. Rodriguez-Fernandez. 2005. The chemokine receptor CCR7 activates in dendritic cells two signaling modules that independently regulate chemotaxis and migratory speed. *J Immunol 174:4070-4080.*
190. Yanagawa, Y., and K. Onoe. 2002. CCL19 induces rapid dendritic extension of murine dendritic cells. *Blood 100:1948-1956.*
191. Marsland, B. J., P. Battig, M. Bauer, C. Ruedl, U. Lassing, R. R. Beerli, K. Dietmeier, L. Ivanova, T. Pfister, L. Vogt, H. Nakano, C. Nembrini, P. Saudan, M. Kopf, and M. F. Bachmann. 2005. CCL19 and CCL21 induce a potent proinflammatory differentiation program in licensed dendritic cells. *Immunity 22:493-505.*
192. Katou, F., H. Ohtani, T. Nakayama, H. Nagura, O. Yoshie, and K. Motegi. 2003. Differential expression of CCL19 by DC-Lamp+ mature dendritic cells in human lymph node versus chronically inflamed skin. *J Pathol 199:98-106.*
193. Yee, C., M. J. Gilbert, S. R. Riddell, V. G. Brichard, A. Fefer, J. A. Thompson, T. Boon, and P. D. Greenberg. 1996. Isolation of tyrosinase-specific CD8+ and CD4+ T cell clones from the peripheral blood of melanoma patients following in vitro stimulation with recombinant vaccinia virus. *J Immunol 157:4079-4086.*
194. Stachowiak, A. N., A. Bershteyn, E. Tzatzalos, and D. J. Irvine. 2005. Bioactive Hydrogels with an Ordered Cellular Structure Combine Interconnected Macroporosity and Robust Mechanical Properties. *Advanced Materials 17:399-403.*
195. del Pozo, M. A., P. Sanchez-Mateos, M. Nieto, and F. Sanchez-Madrid. 1995. Chemokines regulate cellular polarization and adhesion receptor redistribution during lymphocyte interaction with endothelium and extracellular matrix. Involvement of cAMP signaling pathway. *J Cell Biol 131:495-508.*
196. Stachowiak, A. N., Y. Wang, Y. C. Huang, and D. J. Irvine. 2006. Homeostatic lymphoid chemokines synergize with adhesion ligands to trigger T and B lymphocyte chemokinesis. *J Immunol 177:2340-2348.*
197. Friedl, P., K. S. Zanker, and E. B. Brocker. 1998. Cell migration strategies in 3-D extracellular matrix: differences in morphology, cell matrix interactions, and integrin function. *Microsc Res Tech 43:369-378.*

198. Hautanen, A., J. Gailit, D. M. Mann, and E. Ruoslahti. 1989. Effects of modifications of the RGD sequence and its context on recognition by the fibronectin receptor. *J Biol Chem 264:1437-1442.*
199. Shimizu, Y., and S. Shaw. 1991. Lymphocyte interactions with extracellular matrix. *Faseb J 5:2292-2299.*
200. Friedl, P., F. Entschladen, C. Conrad, B. Niggemann, and K. S. Zanker. 1998. CD4+ T lymphocytes migrating in three-dimensional collagen lattices lack focal adhesions and utilize beta1 integrin-independent strategies for polarization, interaction with collagen fibers and locomotion. *Eur J Immunol 28:2331-2343.*
201. Franitza, S., R. Alon, and O. Lider. 1999. Real-time analysis of integrin-mediated chemotactic migration of T lymphocytes within 3-D extracellular matrix-like gels. *J Immunol Methods 225:9-25.*
202. Gunzer, M., A. Schafer, S. Borgmann, S. Grabbe, K. S. Zanker, E. B. Brocker, E. Kampgen, and P. Friedl. 2000. Antigen presentation in extracellular matrix: interactions of T cells with dendritic cells are dynamic, short lived, and sequential. *Immunity 13:323-332.*
203. Maheshwari, G., G. Brown, D. A. Lauffenburger, A. Wells, and L. G. Griffith. 2000. Cell adhesion and motility depend on nanoscale RGD clustering. *J. Cell. Sci. 113:1677-1686.*
204. Hern, D. L., and J. A. Hubbell. 1998. Incorporation of adhesion peptides into nonadhesive hydrogels useful for tissue resurfacing. *J Biomed Mater Res 39:266-276.*
205. Maheshwari, G., G. Brown, D. A. Lauffenburger, A. Wells, and L. G. Griffith. 2000. Cell adhesion and motility depend on nanoscale RGD clustering. *J Cell Sci 113 (Pt 10):1677-1686.*
206. Green, N. 1975. Avidin. *Advanced Protein Chemistry 29:85-133.*
207. Shakhar, G., R. L. Lindquist, D. Skokos, D. Dudziak, J. H. Huang, M. C. Nussenzweig, and M. L. Dustin. 2005. Stable T cell-dendritic cell interactions precede the development of both tolerance and immunity in vivo. *Nat Immunol.*
208. Pierre, P., S. J. Turley, E. Gatti, M. Hull, J. Meltzer, A. Mirza, K. Inaba, R. M. Steinman, and I. Mellman. 1997. Developmental regulation of MHC class II transport in mouse dendritic cells. *Nature 388:787-792.*
209. Zhou, Y. W., S. Aritake, A. Tri Endharti, J. Wu, A. Hayakawa, I. Nakashima, and H. Suzuki. 2003. Murine lymph node-derived stromal cells effectively support survival but induce no activation/proliferation of peripheral resting T cells in vitro. *Immunology 109:496-503.*
210. Friedl, P. 2004. Dynamic imaging of cellular interactions with extracellular matrix. *Histochem Cell Biol 122:183-190.*
211. Gunn, M. D., S. Kyuwa, C. Tam, T. Kakiuchi, A. Matsuzawa, L. T. Williams, and H. Nakano. 1999. Mice lacking expression of secondary lymphoid organ chemokine have defects in lymphocyte homing and dendritic cell localization. *J Exp Med 189:451-460.*
212. Nagira, M., T. Imai, R. Yoshida, S. Takagi, M. Iwasaki, M. Baba, Y. Tabira, J. Akagi, H. Nomiyama, and O. Yoshie. 1998. A lymphocyte-specific CC chemokine, secondary lymphoid tissue chemokine (SLC), is a highly efficient chemoattractant for B cells and activated T cells. *Eur J Immunol 28:1516-1523.*
213. Lortat-Jacob, H., A. Grosdidier, and A. Imberty. 2002. Structural diversity of heparan sulfate binding domains in chemokines. *Proc Natl Acad Sci U S A 99:1229-1234.*

214. Kleindienst, P., and T. Brocker. 2003. Endogenous dendritic cells are required for amplification of T cell responses induced by dendritic cell vaccines in vivo. *J Immunol 170:2817-2823.*
215. Cupedo, T., W. Jansen, G. Kraal, and R. E. Mebius. 2004. Induction of secondary and tertiary lymphoid structures in the skin. *Immunity 21:655-667.*
216. Shreedhar, V., A. M. Moodycliffe, S. E. Ullrich, C. Bucana, M. L. Kripke, and L. Flores-Romo. 1999. Dendritic cells require T cells for functional maturation in vivo. *Immunity 11:625-636.*
217. Hugues, S., L. Fetler, L. Bonifaz, J. Helft, F. Amblard, and S. Amigorena. 2004. Distinct T cell dynamics in lymph nodes during the induction of tolerance and immunity. *Nat Immunol 5:1235-1242.*
218. Gibson, L. J., and M. F. Ashby. 1997. *Cellular Solids: Structure and Properties.* University Press, Cambridge, UK.
219. Caterson, E. J., L. J. Nesti, W. J. Li, K. G. Danielson, T. J. Albert, A. R. Vaccaro, and R. S. Tuan. 2001. Three-dimensional cartilage formation by bone marrow-derived cells seeded in polylactide/alginate amalgam. *J Biomed Mater Res 57:394-403.*
220. Chen, G., T. Sato, T. Ushida, N. Ochiai, and T. Tateishi. 2004. Tissue engineering of cartilage using a hybrid scaffold of synthetic polymer and collagen. *Tissue Eng 10:323-330.*

Appendix A Abbreviations used

Ab = antibody
BSA = bovine serum albumin
conc. = concentration
ECM = extracellular matrix
M = million (cells) or molar (solutions)
O/N = overnight
resus. = resuspend
RT = room temperature
v = volume
wt = weight

Appendix B Preparation of common buffers

Important note: Any buffer that is to be used with cells should be filtered (using a 0.2 μm filter) in a sterile laminar flow hood.

B.1 Buffers for cell culture and isolation

B.1.1 RPMI complete cell culture medium (RPMI-10):

1) Mix together:
    a. RPMI 1640 (with 2 mM L-glut) powder at 10.4 g/L in water
    b. 10 mM HEPES acid
2) Bring solution pH to ~ 7.1-7.2 if necessary. Usually with this amount of HEPES it is already at the right pH prior to filtering.
3) In a sterile hood, add:
    a. fetal calf serum (FCS) to 10% (v/v)
    b. 100 U/mL penicillin/100 μg/mL streptomycin
    c. 50 μM 2-mercaptoethanol
4) Sterile filter as usual with bottle top filter.

B.1.2 Serum-free RPMI (SF-RPMI):

Prepare as for complete medium, but do not add FCS.

B.1.3 2-Mercaptoethanol Stock Solution:

Neat 2-mercaptoethanol (2-ME) is at 14.3 M.
To prepare 50 mM stock: add 143 μL 2-ME to 40 mL water (re-make every ~ 4 months).

B.1.4 Red blood cell (RBC) lysis buffer:

175 mM ammonium chloride in water, sterile-filtered.

Collagenase solutions:

Collagenase D ordered from Roche is typically 0.15 Wunsch/mg, 250 Mandl/mg. It should be reconstituted at 4000 Mandl/mL in HBSS and stored frozen. (Note: Current Protocols in Immunology claims conversion of 750 Mandl/Wunsch unit.) Enzyme activity is dependent on the presence of calcium.

Liberase comes in several speciality enzyme blends, which have high activity (~ 4 W/mg). Recommended usage is at 1:50.

B.1.5 MACS Buffer:

PBS pH 7.4, containing:
0.5 % BSA
0.1% NaN3
2 mM EDTA (MW = 416.23 → 0.832 g/L)

B.1.6 Lipopolysacharride (LPS) stock:

Prepare stock solution at 1 mg/mL in sterile PBS. Vortex thoroughly and if necessary also sonicate for 5-10 min.

B.2 Buffers for common assays

B.2.1 Hank's Balanced Salt Solution (HBSS):

Note: usually make calcium and magnesium free (HBSS-CMF) version.

5.4 mM KCl (0.402 g)
0.3 mM Na_2HPO_4 ($\bullet 7H_2O$) (0.09 g; 0.0426 g for anhydrous) ["*dibasic*"]
0.4 mM KH_2PO_4 (0.054 g) ["*monobasic*"]
4.2 mM $NaHCO_3$ (0.353 g)
137 mM NaCl (8.0 g)
5.6 mM D-glucose (1.0 g)
0.2 g phenol red (optional)
1.3 mM CaCl2 (0.14 g; optional)
0.5 mM $MgCl_2 \bullet 6H_2O$ (0.10 g; optional)
0.6 mM $MgSO_4 \bullet 7H_2O$ (0.10 g; optional)

Add H_2O to 1 liter and adjust pH to 7.4 with 1 M HCl or 1 M NaOH.
Filter sterilize and store up to 1 month at 4 °C.

B.2.2 FACS staining buffer

Prepare HBSS-CMF, containing:
0.1% (w/v) sodium azide (NaN_3)
1.0% (w/v) bovine serum albumin (BSA; fraction V)
Store at 4°C up to 1 year.

B.2.3 Propidium Iodide Stock Solution:

1 mg/mL in PBS (store protected from light at 4°C). Final usage typically 1.25 µg/mL.

B.2.4 ELISA Buffers:

Reagent Diluent – 1% BSA in PBS, pH 7.4 (10 g BSA in 1 liter PBS)

Blocking Buffer – 1% BSA, 5% sucrose, 0.05% NaN_3 in PBS.

Wash Buffer – 0.05% Tween 20 in PBS, pH 7.4 – make from tablets (Calbiochem, Inc)

Stop Solution - 1 M H_2SO_4 (~ 53 mL per L H_2O).
H_2SO_4 MW = 98.1, density = 1.84 g/cm^3

Appendix C Cell Isolation and Treatments

C.1 General treatments

C.1.1 Cell centrifugation/washing procedures:

1) Cell suspensions are typically centrifuged for 5 min at 1300 rpm on a centrifuge with a GH-38 rotor (~200-400 g) to form a cell pellet.
2) Liquid is aspirated from the cell pellet using a clean pipet hooked up to vacuum.
3) The cells are initially resuspended in a small volume of buffer or medium.
4) Only then should a large volume of solution for washing or culturing be added.

C.1.2 Pertussis toxin (PTX) treatment:

Materials:

PTX (Sigma): P7208 – 50 μg.
Reconstitute with 500 μL water – results in PBS because lyophilized with salts.
Stable for 6 months.

PTX B oligomer (Sigma): P159 – 40 μg.
Reconsitute with water or buffer. This is used as a control.

Procedure:

Initial concentration is 100 μg/mL; desire 2-100 ng/mL for final conc.

1) For 100ng/mL = 1:1000 overall, dilute 1:10 followed by 1:100.
2) Incubate cells (at 10M/mL) for 10 min with PTX
    a. I usually did in full medium, though PBS was used in original report.
3) Wash 3 times.
4) Rest cells for 90-120 min at 37 °C before use.

C.2 Cell isolation

C.2.1 Splenocyte preparation:

Dissection:

1) Put mouse in euthanizing chamber.
2) Turn on CO_2 at low pressure for ~ 1min.
3) Raise pressure to high and leave on for ~ 4 min.
4) Pull on mouse leg to test for limpness (absence of reflex) and therefore death.
5) Cut open the mouse torso, through the skin but not the thin membrane below initially.

6) Wipe fur off of scissors, then cut through the membrane film, toward left side of mouse.
7) Remove spleen with tweezers, tearing away pancreatic filaments without bursting open the spleen. Put in ice cold RPMI (e.g., in a conical tube).
8) Make a cut in the mouse lungs to doubly ensure death, put in plastic bag and dispose of in carcass freezer.

Isolation:

1) Prepare a 50 mL Falcon conical tube and cell strainer (70 μm).
2) Burst and press spleen through pre-wet filter using a syringe plunger.
3) Wash with 10 mL RPMI (20 mL for 2 spleens) and continue pressing.
4) Centrifuge cells as usual, resuspend in 100 (or 200) μL complete RPMI.
5) Add 5 mL RBC lysis buffer, invert tube once to mix, incubate 5 min at RT.
6) Add 7.5 mL complete RPMI, 7.5 mL SF-RPMI, invert once, then centrifuge.
7) Resuspend in 100 μL RPMI, then add 10 mL RPMI and 10 mL SF-RPMI. Tap/flick tube to promote dead cell clump formation and floating, then filter through new cell strainer (40 μm) into new 50 mL conical tube.
8) Take an aliquot for cell counting, then centrifuge as usual.
9) Resuspend in MACS buffer, appropriate labeling buffer, or culture medium.

Note: Resuspending a spleen in SF-RPMI alone seems to promote fat precipitation in a way that can lose a lot of cells. However, prior to MACS separation it is desirable to get rid of as much serum as possible. For this reason, I use a 50/50 mix in steps 6 and 7.

C.2.2 Lymphocyte isolation from splenocytes (or lymph nodes):

Materials:

Ab cocktail (all from BD Biosciences): CD8α, CD11b, B220, and NK1.1, each at 1 μg/mL. Anti-biotin microbeads are sold as a stand-alone item from Miltenyi Biotech (130-090-485).

Isolation:

1) Degas MACS buffer using vacuum line and prepare cells as usual (must lyse RBCs in splenocytes, but not in lymph node cells because there are very few).
2) Suspend cells in MACS buffer at 100M cells/mL.
3) Add 8 μL Ab-cocktail per mL cells and incubate 10 min.
4) Wash cells two times with 10-20x staining volume.
5) Resuspend in 40 μL buffer + 10 μL anti-biotin microbeads for 20M cells, or scale up accordingly for more cells. (Has not been tested for < 20M cells.)
6) Incubate 15 min.
7) Wash once with 10-20x staining volume.
8) Perform MACS separation as usual.

C.2.3 Lymphocyte non-specific priming:

Procedure:

1) Add 150-200 µL of antibody solution (10 µg/mL each CD3 and CD28) to 6-8 wells of a 24-well tissue culture plate, and incubate at 37 °C for at least 90 min.
2) Meanwhile, harvest $CD4^+$ T cells from splenocytes and/or lymph node cells as usual.
3) Count T cells, and resuspend at 1.1-1.3 M cells/mL.
4) Rinse tissue culture plate with PBS 3X prior to use, then plate cells at 1 mL per well.
5) After ~ 48 h, prepare IL-2 in fresh culture medium, and plate 0.67 mL per well in a fresh tissue culture plate. The final IL-2 concentration in step (6) should be 5 ng/mL.
6) Observe the 2-day-old T cells to ensure that they are blasting (enlarged). In a sterile hood, pipet several times to mix, then add 0.33 mL of cells to each well in the fresh plate. Thus, each well in the old plate will be split into three wells in the new plate.

C.2.4 BMDC (bone marrow dendritic cell) extraction and preparation:

Dissection:

1) Euthanize mouse with carbon dioxide gas in chamber.
2) Pin mouse legs down in a stretched out position.
3) Cut open the mouse, and cut down from thigh to as close as possible to the ankle.
4) Strip muscle away from tibia with forceps; cut through bone at ankle.
5) Move tibia around until it breaks at knee (shiny part), or cut at knee if needed.
6) Strip muscle away from femur, cutting as well if necessary.
7) Move femur around until can tell where hip socket is; cut femur as close to hip socket as possible.
8) Repeat procedure for other leg if desired.

(Store bones in 10 mL cold RPMI 1640 as they are collected one by one.)

Isolation:

1) Put bones into a 10 cm culture dish, and add ~ 10 mL more media.
2) Prepare a 50 mL Falcon conical tube and cell strainer (70 µm).
3) Use 26G needle and 1 mL syringe to inject one bone at a time with medium, while holding the bone over the prepared cell strainer. (Cut the ends of the bone off first if necessary to open it up well enough.
4) Keep washing out the red bone marrow/blood until the bone appears white.
5) Lyse red blood cells as for spleen, count cells, and resuspend at 1M cells per mL.
6) Add 5ng/mL of GM-CSF to cells.
    a. 0.5-1 µL per mL depending on stock solution
    b. Expect 15-25M cells per leg.
7) Plate 1 mL of cells/media/GM-CSF per well in 24-well plate.

Culturing:

On days 2, 4, and 6:

1) Gently remove 0.7 mL medium from each well, minimally disturbing cells.
2) Replace with pre-warmed fresh medium + GM-CSF at 5 ng/mL.

C.2.5 Splenic DC Preparation:

Collagenase D solution: 2 mg/mL of >= 0.15 Wunsch U/mg enzyme should be used. This means using Roche stock solution at ~1:8 by volume.

Procedure:

1) Isolate spleen and put in petri dish with collagenase D (5 mL/spleen).
2) Inject spleen with 0.5 mL solution (1 mL, ~26 G needle).
3) Incubate for 45-60 min.
4) Pass through 70 μm cell strainer.
5) Collect, wash to final volume of 14 mL, count.
6) Resuspend in 100 μL buffer + 25 μL CD11c beads (this is 1/4 of is recommended by Miltenyi; Rob says we can use even less) per 100M cells.
7) Incubate 15 min.
8) Wash with 10-20x buffer.
9) Separate on MACS column as usual.
10) Repeat on second column for better purity.

Notes:

- The Miltenyi protocol suggests using HEPES-buffered saline, but I have used Hank's Balanced Salt Solution instead.
- I have used as little as 2 mL per spleen at 1 mg/mL enzyme.
- Expect about 1-3M cells per spleen.
- Total prep time: 2-2.5 hours.

C.2.6 MACS column separation:

MS (Mini) columns:

Resuspend cells in 0.5 mL buffer per 100 M cells.
Place column onto magnet, then wash with 0.5 mL MACS buffer.
Add cells to column and collect eluent (for negative selection).
Wash 3x with 0.5 mL each.
For positive selection, remove column from magnet, then place 1 mL onto column and use plunger to quickly collect cells.

Max cells: 200M
Max positive cells: 10M

LS (Midi) columns:

Resuspend cells in 0.5 mL buffer per 100 M cells.
Place column onto magnet, then wash with 3 mL MACS buffer.
Add cells to column and collect eluent (for negative selection).
Wash 4x with 3 mL each.
For positive selection, remove column from magnet, then place 5 mL onto column and use plunger to quickly collect cells.

Max cells: 2000M
Max positive cells: 100M

C.3 Fluorescent Labeling of Cells

Unless noted otherwise below, most dye stocks are stored frozen at –20 °C, and can be thawed and re-frozen multiple times over a period of 1-2 months at least. Dyes that have not yet been reconstituted with DMSO are good for 1-2 years frozen.

RED DYES

C.3.1 CMTMR (Molecular Probes):

Background:

- Excitation/Emission Max = 541/565 nm.
- Inherited by daughter cells through at least four divisions.
- Bright for at least 72 hours.
- Does not require enzymatic cleavage to activate fluorescence
- Transformed into cell-impermeant reaction products once inside cell.
- MW = 554.04

Procedure:

1) Prepare stock on order of 10 mM in DMSO. [e.g., 1 mg/mL for 36 mM]
2) Prepare cell suspension at 100M/mL in serum free medium.
3) Prepare diluted CMTMR (see 4a) and immediately proceed to step 4.
4) Add 1x volume cells to 9x volume of CMTMR solution and rapidly invert/mix.
    a. final dilution of CMTMR should be 0.5-25 μM
    b. final dilution of cells is 10M/mL
5) Incubate for 15-45 minutes at growth temperatures. [usually 20 min]
6) Wash with 10x volume pre-warmed medium.
7) Resuspend cells in 1x volume pre-warmed medium and incubate for 30 min at 37 °C.
8) Wash cells twice with cold PBS.

Comments:

- This dye seems to leak from cells despite extra incubation and washing.
- The dye is then taken up by PEG gels over time.

C.3.2 PKH26 Red (Sigma)

Background:

- Excitation/Emission Max = 551/567 nm.
- Incorporated into lipid regions of the cell membrane.
- Avoid volumes less than 100 μL or greater than 1mL.

Procedure:

All should be done at room temperature, under sterile conditions, in polypropylene tubes.

1) Wash cells with serum-free medium, centrifuge.
2) Add Diluent C (e.g., 1 mL for 10^7 cells): pipet but do not vortex.
3) Prepare 4e-6 M dye in Diluent C (e.g., 4 μL in 1 mL).
4) Add cells to dye, mix by pipetting, and incubate for 2-5 min (inverting tube periodically).
5) Add equal volume (e.g., 2 mL) of serum or 1% BSA; incubate 1 min.
6) Add equal volume of complete medium (e.g., 4 mL), and centrifuge 10 min.
7) Transfer cell pellet to new tube for further washing with complete medium, 3x.

Comments:
Uniformity of cell staining may vary; some cells (e.g., fibroblasts) may be very spotty.

C.3.3 SNARF-1 (Molecular Probes):

Background:

- Excitation/Emission Max = 488-530/580&640.
- pH indicator if fluorescence emission monitored at two wavelengths.
- Succininudyl ester and thiol-reactive acetate are designed for long-term cellular retention.
- MW = 592.56 (carboxylic acid, acetate, succinimidyl ester) – S22801.

Procedure:

1) Stock is typically prepared at 1-10 mM in DMSO.
    a. stored at –20 °C, in single-use aliquots ONLY!
    b. 50 μg means resuspend in 8.4-84.3 μL and then add 1 μL of dye to 1 mL cells for 10-1 μM final concentration, respectively
2) Literature reports 10-60 min incubation at 1-20 μM in serum-free medium.
3) May use Pluronic F-127 to promote dispersion of SNARF (very nonpolar) in buffers.

GREEN DYES

C.3.4 CMFDA (Molecular Probes):

Same as CMTMR except that it does require enzymatic cleavage to activate fluorescence.

Background:
Excitation/Emission Max = (?)
MW = 464.86

Procedure:

1) Prepare stock at 1-10 mM (1 mg/mL gives 2.15 mM).
2) Final usage is 1-20 μM.
    a. for sensitive cells dilute 1:10, then use 2-4 μL of this per mL (per 10M cells). [~0.5-1 μM final]
    b. for bright staining use 2-4 μL directly

Comments:
Photobleaching, of course, but quite reasonable if doing confocal (not epifluorescence) imaging.

C.3.5 CFSE (Molecular Probes):

Background:
CellTrace Proliferation Kit: C34554 ($98)
CFDA, SE (5,6) C1157 ($164, 25 mg)
Excitation/Emission Max = 492/517 nm; MW = 557.
For long-term exps., 5-10 uM dye recommended.
Should be visible for 8 divisions on flow cytometer.
Remains associated with apoptotic cells for a few days.
Can't be measured directly after labeling because of the extremely high fluorescence, unless use 0.625-1.25 uM. (Most CFSE taken up at first is not stably incorporated.)

Protocol 1: Kit

Make 5 mM stock using one vial and 18 uL DMSO.
Suspend cells in warm PBS/0.1% BSA at 1M cells/mL.
Add 2 uL stock/mL cells for a 10 uM concentration (0.5-25 uM typical).
Incubate at 37 C for 10 min.
Quench staining with 5 volumes ice-cold culture medium: incubate 5 min on ice.
Pellet cells, resuspend in fresh medium; repeat 2x.

Protocol 2: Kit, Alternate Method (ensure complete probe modification)

Dilute 5 mM CFSE in warm PBS (or other) to working concentration (0.5-25 uM).

Resuspend cells in PBS/CFSE directly; incubate 15 min at 37 C.
Pellet cells, resuspend in fresh warm medium: incubate 30 min.
Wash cells again.

Protocol 3: Current Protocols Method for High Cell Numbers (Unit 4.9)

Prepare 50 M cells/mL in HBSS.
Dilute a 5 mM CFSE stock 1:100 in PBS → 50 uM solution.
Add 110 uL CFSE/mL cells for 5 uM concentration. (Strategy for addition: put drop of CFSE on non-wetted part of conical while holding horizontally; rapidly invert.)
Incubate 5 min at RT.
Add 10 volumes PBS/5% FCS and pellet cells (at RT!): wash 3x.
Harvesting: wash in 3 mL PBS, resuspend in 150 uL 0.5 mM EDTA/PBS, incubate 5 min at 37 C to dissociate aggregates; centrifuge, resuspend in PBS/5% FCS for FACS.

Protocol 4: Current Protocols Method for Low Cell Numbers (Unit 4.9)

Prepare 0.5-10 M cells/mL in PBS/5% FCS; otherwise same.

Comments:
Have gotten cell death (~ 50%) before with all protocols.

FAR RED DYES

C.3.6 DDAO (Molecular Probes):

Background:

- Ex/Em Max = ~ 600-650 (broad); ~ 665

Procedure: As for CFSE.

VARIOUS

C.3.7 fura-2 AM (Molecular Probes)

Background:

- Ex Max: 335 at high conc. Ca^{++}, 363 at low conc. Ca^{++} (ratiometric dye).
- Em. Max: ~ 505-515
- MW = 1002

Procedure:

1) Stock typically prepared at 1 mg/mL = 1 mM in DMSO.

2) Typical usage at 0.1-5 μM. For example:
    a. Add 0.1 mL cells to 2.5 μL fura/0.9 mL serum-free medium.
    b. After 25 min, wash 2-3x in complete medium.

C.3.8 DiDyes (Molecular Probes)

Background:

- Info here is for the readily cell-loadable ones. Also have DiI, DiD, DiO, DiA, DiR, Ph.
- Ex/Em Max = 497/513 SP-DiO; 556/573 SP-DiI; 555/570 DiI(3)-DS
- MW = 993.54 Di(3)-DS; 1145.73 SP-DiI; 1115.55 SP-DiO.
- Sulfonated derivates may be stored at RT for 6 months.

Procedure:

1) Stock is typically 1-2 mg/mL in DMF, DMSO, or ethanol. [DMF for SP-DiO.]
2) Dilute in HBSS or D-PBS at 1-2 μM for working concentration. (~1μL/mL.)
3) Incubate cells for <=5 min at 37C, then 15 min at 4C.
4) Wash with PBS, resuspend in fresh medium.

Appendix D Peptide/Protein Modifications

D.1 Acrylation of co-polymerization materials

D.1.1 Peptide acrylation:

Materials:

Reaction buffer: 0.1M $NaHCO_3$ (MW 84.01), 0.5 M NaCl at pH 8.3

Acryloyl-PEG-N-hydroxysuccinimide ester (NHS-PEGA) at MW 3400. (Previously from Nektar Therapeutics, now sold by Laysan Bio, Inc.)

Peptides used in the past:

adhesion – GWG**RGDSP** (MW 830.9)
enzyme-sensitive – GWG**LGPA**GK (MW 842.0)

Procedure:

1. Peptide is dissolved in reaction buffer in a small scintillation vial with stir bar.
    a. The final concentration will be 5 mg/mL of *peptide* (taking into account that it is only 75% pure). Initially it is dissolved in a smaller volume, reserving 1-1.5 mL for dissolution of the Acrl-PEG-NHS.
2. Acrl-PEG-NHS is prepared at 0-50% molar excess with respect to the peptide.
    a. Stored frozen, the closed bottle should be moved to RT a few minutes prior to use to equilibrate and thus minimize water contamination
    b. The powder should be dissolved at the last minute in ~ 1 mL of buffer, by vortexing in an eppendorf tube.
3. The Acrl-PEG-NHS solution is added dropwise to the stirring peptide solution.
4. Stir for 2-3 hours.
5. Dialyze mixture in a 3500MW cassette from Pierce, while changing the deionized water two times, including one overnight soak.

Sample Calculation: 40 mg protein (775 MW) in 5 mL; add 0.1976 g PEG-NHS in 1 mL. Note: If both sides of the peptide will undergo reaction (as with the lysine-APGL construct), the amount of NHS-PEGA must be doubled.

Assay to confirm reaction:

The peptide-PEG conjugate may be tested on the UV-vis spectrophotometer: the final ratio of absorbance at 280:260 nm should be ~ 0.60-65 (*not* so high as 0.8) for a single PEG tether on the peptide. For PEG-peptide-PEG materials, the absorbance ratio may remain higher.

D.1.2 Biocytin acrylation:

Materials:

EZ-link biocytin from Pierce (MW 372.5)

Procedure:

Basically the same as peptide acrylation. Briefly:

1. Biocytin is reacted with NHS-PEGA.
    a. Use 1-1.33 moles NHS-PEG-A: 1 mole biocytin.
2. React 2-3 h at room temperature, with stirring.
3. Dialyze 1 h
    a. in 3500 MW cutoff cassette (Pierce) if used excess NHS-PEGA.
    b. in 500 MW cutoff tube (Spectrum Laboratories) if used even ratio.
4. Filter and freeze solution, lyophylize overnight.
5. Resuspend in buffer at, e.g., 40 mg/mL – freeze aliquots at –20 °C.

Note: Aliquots are good for at least a month when thawed and left at 4 °C.

D.2 Protein tagging

D.2.1 Background on proteins

- Fibronectin (FN)
    - from bovine plasma
    - MW 450 KDa
    - Sigma product #F 4759
    - reconstitution in water results in Tris buffer.
- Laminin (LMN)
    - from Engelbreth-Holm-Swarm murine sarcoma
    - MW 810 KDa
    - Sigma product #L 2020
    - supplied in Tris pH 7.5 buffer with 150 mM NaCl
- ICAM-1
    - recombinant protein
    - MW 77 KDa (120 under reducing conditions)
    - lyophilized with 50 mM Tris-citrate, 2 mM $CaCl_2$, pH 6.2.

D.2.2 Fluorescent labeling

Use Fluorescein (or FITC, Rhodamine) labeling kit from Pierce Biotechnology. The kit is worth the money because it includes 1 mg pre-weighed vials of the label.

1. For ideal labeling, dialyze protein into BupH Borate buffer (pH 8.5), with 0.05-1 mL protein at 1-10 mg/mL.
    a. e.g., use Pierce dialysis cups (3500 MW cutoff)
    b. dialyze 1 h at RT in 500 mL buffer
2. 24-fold molar excess of dye is ideal (MW NHS-fluorescein = 473.4); they suggest dissolving NHS-fluorescein as 1 mg in 100 μL DMF: react for 1 h at RT.
3. For < 100 μL, use slide-a-lyzer with > 100 mL PBS: 1 h at RT.
4. For large volumes, using desalting column is recommended.
    a. wash column with 25 mL PBS; use no > 1 mL sample per one column.
    b. add 0.5 mL sample, PBS aliquots until no protein runs through.

D.2.3 Biotinylation of mg level of protein

Kit does not come with pre-weighed vials – not worth it – order reagent directly.

Mutiple options available – I usually used the longest linker (LC-LC):
MW Sulfo-NHS-LC-biotin = 557
MW Sulfo-NHS-LC-LC-biotin = 669.75

1. Recommended buffer is BupH PBS, with 2-10 mg/mL protein.
2. 12-fold (10 mg/mL) or 20-fold (2 mg/mL) excess of sulfo-NHS-biotin is recommended for incorporating 3-5 biotin per protein molecule; they suggest dissolving 2 mg biotin in 100 μL ultrapure water, but 1 mL usually works better for my protein etc amounts.
3. React for 2 h on ice or 30 min at RT.
4. Desalting is recommended purification method:
    a. equilibrate 10 mL column with 30 mL PBS.
    b. apply sample in 0.5-1 mL aliquots: collect.
    c. pool protein-containing fractions from testing 280 nm absorbance.

Note: Despite desalting being recommended, dialysis seems to work fine. The advantage of dialysis is that there is no need to re-concentrate the protein afterward.

D.2.4 Simultaneous labeling with biotin and fluorophore

Adding NHS-fluorescein and sulfo-NHS-biotin at the same time is probably best. However, adding a fluorophore will inevitably change the degree of biotin labeling. We have found it difficult to make double-labeled proteins that work well thus far.

D.2.5 Biotinylation of small quantities (< 100 μg) of protein

Materials:

Biotin-XX Microscale Protein Labeling Kit (B30010, Molecular Probes).
(Sold together with biotin assay as B30756.)

Procedure:

Preparation, first time only:

- Prepare 1 M $NaHCO_3$: 1 mL deionized water + vial
  - store the rest in fridge for two weeks, or freeze for long-term use.

Biotinylation, each time:

1. Prepare protein at 1 mg/mL in PBS.
   a. e.g., 50 μg of ICAM-1 = 50 μL resuspension in water
   b. ICAM-1 lyophilized in Tris, so must be dialyzed into PBS
2. Optional desalting using ElutaTube microdialysis vials
   a. Fill wth 200 μL deionized water, hydrate > 5 min at RT
   b. Dialyze in 500 mL for 0.5 h at RT, then 1.5 h at 4 °C.
   c. Repeat 3 times (at 4 °C whole time).
3. Transfer protein to reaction tube (e.g., 50 μL), add 1/10 volume of $NaHCO_3$ (e.g., 5 μL).
4. Add 10 μL DI water to vial of reactive biotin and add immediately to rxn. tube.
   a. amount for ICAM-1 labeling: 0.65 μL
5. Incubate 15 min at RT.

Purification, each time:

1. Gently rock gel resin (Component E) to resuspend.
2. Fill spin filter to lip with gel resin (c. 800 μL).
3. Centrifuge at 16000 g for 15 sec (including run-up time).
4. See figures for appropriate resin amount; correct as necessary.
   a. rinse collection tube with buffer if resin has gotten in there.
   b. to exchange buffer, centrifuge through bed at low speed a few times.
5. Place up to 50 μL rxn. onto center of resin bed.
6. Centrifuge for total of 1 min at 16000 g (high side of resin on outside).

Appendix E Scaffold preparation and analysis

E.1 Scaffold fabrication

E.1.1 Protocol for making templates

Materials:

- Low polydispersity poly(methyl methacrylate) (PMMA) particles from Fluka (via Sigma-Aldrich).

Size (μm)	20	40	60	80
Catalogue #	90549	84657	77006	90544

- Kit for preparing poly(dimethyl siloxane) – e.g., Sylgard 184 silicone elastomer kit.
- Annular cutting tool (4.5 mm diameter, ~4 mm height) from MIT Machine Shop.
- Shaker with 3/8 inch orbit from IKA or Labline.

Procedure:

1. Mix ~15:1 (base:curing agent) of the two-part PDMS kit and pour into petri dish. Per 10 cm Petri dish, use about ~12 mL of solution (makes c. 20 cut-outs).
2. Let bubbles settle at ambient conditions 1-2 h (or rid in vacuum oven for 20-30 min), then leave on top of glassware oven O/N. (Allow to cool briefly on next day.)
3. Use annular cutting tool to make hole and razor blade to cut out surrounding square area to make walls for a well; stick wells onto coverslips.
4. Arrange and tape down coverslips on the shaker when ready to make templates.
5. Sphere preparation: centrifuge 10 wt% solids solutions for 2 min/2000 rpm, resuspend in 70% ethanol at 55-65 wt %.
6. Add 15-30 μL of resuspended PMMA microspheres per well. Cover with a taped down Petri dish to slow the rate of evaporation. Turn shaker on 350-450 rpm.
7. Once the spheres are partly but not completely dry (~ 10-15 min), turn off shaker and add another 15-30 μL of PMMA solution. Turn shaker back on.
8. Repeat step 5 again if desired. In total, wells should receive ~ 50 μL each.
9. This time, let scaffolds shaker until completely dry (2-4 h).
10. Check under microscope for how well they have ordered.
11. For scaffolds that are not well ordered enough, resuspend microspheres with 70% ethanol directly in the well (~ 30 μL), and shake again (2-4 h).
12. Most scaffolds should now be well ordered (except for slight disorder in the very center, often) but can be resuspended again if not.

Note: Larger sphere sizes (40-80 μm) only need lower level shaking (350-450), while smaller sphere sizes (20-30 μm) need higher level shaking (450-500). Further, smaller spheres typically need to be more concentrated to order well.

E.1.2 Protocol for making polymer scaffolds

Prepolymer solution stocks and other materials required:

- Fluor 570 = methacryloxethyl thiocarbonyl rhodamine
  - Polysciences, Inc # 23591
- HBS = HEPES-buffered saline (see Appendix A)
- HPK = 1-hydroxy-cyclohexylphenylketone
- PEGDMA = poly(ethylene glycol)-dimethacrylate, 1000 Da
- TEOA = triethanolamine

Buffer stock: 20μL (0.0224g) TEOA per mL HBS.
Initiator stock: 0.2g HPK per mL 70% ethanol (make fresh!)

Optional:
Fluor 570 stock: 0.1% w/v aqueous.
Biotin-PEGA
Peptide-PEGA

Alternative initiator:
DMPA = 2,2-dimethyl-2-phenyl-acetophenone

Procedure:

1. Weigh semi-solid PEG, add to the HBS/TEOA, and vortex to dissolve.
2. Add ethanol, any optional components, and finally the initiator.
3. Filter the solution through a 0.2 μm filter (e.g., Acrodisc from Pall corporation).
4. Add 8-12 μL prepolymer solution to an edge of the template.
5. Centrifuge 3 min. at 1500 rpm. It should look slightly wet but not overly so. If it looks dry, add 1-2 μL more of pre-polymer solution and wait 10-20 sec.
6. Expose to UV light for 90 seconds, immediately transfer construct to acetic acid.
7. Exchange process: change acetic acid after 2-4 hours (1x), next day (3x), third day (1x), then to PBS (3-4x over 24 h), sterile PBS (1x), dip into 70% ethanol, sterile PBS (2-3x over 24h and long-term storage). All at ~ 8 mL/scaffold.

Note: on first acetic acid exchange, remove scaffolds from the PDMS well/coverslip. Removing them at this time reduces tearing because they are swollen rather than slightly dry.

Recipes:

Base recipe: 0.2 g PEGDMA per 1 mL of 3:1 buffer stock:ethanol, 40 μL initiator stock.

Fluorescent recipe: add 30 μL Fluor 570 stock per 1 mL base recipe (0.003 wt % final).

Peptide recipe: 160:1 PEGDMA:RGD-PEGA molar ratio is typical (e.g., 240 uL per 1 mL prepolymer solution buffer when using 0.03 g/mL stock peptide solution.)

Biotin-containing recipe: 1:500 by moles means ~0.0018 g bio-PEGA per 0.2 g PEGDMA, or ~ 40 μL stock solution per mL prepolymer.

COOH-containing recipe: add up to 2 uL MAA to base recipe – *post-processing differs.*

E.1.3 Protocol for protein conjugation to scaffolds

Procedure for biotinylated scaffolds:

All steps should be done 4 °C, while shaking gently (100-200 rpm).

1. Per scaffold, add 1 mL of 1 μg/mL of SAv (with or without a conjugated fluorophore such as Alexa-647) in PBS. Incubate 12-24 h.
2. Wash with 1.5 mL PBS (3+ exchanges over 12-24 h).
3. Add 5-20 μg/mL protein in PBS. Incubate 12-24 h.
4. Wash with 1.5 mL PBS (3+ exchanges) for 4-6 h.

This procedure was used for most experiments described in the main document.

Procedure for MAA-containing scaffolds – aqueous:

Activation buffer: 0.1 M MES, 0.5 M NaCl, pH 6.0
Alternative: pH 5 MES for step 1; pH 7-8.5 phosphate or carbonate buffer for step 2.
MW NHS = 115.09; MW EDC = 191.7 g/mol.

1. Equilibrate EDC and NHS to RT before opening.
2. React scaffold with 2 mM EDC and 5 mM NHS for 30-45 min. (per mL: 0.4 mg EDC, 0.6 mg NHS, 1.1 mg sulfo-NHS – prep 10 mL or more.)
3. Add 20 mM 2-mercaptoethanol (1.4 μL per mL); wait 5 min.
4. Add protein (conc.?) and react for 2-3 h at RT.
5. (May quench by adding hydroxylamine to 10 mM.)

This procedure was tested as an alternative for making protein-coated scaffolds. It appeared to result in weak protein attachment; however, studies were not exhaustive.

Procedure for MAA-containing scaffolds – organic:

MW NHS = 115.09; MW DCC = 206.33 g/mol.

1. Equilibrate scaffolds in DCM.
2. Replace DCM with rxn mixture: 27.4 mM each of NHS, DCC in DCM.. (Per 10 mL: 0.0315 g NHS, 0.0565 g DCC; this is 3x of Darrell's old recipe.)
3. React for 8 h – overnight at RT.

4. Rinse with DCM several times.
5. Briefly equilibrate with DMSO, (75/25 DMSO/PBS), 50/50 DMSO PBS.
6. Add about 1 mL of 10 μg/mL protein to each scaffold: react 2-3 h at RT.

This procedure was tested as yet another alternative. Protein attachment seemed to work quite well; however, removal of all organic solvent and chemical precipitates was difficult.

E.1.4 Protocol for making attached scaffolds surrounded with bulk gel

Glass Preparation:

1. Dip round (imaging) coverslips in trichlorovinylsilane (4 wt. % in methanol).
2. Incubate 20 min.
3. Rinse slides thoroughly with methanol (and optionally, water).
4. Put slides in vacuum oven, turn off the vacuum once pressure gauge hits 30, then leave slides in that atmosphere for 30-60 min.
5. Note: flush silane with nitrogen before putting it back into chemical fridge.

Scaffold Preparation/Treatment:

1. Prepare a square-shaped PDMS well that is large enough to surround the (round) template with a bit of room to spare all around.
2. Add pre-polymer to a template prepared on a normal coverslip and photopolymerize for 30 seconds.
3. Meanwhile, spincoat a thin layer of pre-polymer onto a silanized coverslip at low speed.
4. Slice off template-polymer composite using a razor, remove its surrounding (round) PDMS well, and place it onto the silanized coverslip. Polymerize for 30 seconds more.
5. Set the square PDMS well down around the template, add 70-100 μL of pre-polymer solution (gently, so as not to disturb/lift off the template), and polymerize for a final 30 seconds.
6. Wash with acetic acid as usual, then transfer to DCM and continue with protein attachment protocol as for MAA scaffolds in organic solution. This method results in the most stable removal of PMMA and attachment of protein.
7. Cells can be injected into attached scaffolds, which results in excellent packing. However, trace DCM can result in cell death. Further, about half of the scaffolds may detach from the silanized coverslip after undergoing all of the washing steps. This method is thus ultimately inefficient and undesirable.

E.2 Supplementary assays for proteins attached to scaffolds

E.2.1 Scaffold immunostaining:

Procedure:

All steps should be done at 4 °C for 12-24 h, while shaking gently (100-200 rpm).

1. Incubate scaffold with 0.5 mL antibody diluted to 1-10 μg/mL (in FACS buffer).
2. Rinse 3x in quick succession, then soak in FACS buffer.
3. Rinse 3x in quick succession prior to imaging or addition of next reagent.
4. Repeat for secondary step(s) as necessary.

Specific antibodies:

Anti-fibronectin (250 μg/mL) L.
Secondary antibodies (2 mg/mL) at 1:500
FITC ICAM-1 Ig (500 μg/mL) diluted 1:50.

E.2.2 Determining protein concentration with microBCA assay:

Objective: Calculate protein concentration of modified (biotinylated) proteins after processing/dialysis in order to get accurate value of biotin groups per protein.

Materials:

- MicroBCA kit (Pierce 23235)
- PBS or other appropriate diluent
- Protein to be tested
- (Protein standard)

Procedure (test tube → UV-vis spectrophotometer):

1) Pre-heat water bath in large crystallizing dish to 60 °C.
    a. use combination heater/stirplate, on low stir speed (100-200 rpm)
2) Prepare protein samples and standards at 2x final concentration 0.8-1 mL each).
    a. include a blank (no protein) sample
    b. they recommend using BSA as a standard (final conc. 0.5-200 μg/mL)
3) Prepare Pierce working reagent (WR) at 25:24:1 ratio of kit components MA:MB:MC.
    a. prepare enough to mix 1:1 with each protein sample or standard
    b. final volume should be 1.6-2 mL, to adequately fill disposable UV cuvettes
4) Mix each protein sample/standard with an equal volume of WR, mix well.
5) Incubate tubes in water bath for 1 h.
6) Cool tubes to RT (e.g., immerse in RT/cool water repeatedly).
7) Tare spectrophotometer on cuvette filled with water, at 562 nm.
8) Measure absorbance of each sample at 562 nm, ideally within 10 minutes.

Analysis:

- Subract the blank (no protein) reading from all samples/standards.
- Prepare a standard curve from the protein standard values.
- Use the curve-fit (linear) to determine the protein sample concentrations.

Notes:

- This procedure may also be done on a microplate reader (see Pierce documentation if interested); however, the detection limit is less sensitive.
- BSA concentration does not necessarily correlate well with the concentration of another protein. For example, ICAM-1 has a higher absorbance, and can be used at even lower concentrations as a standard (e.g., 0.25, 0.5, 1, 2 μg/mL)
- The cuvettes do sometimes vary by a few thousandths absorbance units in their baseline readings.
    - For rapid but accurate testing, I usually do the following:
        - Fill first cuvette with water, measure absorbance.
        - Transfer water to next cuvette in the box.
        - Fill first cuvette with sample, measure, and set aside (in case of error).
        - Measure baseline of second cuvette.
        - Repeat for all samples…
    - Perform all solution transfers with disposable glass pipets, keeping a box nearby.
    - Keep extra water nearby, as the level will eventually lower after many transfers.

E.2.3 HABA protocol for biotin content

Objective: Measure biotin groups on protein when don't need a supersensitive assay (e.g., used this for measuring biotin groups on fibronectin).

Method: Biotin displaces HABA from avidin, decreasing absorption at 500 nm.

Materials:

Buffer: PBS (or TBS if desired)
Avidin (Pierce): usually we keep stock at 2 mg/mL.
HABA (Pierce): available in kit or sold separately as a powder.

Prep HABA/Avidin solution: 1 mg Avidin + 60 μL HABA + 1.94 mL PBS is basis.
e.g., 500 μL Avidin, 60 μL HABA, 1.44 mL PBS if use normal Avidin stock.
Stable for 2 weeks in fridge – may filter if precipitate forms.

Procedure:

1. Test H/A solution: should have A_{500} = 0.9-1.3 = reading 1 = R1.
2. Add biotinylated protein to the same cuvette: mix and get A_{500} = R2.
    a. wait for value to be constant >15 sec
    b. if sample is absorbance is <0.3, dilute and repeat the assay
3. Junsang recommends always making a standard curve with free biotin!!!
    a. 1 mM stock = 0.244 mg/mL stock (JSD has in PBS pH 6.0)
    b. use b/w c. 0.2 and 5 μg/mL curve = 50x dilution on down
4. If using cuvettes, *dry thoroughly* in between samples.

Calculation:

Abs = $\varepsilon\ l\ C$ (l = 1 cm for most cuvettes)
ε = 34000 mL/($M^{-1}cm^{-1}$) for H/A

1. Calculate mmoles protein/mL = conc (mg/mL) / MW
   e.g., 3 mg/mL 450 KDa FN → 6.666 e-6 mmole/mL
   e.g., 1 mg/mL 890 KDa LMN → 1.235 e-6 mmole/mL

2. Calculate change in absorbance, accounting for dilution
   - e.g., 10x diluted protein means delta A = 0.9 R1 – R2
     - because C_{HABA}-2 is 0.9 of C_{HABA}-1
   - I usually use 488 buffer + 12.5 μL protein solution
     - equation is thus 0.975 R1 – R2

3. Calculate biotin concentration (mmole/mL)
   C = ΔA/34000

4. Calculate mmoles biotin/mmoles protein
   - e.g., for 10x diluted protein: C3/C1 * 10
   - For my typical case, multiply by 40 (dilution factor) instead.

E.2.4 Determining biotin content on small amounts of protein

Objective: measure biotin on small amounts of expensive protein (e.g., ICAM-1).

FluoReporter biotin quantitation kit (F30751, Molecular Probes).
Ex/Em = 495/519.

Requires estimate of protein concentration:

1. Simplest determination = mg protein x % yield / volume (mL) recovered
   a. assume 79-95% recovery for protein with ICAM-1 MW
2. Better alternative: A280 of conjugate soln. vs. 1 mg/mL soln. of protein alone.
3. Best alternative: Protein assay kit (Q33210) – requires 5 µL.

Procedure:

96-well microplate format.

Requires 600 ng of singly biotinylated IgG; lower MW or >1 biotin requires less protein.
Detects 4-80 pmol biotin (50-fold higher sensitivity cf. HABA assay).

1. Allow components to come to RT before opening.

2. Add 1 mL of provided 10X PBS to 9 mL DI water (per two assays).
3. Add 1.75 mL PBS to Biotective Green (Comp. A).
    a. may be refrigerated for up to 5 days.
4. If needed, reconstitute protease (Comp. C) in 50 μL PBS.
    a. may be aliquotted and frozen.
5. Optional protease digestion.
    a. dilute bio-protein in PBS to 50 μL.
    b. add 1 μL protease stock soln.
    c. digest IgG as a positive control: 3 μL + 154 μL PBS + 3 μL protease.
    d. incubate O/N at 37 °C.
6. Biocytin standard: 843 μL PBS + 6.8 μL biocytin (Comp. B).
    a. serial dilution in triplicate (+ PBS alone as neg. control), 50 μL each.
7. Dilute bio-protein in PBS – e.g., assume 1-20 degree of labeling.
8. Add 50 μL of bio-protein samples, pos. controls to appropriate wells.
9. Add 50 μL Biotective Green reagen to each well; incubate 5 min at RT.
10. Measure on fluorescence reader (c. 485/530) within 15 min.

Analysis:

Plot fluorescence (x) vs. amount of biocytin (y).
Use quadratic fit, or straight line fit through two bracketing values.

DOL of positive control(s) varies from lot to lot; should get within 0.5 of value.

Note: biocytin is a good control for proteolytically cleaved biotin; goat IgG also provided.

Appendix F Experiments in 2D (no scaffolds)

F.1.1 Protocols for protein surface preparation

Objective: Prepare surfaces to test cell spreading and/or sticking to various ECM components. Also used to prepare surfaces for testing cell migration in the presence of chemokine.

Materials:

- 1% BSA in PBS, or blocking buffer
  - used as negative control, and post-treatment block.
- Adhesion protein of interest

Procedures for protein preparation:

- Initial prep for various ECM proteins.
  - Fibronectin (Sigma F4759): 1 mg/mL in water, dissolve 30$^+$ min at 37 °C, store aliquots in freezer.
  - Laminin (mouse, Sigma L2020): slowly thaw in fridge (from freezer).
  - ICAM-1, VCAM-1 (recombinant, R&D systems)
  - Laminin (human,):
  - CN I, III from calf skin: 1 mg/mL dissolution in pH 3 aq. AA (0.25%).
  - CN IV (Sigma C0543): 1 mg/mL dissolution in pH 3 aq. AA.
  - CN IV – gel: 1.5-3 mg/mL dissolution in pH 3 water/AA;.
  - Vitrogen CN I – gel: std. 9:1 procedure; 60 min gel, best w/out CO_2.
  - Vitrogen CN I: film same as gel, but dry it out, rehydrate with sterile H_2O.

Procedure for protein coating:

- Dilute protein in SF-RPMI or HBSS
  - Laminin (mouse): incubate at 2 μg/cm^2.
  - Fibronectin (Sigma F4759): 5 μg/cm^2, air dry 45 min at RT, rinse if desired.
  - ICAM-1, VCAM-1: dilute to 10 μg/mL in PBS, incubate at 4 °C O/N.
  - CN I, III from calf skin: incubate at 10 μg/cm^2.
  - CN IV (Sigma C0543): incubate at 10 μg/cm^2 for a few hrs at RT or 37 °C; dry O/N.
  - CN IV – gel: std. 9:1 CN: 10x medium/$NaHCO_3$ procedure, with CN pH to 7.4, then gel 20-40 min.
- For testing cell specific adhesion on ECM-treated plates, must use serum-free medium.
- After incubation time (1-3 h), can rinse cells with warm serum-free medium, and gently turn over/blot plate to test strength of cell adhesion.
- Cells may be observed by optical microscopy, and/or fluorescence if labeled.

Notes:

For sample calculations, see for example notebook page III.133.

BD Biosciences CN I: perfect results with 800 uL CN + 40 uL 0.1M NaOH + 110 uL (slightly basic) 10x medium. Sigma CN IV: perfect results with 8:1:1 mix.

24-well plate has ~ 1.54 cm^2 per well surface area.
8-well Lab-Tek has ~0.7-0.8 cm^2 per well surface area.

F.1.2 2D Chemokinesis Experiments:

Chamber Preparation:

Coat Lab-Tek chambers with fibronectin (may be done same day), or ICAM-1 or VCAM-1 (overnight procedure). See Appendix F.1.1.

Cell Preparation:

1) Prepare cell suspension from spleen and/or lymph nodes of young mouse.
    a. (If using splenocytes, first lyse red blood cells.)
2) Perform MACS according to manufacturer's protocol.
3) Label ~ 40% of cells with fura-2 AM or CMFDA (see Appendix C.3).
4) Add chemokine to final cell resuspension (e.g., 1-5 μg/mL), allow to equilibrate 5-20 min on the microscope, and begin imaging.

Imaging:

Typically do hour-long runs at 30-second intervals in four quadrants.
Positive chemokine concentrations are ~ 1*-5 μg/mL.
* Previous CK reconstitution was calculated incorrectly: really was using 2.5 μg/mL.

Note: Be sure to note age (and sex) of mouse!!!

F.1.3 Protocol for chemokine stability testing

Overview:

To assess chemokine (CK) stability, diluted CK solutions are prepared at staggered intervals, and interrogated by ELISA on the same day.

Sample dilutions:

1. For CCL21 at 2000 and 200 ng/mL: 1.5 µL of 100 µg/mL CCL21 in 75 µL, and 1.5 µL of 1:10 CCL21 dilution.
2. Test (for example) CCL21 in RPMI-10 and 1% BSA at 37 °C with shaking.
3. Final dilutions for ELISA should be about 1:4000 and 1:400, respectively. (12.5 µL of 1:100 or 1:10 in 0.5 mL of Reagent Diluent).
4. Previous testing was done for 2h, 1d, 2d, and 5 d before the ELISA was performed.

F.1.4 Chemotaxis filterplate assay method

Adapted from Dr. Richard Colvin

Preparation:

- Cell number: ~ 25000 cells on top often good; aim for 500-600 coming through.
- Volumes: bottom = 31, top = 25-50 uL.
- Perform chemotaxis assay at 37 C for c. 2 hours (primary cells).

Assay:

1) hold plate at angle and rinse off top with distilled water, to wash away cells.
2) spin for 5 min/1500 rpm.
3) remove top (break seal at two points w/spatula, open like a hinge).
4) aspirate supernatant, quickly moving from center-bottom of each well to next well; leave behind 5-10 uL.
5) leave at –80 C O/N (or less long; O/N usually most convenient)
6) use cyquant (C7026) – A(1:400) + B(1:30); may want to double B or add other detergents, depending on signal. use ~ 2 mL/plate (20 uL.well); incubate 2-5 h.
7) read on fluorescence plate reader (485/520).

Controls:

- cyquant alone for background
- cell calibration curve: ~ 100K, doubling dilutions downward (10 uL).

Appendix G Scaffold-cell integration

G.1 Cell loading

G.1.1 Cell loading, general (medium):

1. Put scaffold in 96-well round-bottom plate, with scaffold flatter side up.
2. Add 10 μL cells on top, incubate 3 min at 37 °C.
3. Spin for 1 min at 800 rpm.
4. Repeat steps 2-3 one or more times as needed.
5. Dip scaffold in 200 μL fresh warm medium to remove surface cells.
6. Place gently in Lab-Tek filled with 100-150 μL medium.
    a. alternatively, place in POC chamber (Zeiss), surround with 100-150 μL medium, and close chamber by adding second coverslip and metal cover.
7. Image scaffold/cells; remove some medium if scaffold floats.
8. Add more medium (100+ μL) for long term culture.

G.1.2 Cell loading, general (collagen):

1) Put scaffold in 96-well round-bottom plate, with scaffold flatter side up.
2) Add 10 μL cells on top, incubate 3 min at 4 °C.
3) Spin for 1 min at 800 rpm.
4) Repeat steps 2-3 one or more times as needed.
5) Place scaffold gently in Lab-Tek chamber.
6) Surround with 60-100 μL collagen.
7) Add more medium (100+ μL) for long term culture.

G.1.3 Fibroblast (e.g., BLS4) cell loading:

Note: to get good loading of BLS4 in scaffolds without clumping, it is important to do extended EDTA treatment prior to trypsinization.

1. Warm all components to 37 °C prior to use.
2. Aspirate cell medium and rinse cells briefly with warm PBS.
3. Aspirate PBS, add 3 parts EDTA (0.02 % solution).
4. Incubate 10 min.
5. Leave EDTA there, and add 1 part trypsin/EDTA (0.25% / 2.21 mM).
6. Incubate 2-5 min, then ads 10 mL complete medium.
7. Wash, count, and resuspend cells.
8. Add 500K or fewer cells per scaffold, added in ~ 20 μL as usual.

G.2 Cell migration experiments

G.2.1 T cell migration in protein-coated scaffolds

1) Protein-coated scaffolds should be prepared ahead of time according to Appendix E.1.3, and washed several times in PBS the morning of the experiment.
2) Meanwhile, naïve T cells should be prepared according to Appendix C.2.2, or activated T cells should be removed from culture well plates by pipetting and counted.
3) The selected T cells should be labeled with CMFDA (see Appendix C.3.4) or other appropriate fluorescent dye.
4) Finally, the cells should be loaded into the scaffold as described in Appendix G.1 (~500M cells/mL).
    a. For experiments where soluble CCL21 is added, the final concentration must be taken into account. For example, CCL21 must be added to a 10 μL cell suspension at 20 μg/mL for a final concentration of 2 μg/mL in 100 μL.
5) Cells may be imaged immediately or after a delay following incubation. Typically, intervals of 30 sec and total imaging times of 0.5-3 h were used.

G.2.2 T cell migration in composite scaffolds

As described in Appendix above, but with the following modifications:

1) Composite scaffolds may not necessarily contain any coating proteins.
2) Cells should be loaded at 4 °C.

Appendix H GENERAL SUPPORT ASSAYS

H.1 Flow Cytometry

H.1.1 Flow cytometry general protocol:

Note: this method is designed for the simplest calculations and quickest procedure possible, without compromising results. Once the method is familiar, it should only take ~ 45-50 minutes per staining step, plus initial time to retrieve and count cells.

Reagents:

- All antibody(Ab)/reagent dilutions may be performed in eppendorf tubes.
- All centrifuging may be done at the standard 5 min/1200 rpm.
- For multi-colour samples, need to prepare: sample (all Abs at once), single color controls (one antibody at a time), and an isotype control (all ITC Abs at once).
- FACS buffer: 1% BSA, 0.1% NaN3 in HBSS (or PBS is okay) pH 7.4.
- PI stock solution: 1 mg/mL
- final PI concentration: 1.25 μg/mL. To achieve this, add 5 μL of a 1:10 dilution of the PI stock solution per 400 μL of cells/FACS buffer.
- Final cell suspension: minimum 0.4 mL (100,000/mL); ideally ~ 500,000^{+}/mL.
- CD16/32 solution: prepare at 10 μg/mL (1:50) in FACS buffer just prior to use (i.e., while spinning down cells): prepare enough for 1 extra sample.
- FITC, biotin antibodies: typically are used at 10 μg/mL (1:25 for 2x stock).
- PE antibodies: typically are used at 2 μg/mL (1:50 for 2x stock).
- For antibodies, prepare 60 μL per cell sample (but add 50 μL), due to losses.
- For SAv conjugates, prepare enough for one extra sample.
- SAv-APC: typically used at 1:100; SAv-PE: typically used at 1:1000.
- Cychrome Abs, SAv-Cychrome similar to PE, but somewhat less bright.
- Spin Abs before using (0.5 min, 1000's of rpm, especially PE).

Preparation:

1. Count cells: you will typically use 10^5-10^6 cells per sample (e.g., 400,000).
2. Resuspend cells in FACS buffer, or in CD16/32 (diluted in FACS buffer): 50 μL per sample. Cells should be resuspended in ~ 10% excess volume due to losses.
3. Plate 50 μL of cells per sample well in a 96 v-bottom plate. Wait 10 min if doing Fc blocking (CD16/32) step. Otherwise proceed to step 4 immediately. Note: While waiting for Fc block (or spinning down cells), prepare antibody dilutions.
4. Add 50 μL of appropriately diluted antibodies (i.e., 2x the final desired dilution) to the cell samples. Note: CD16/32 does not need to be washed out first.
5. Incubate 20 min. over ice. Add 100 μL FACS buffer to each sample, and centrifuge. Check for cell pellets; flick buffer out by shaking plate over bio-trash.
6. Resuspend each sample in 200 μL; centrifuge, flick buffer out. Repeat.

7. If using secondary antibodies, resuspend cells directly in 100 μL of diluted secondary (or resuspend in 50 μL buffer, then add 50 μL secondary if desired). Repeat steps 5 and 6; or if only primary antibodies are used, proceed to step 8.
8. After the final (third) wash, resuspend the cells in 200 μL FACS buffer, and add them to individual FACS tubes containing 200-800 μL of FACS buffer or PI-containing FACS buffer (not if you are using Cychrome!), if desired.

H.1.2 Flow cytometry: specific antibodies and resulting data

FACS for Naïve T cell Determination

Background:

CD62L is highly expressed on naïve cells, and low on effectors (but high on memory). CD44 is upregulated on memory cells compared to naïve cells.

Notes/Calculations:

Ab	isotype	amount	2x stock
TCR-FITC	Ar Ham IgG2, L1	10 μg/mL	1:25
CD62L-PE	rat IgG2a,K	2 μg/mL	1:50
CD44-CyC	rat IgG2b,K	2 μg/mL	1:50

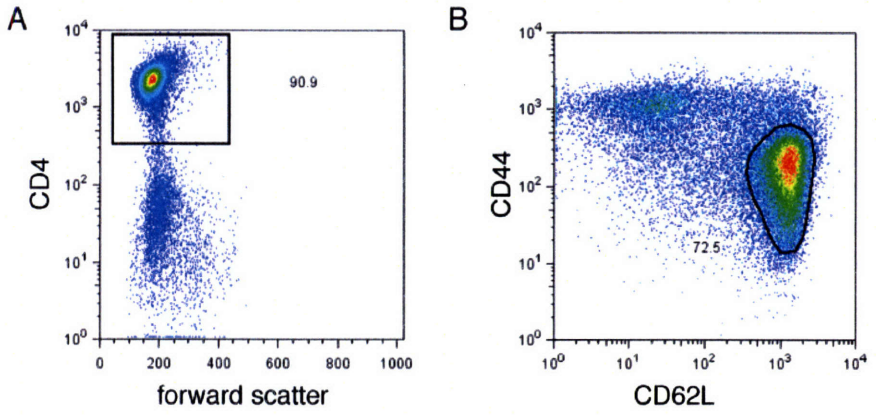

Figure A 1 **Phenotype of CD4$^+$ T cells obtained by magnetic sorting.** Cells were tested after magnetic sorting of splenocytes for CD4$^+$cells by negative selection. (A) Live cells were gated using PI staining. The resulting cells were primary CD4$^+$. (B) The CD4$^+$ cells were examined for expression of markers distinguishing naïve and memory T cells. A majority were naïve.

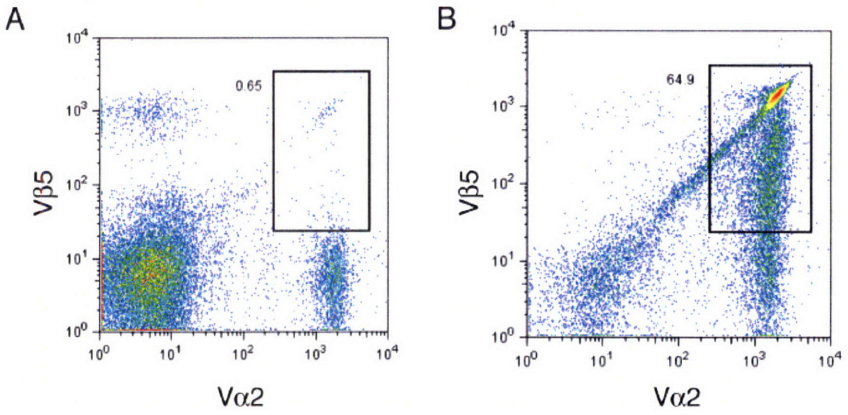

Figure A 2 **T cell receptor (TCR) expression on different mouse strains.** $CD4^+$ cells were sorted using negative magnetic selection as previously described. Expression of the Vα2 and Vβ5 TCR chains was then examined on C57BL/6 (A) and OTII (B) mice. Due to the significant expression of Vα2 on C57BL/6 cells, it is best to gate on both TCR when analyzing co-cultures that contain both cells (if one wants to examine only cells that can respond to OVA peptide).

FACS for T Activation Determination:

Background:

CD69 and CD25 (IL2-α chain) are upregulated upon stimulation of T cells.

Notes/Calculations:

Antibodies

Ab	isotype	amount	2x stock
CD4-biotin	rat IgG2b, K	10 μg/mL	1:25
CD25-PE	rat IgG2b, K	2 μg/mL	1:50
CD69-FITC	hamster IgG1, L3	10 μg/mL	1:25
(CD4-CyC	rat IgG2a, K	2 μg/mL	1:50
CD69-FITC	hamster IgG1, L3	10 μg/mL	1:50

Prep Abs. at 2x concentration, then mix with cells 1:1 (50 μL each).

FACS for T blast phenotype:

Background:

CD8 T cells proliferate more quickly than CD4 and may take over blast cultures even if initially present at low frequencies, so we tested phenotype of our proliferating blasts. We also looked at viability over time, to determine the best time to use the cells in experiments.

Notes/Calculations:

Antibodies

Ab	isotype	amount	2x stock
TCR-FITC	Ar Ham IgG2, L1	5 μg/mL	1:50
CD4-PE	Rat IgG2B, K	1 μg/mL	1:100
CD8-APC	Rat IgG2A, K	1 μg/mL	1:100

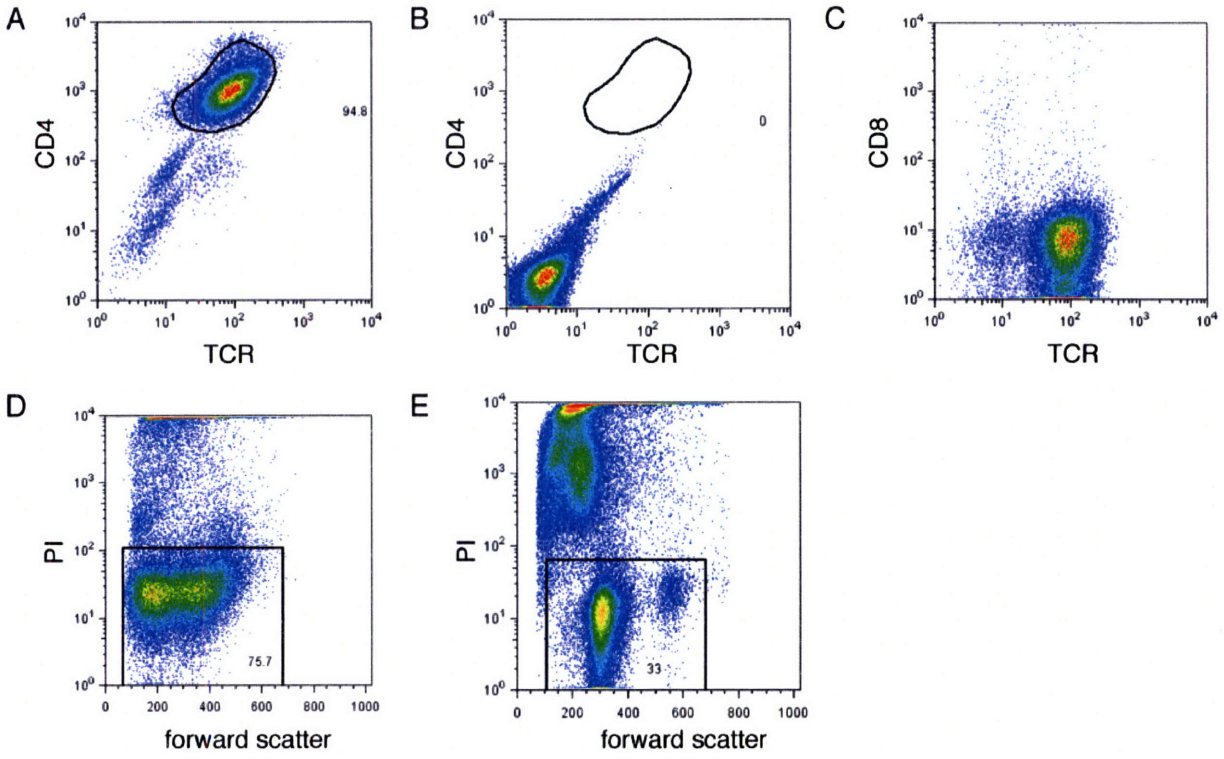

Figure A 3 **T cell blast phenotype.** (A-D) Day 4 T blasts were assessed by flow cytometry. (A and C) T cells were tested with antibodies to T cell receptor (TCR), and CD4 or CD 8 markers. (B) T cells were tested with relevant isoptype control antibodies matched to CD4 and TCR. (D-E) Day 4 (D) and day 7 (E) T cell blast viability was assessed by PI staining.

H.2 Enzyme-linke immunosorbent assay (ELISA)

H.2.1 ELISA protocol

Materials:

Reagent Diluent, Blocking Buffer, Wash Buffer, Stop Solution – see Appendix B.2.4.
Substrate Solution: 1:1 mixture of A and B from R&D (H_2O_2 and tetramethylbenzidine)

Notes:

Be sure to test the OD of a sample-free but treated control: expected value = 0.03-0.06.

Procedure:

1. Use 100 µL per well of capture Ab in PBS: incubate sealed plate O/N at RT.
2. Aspirate and wash wells 3x with wash buffer; blot against paper towel.
3. Block plates (200-300 µL blocking buffer) for at least 1 hour at RT.
4. Repeat 3x wash step.
5. Add samples: typical maximum = 4 ng/mL (e.g., 1 µL in 10 mL): perform doubling dilutions in eppendorfs using 1 mL for max. concentration, then transferring 0.5 mL to 0.5 mL reagent diluent: add 100 µL per well.
6. Tap gently to mix, seal plate then incubate samples 2 h at RT.
7. Repeat 3x wash step.
8. Add 100 µL per well of detection Ab (in RD): (1-)2h at RT.
9. Repeat 3x wash step.
10. Add 100 µL SAv-HRP per well (usually 1:200 dilution): 20 min at RT.
11. Repeat 3x wash step.
12. Add 100 µL substrate soln. per well: incubate 20-30 min. at RT, out of light.
13. Add 50 µL stop solution per well: gently tap to mix, observer w/in 30 min.
14. Perform readings at 450 nm and 540 or 570 nm for wavelength correction.
15. (Analysis: subtract value at 540 from value at 450 and use standard curve.)

Alternate Protocols:

BD

1a. Capture Ab at 1-4 µg/mL in binding solution (pH6 or 9 phosphates) O/N at 4 °C.
2a. Blocking buffer has 1% BSA (in PBS) only.
3a. Samples incubated for 2-4 h at RT or O/N at 4 °C.
4a. Detection Ab at 0.5-2 µg/mL: 1h at RT.
5a. SAv-HRP diluted in blocking buffer/tween.

Miller Lab

1a. Capture Ab O/N at 4 °C in PBS.
2a. Blocking step may be done O/N at 4 °C.
3a. Standards from 20 ng/mL down.
4a. Samples may be incubated O/N at 4 °C with shaking.

H.2.2 Specific Chemokine Information

From R&D: reconstitute capture with sterile PBS (e.g., 0.5 mg/mL); reconstitute detection with 20 mM Trizma base, 150 mM NaCl, 0.1% BSA, pH 7.3.

SLC:

- capture at 2 ug/mL, and detection at 50 ng/mL
- suggested two-fold dilution series beginning at 2 ng/mL
- usually 2 ng/mL in non-linear regime, cut this data point during analysis.

ELC: like SLC, except use detection at 100 ng/mL.

From BD: comes as a liquid: both capture and detect at 0.5 mg/mL.

IL-2: 500 → 4 pg/mL dilution series (despite usual BD is 2000 → 15).
Detection Ab diluted from 500 → 1 μg/mL: 20 μL per 10 mL.

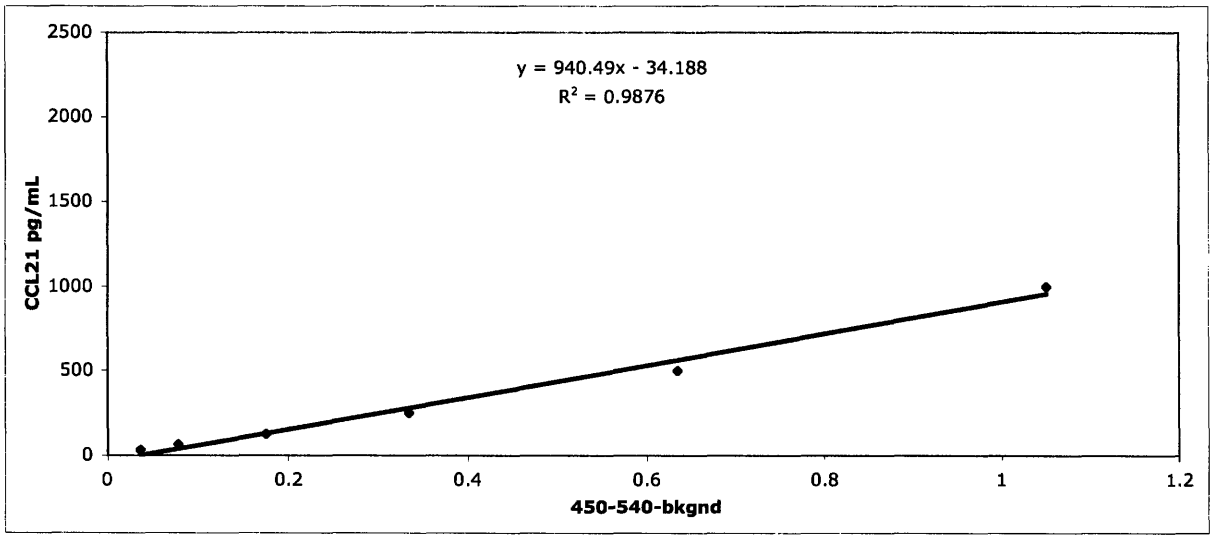

Figure A 4 **Typical calibration curve for CCL21 ELISA data.** Highest (2000 pg/mL) and lowest (15.625 pg/mL) data points were removed due to being outside the linear region, and outside the detection limit, respectively.

s

H.3 High-pressure liquid chromatography (HPLC)

H.3.1 HPLC protocol

Sample Prep

- Previously used 10 mg sample in 0.5 mL for peptide
- S-75 column instructions say:
  - protein <= 10 mg
  - filter sample or centrifuge at 10,000 g for 10 min
  - 0.5-0.75 mL/min good starting point.
  - 25 μL sample volume good starting point.

Superdex-75 Column Info

- Maximum back-pressure is 1.8 MPa.
- Approx. 24 mL bed volume.
- Optimum separation range 3 K-70 K for globular proteins.
- Equilibration after long-term storage
  - 50 mL water at 0.5 mL/min
  - 50 mL eluant at 0.5 mL/min
- Equilibration for storage
  - 50 mL water
  - 50 mL 20% ethanol

Procedure

5. Turn on computer, all components (4 power switches).
6. Load D7000-HSM program.
7. For system status hit *i* button and hit initialize to ready system.
8. Open a sample table, then data acquisition to get immediate read.
9. Must start manually: hit pump on to start, slowly work up flowrate.
10. See sheet for troubleshooting rise in backpressure if necessary.
11. Hit autozero to re-zero absorbance (top box) when necessary – get steady.
12. Before using autosampler, hit "WASH" key to clean flow path.
13. Run samples.

To flush

1. Turn pump off.
2. Open rightmost valve.
3. Turn pump on, hit purge.
4. Hit purge again to stop.

For flush, just goes source -> pump -> out. (Normally source -> pump -> mixer -> autosampler -> quad filter -> column -> detector -> waste.)

Writing a method

Note: Beware of pitfalls/redundancies where you need to set a parameter twice or it won't work correctly. Below I will describe the buttons going left-to-right (upper row first).

- Configuration
  - make sure correct components are selected
  - to recognize multiple solvents, switch to gradient mode "low"
- Information
  - fill out solvent info, method description, etc
- Pump
  - **set pressure limit!**
  - set flowrate, solvents desired, etc
- Autosampler
  - defaults should mostly be fine
  - may experiment with *cut* or *loop* and injection volume
- Detector
  - defaults should mostly be fine
  - **set the correct end time here**
- Various reports stuff
  - defaults should mostly be fine
  - **set intensity range and time axes**

Writing a sample table

- Needs to refer to the same method on both tabs (upper left to toggle between tabs)
- Injection volume needs to agree with method on both pages
- Rest is straightforward (mostly use defaults)

H.3.2 HPLC calibration data

Ran standard kit from Bio-Rad at 0.2 mL/min on an S75 column in pure PBS.

MW (g/mol)	Time (min)
158000	46.2
44000	55.4
17000	67.6
1350	96.6

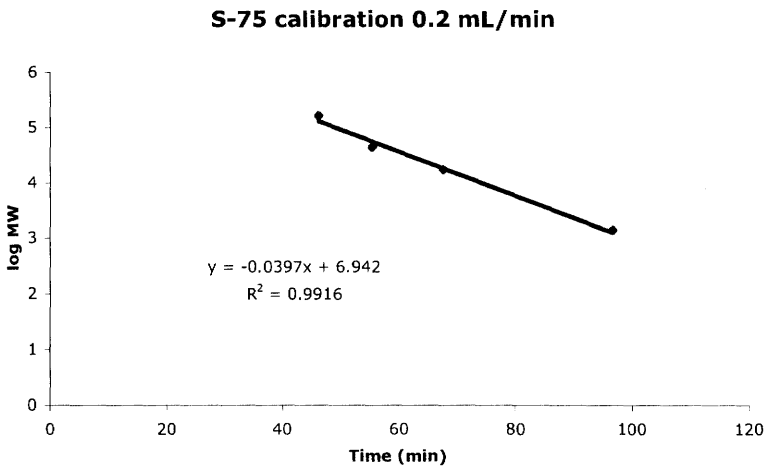

Figure A 5 **Sample calibration for HPLC.**